Master of Science Thesis

An Assessment of Acoustically Transparent Wind Tunnel Walls

for improving aero-acoustic measurements

Maarten Debrouwere

December 6, 2013

Faculty of Aerospace Engineering

Delft University of Technology

An Assessment of Acoustically Transparent Wind Tunnel Walls

for improving aero-acoustic measurements

Master of Science Thesis

For obtaining the degree of Master of Science in Aerospace Engineering
at Delft University of Technology

Maarten Debrouwere

December 6, 2013

Faculty of Aerospace Engineering · Delft University of Technology

Delft University of Technology

DELFT UNIVERSITY OF TECHNOLOGY
DEPARTMENT OF AERODYNAMICS

The undersigned hereby certify that they have read and recommend to the Faculty of Aerospace Engineering for acceptance the thesis entitled **"An Assessment of Acoustically Transparent Wind Tunnel Walls"** by **Maarten Debrouwere** in fulfillment of the requirements for the degree of **Master of Science**.

Dated: December 6, 2013

Supervisors:

Prof. dr. F. Scarano

Ir. S. Pröbsting

Prof. dr. D.G. Simons

Ir. M. Tuinstra

Summary

One of the main limitations of microphone measurements in an open-jet wind tunnel is spectral broadening. The phenomenon of spectral broadening is observed when a single frequency sound wave passes through a free shear layer. Inside the turbulent shear layer the wave interacts with the turbulence, which leads to broadening of the tone in the frequency domain. The spectrum of a single frequency tone measured with a microphone will not only include the peak but also two shoulders containing the broadened frequencies, one on each side of the peak. Spectral broadening does not only affect single microphone measurements but also has a detrimental effect on acoustic array measurements. The distortion caused by the shear layer will reduce the coherence between the microphones in the array. This limits the size and thus resolution of the array. This spectral broadening is particularly problematic when examining objects which produce a tonal noise, e.g. open rotors, sharp edges.

Several institutes have installed an acoustically transparent wall (ATW) in the test section of a wind tunnel to overcome this limitation. Such a wall replaces the free shear layer with a turbulent boundary layer reducing the size and intensity of the turbulent structures and therefore the amount of spectral broadening. The main goal of this research project is to improve aero-acoustic wind tunnel measurements by evaluating the acoustic and aerodynamic properties of an acoustically transparent test section compared to a traditional open jet configuration. Initially the acoustic and aerodynamic properties of various porous materials were investigated separately after which a series of aero-acoustic wind tunnel experiments was performed to characterize the full system. The use of perforated metal plates as ATW was investigated as an alternative to conventional tensioned fiber weave walls, since these are difficult to produce and tedious to work with.

From sound transmission measurements performed in an anechoic chamber, it could be concluded that all porous materials showed good transmission characteristics up to 7 kHz. Both the fiber weave materials and perforated plates showed little difference from the clean configuration (no material). At higher frequencies the perforated plates suffered from reflecting sound waves because of a lower open area ratio compared to the fiber weaves.

To model spectral broadening, the interaction between a sound wave and the turbulent structures is examined. A clear relation is found between the amount of spectral broadening and the thickness of a turbulent region and the velocity fluctuations in the direction of the propagating sound wave. Therefore a series of PIV measurements was conducted to determine the thickness and velocity fluctuations normal to the free stream of the boundary layer over different porous materials and a free shear layer. A prediction of the amplitude of the time delay variations on a sound wave caused by the turbulence was made based on the measured aerodynamic quantities. These time delay variations are responsible for the spectral broadening observed during wind tunnel measurements. It was found that based on the measured aerodynamic quantities a reduction in amplitude of time delay variations of at least 90 % was found over all porous materials compared to a free shear layer. The tensioned fiber weave material even showed a reduction of almost 95 %.

Finally, a speaker source was observed with both a single microphone and microphone array system, either through a free shear layer or through an acoustically transparent wall. The single microphone measurements through the free shear layer showed the spectral broadening with the associated shoulders in the frequency spectrum. When an ATW was used, nearly all energy remained in the peak, indicating the absence of spectral broadening. However the presence of an ATW elevated the background noise when the wind tunnel was operational.

Analysing the source maps calculated from data acquired with a microphone array, it was found that the interaction between the turbulent structures in a free shear layer and an acoustic wave not only lead to spectral broadening, but also lead to spatial broadening for microphone array measurements. Two spurious sources were found at the broadened frequencies. Through the free shear layer the amplitude of these spurious sources led to corrupted results, drastically increasing the - 3 dB beamwidth and reducing the dynamic range of the measurement. For instance, with a free stream velocity of 30 m/s and a tonal source of 16 kHz, the intensity of the spurious sources was 5 dB above the actual source, while through the acoustically transparent walls these spurious sources were not found or had an amplitude 30 dB below the actual source. This means that almost no spatial broadening is observed through an ATW with a microphone array. Therefore, both the tensioned glass fiber wall and the perforated metal plate greatly improve aero-acoustic wind tunnel measurements if a single frequency source is observed. It must be noted that a perforated metal plate is a viable alternative to tensioned fiber weave materials. Except for the increased background noise, little difference was found between the two porous materials. Furthermore a perforated plate offers many benefits with respect to the construction of the test section.

Acknowledgements

This master thesis concludes my education as aerospace engineer, I would like to express my gratitude towards all people who have assisted and supported me during this research project and my eduction in general. First of all I would like to thank Prof. dr. Fulvio Scarano and Ir. Stefan Pröbsting for their guidance and advice. I am also very grateful to Prof. dr. Dick Simons for introducing me to the field of acoustics and microphone array systems in particular. Next I would like to thank Prof. dr. ir. Georg Eitelberg and Ir. Marthijn Tuinstra for their helpful and contributing comments during progress meetings and their cooperation in lending me two NLR speaker sources. From the physics department I thank Dr. ir. Eric Verschuur and Henry den Bok for their cooperation and assistance during my measurements in the anechoic chamber of TNW. I'm also thankful for the help I received from the technical staff at the aerodynamics group while building and setting up my experiments. I'm also grateful for the assistance I received from Bert van Midden and Kirk Scheper with the acoustic array. Last but not least I would like to thank my friends, family and in particular my parents who have always supported me during my educational period and this research project.

Maarten Debrouwere

Table of Contents

List of Figures

List of Tables

Nomenclature

Abbreviations

ADC	analogue to digital converter
ATW	acoustically transparent wall
B&K	Bruel & Kjaer
DAQ	data acquisition system
FFT	fast Fourier transform
FOV	field of view
JAXA	Japanese aerospace exploration agency
KAT	kleine anechoische tunnel, at NLR
NLR	nationaal lucht- en ruimtevaartlaboratorium
PIV	particle image velocimetry
PSD	power spectral density
SPL	sound pressure level [dB]
TKE	turbulent kinetic energy

Greek Symbols

α	initial acoustic path angle
$\delta*$	displacement thickness [m]
ΔR	extra path length [m]
Δs	particle displacement [m]
Δt	time delay [s]
δ	thickness of turbulent layer [m]
λ	final acoustic path angle
λ_l	wavelength of laser light [m]
ϕ	angle along vortex where acoustic ray enters
ρ	air density $[kg/m^3]$
σ	spreading rate shear layer
Θ	propagation angle
θ	momentum thickness [m]

Θ'	emission angle
Θ_0	refraction angle
Θ_m	angle between wind tunnel axis and the source-microphone vector
ξ	source position

Latin Symbols

$\bar{g}$	steering vector
d_p	particle diameter [m]
d_τ	particle image diameter [m]
E_{ratio}	ratio of peak energy over total energy [-]
f	frequency [Hz]
R_m	straight source to microphone distance [m]
R_t	orthogonal source to shear layer distance [m]
u	streamwise velocity component [m/s]
v	normal velocity component [m/s]
X_m	microphone position
y^+	non-dimensional wall distance [-]
a	amplitude calculated by beamforming algorithm
c	speed of sound [m/s]
D	microphone array diameter [m]
f#	f-stop of lens [-]
M	Mach number [-]
M	magnification factor [-]
P	power calculated by beamforming algorithm
p	recorded microphone pressure [Pa]
r	distance [m]
T	acoustic power transmission coefficient
Z	distance between array and source [m]

Superscripts

$'$	fluctuating component
$\bar{}$	mean component

Subscripts

∞	free stream velocity value
bl	boundary layer
m	microphone index
max	maximum value
sl	free shear layer
ref	reference value
rms	root mean square value

Chapter 1

Introduction

Stricter noise regulations around airports (Jabben et al., 2010, Brueckner and Girvin, 2006) and more social awareness of noise pollution have made the topic of aero-acoustics a major research field over the years. Since high by-pass ratio turbofan engines are producing less and less noise with every generation, airframe noise (Yamamoto et al., 1995) tends to become the dominant factor during the landing phase. Therefore good knowledge on which part of the airframe produces the most noise is required. With the help of more powerful computers and data acquisition systems, phased microphone arrays have become the tool of choice for noise source identification (Michel, 2006). These measurements combined with beamforming algorithms allowed researchers to locate sound sources on aircraft fly-overs (Sijtsma, 2010), windmills (Ramachandran et al., 2012), model landing gears in a wind tunnel (Ravetta et al., 2004), etc.

When using an open jet facility for acoustic testing the microphones are usually placed outside the airflow. This eliminates interaction between the (turbulent) flow and the microphone membranes. The problem in open jet wind tunnels is that there is a free shear layer between the source and the microphones. This leads to a distortion of the sound waves called spectral broadening, additionally to the refraction of the wave across the interface (Sulaiman, 2011). This makes characterization of tonal noise sources less accurate and the experiment in general becomes more difficult.

The main objective of this research project is to improve aero-acoustic wind tunnel measurements by investigating the acoustic and aerodynamic properties of an acoustically transparent test section compared to a traditional open jet configuration. The emphasis of this research will be on reducing spectral broadening caused by the turbulence in a free shear layer. At first the aerodynamics and acoustics were evaluated separately. Different materials were tested for acoustic transmission and distortion in an anechoic room. Next to that a boundary layer survey was performed for each material to determine the relevant flow properties. Finally all elements are combined to characterize the complete system.

Chapter 2

Aeroacoustic measurements through shear layers

2.1 Aero-acoustic measurements

In this section the general measurement techniques used for aero-acoustic testing are outlined. The focus of this section lies on sounds source localisation by means of a phased microphone array. In addition to the microphone array system described, single microphone measurements are often performed simultaneously in order to get a quick analysis of the sound pressure level (SPL) and the spectral distribution related to the source.

2.1.1 Single microphone measurements

The most basic way of analysing the sound produced by a source, is done by recording the response of a single microphone. A microphone transforms the sound/pressure wave into an electrical signal which can be recorded for further analysis. If a calibrated microphone is used, the recorded sound pressure level (SPL) can be determined with equation 2.1. Where p_{rms} is the root mean square value of the recorded pressure signal. The reference pressure p_{ref} is usually set at 20 μPa (rms), which corresponds to the threshold for human hearing. Another way of analysing the recorded signal is by performing a Fourier transform. This mathematical operation transforms the signal from the time domain to the frequency domain. This allows researchers to see which frequencies contain the most energy. The frequency spectrum of the recorded time series of the pressure p(t) is given by equation 2.2. An example of a resulting frequency spectrum for various airfoil sections is shown in figure 2.1.

$$SPL = 10log_{10}\left(\frac{p_{rms}^2}{p_{ref}^2}\right)[dB] \tag{2.1}$$

$$p(f) = \int_{-\infty}^{+\infty} p(t)e^{-2\pi ift}dt \tag{2.2}$$

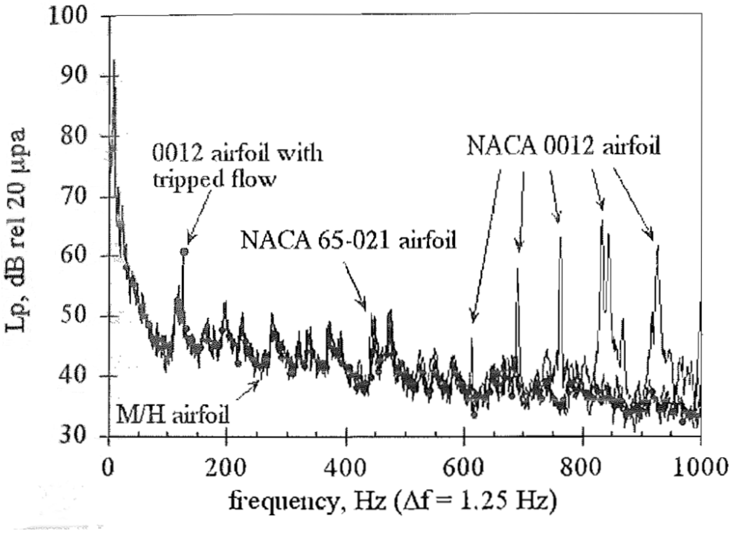

Figure 2.1: Example frequency spectrum from single microphone measurement with $U_\infty = 23$ m/s, (Allen et al., 2002)

In a wind tunnel environment microphones are used to determine the sound levels radiated by a vehicle of vehicle component. This can be a complete aircraft fly-over simulation, a model lading gear or a propulsion device like a jet and open rotors. Equally important as the absolute level is the difference in sound level between different configurations or operating conditions. The shift in frequency peaks is also relevant when analysing different configurations with a microphone system.

The main problem when performing a single microphone measurement is the presence of background noise. The background noise can originate from the drive fan, struts and mounting points, ducts or turbulent layers. These will spoil the measurement and with a single microphone it is very hard to determine which part of measurement is due to the model and which part is due to background noise. Furthermore reflections inside the test section or wind tunnel room might amplify certain frequencies leading to false sound level estimations. In addition to that it is impossible with a single microphone to determine which part of the model is generating the sound. To address all these limitations of single microphone measurements, researchers started using phased microphone arrays which allow for sound source localisation on a specific part of the test set-up. This technique will be detailed in the next sections.

2.1.2 Phased microphone array measurement technique

Phased microphone arrays have become the tool of choice for (aerodynamic) noise source identification (Michel, 2006). This measurement instrument usually has three main components: the microphone array, the data acquisition system and the post processing software (Allen et al., 2002). Such a system is capable of identifying sound sources and even estimating the sound pressure level when properly calibrated and assuming the sources are uncorrelated (Oerlemans and Sijtsma, 2002).

The physical array consists of multiple microphones in a specified configuration. The lay-out of the microphone positions has a great influence on the resolution and performance of the whole system. The aim is to have a different microphone to source distance, for all possible sources observed. The array can be randomly configured and then optimized (Sijtsma, 2010) or logarithmic and spiral shapes have proven to be working well (Allen et al., 2002). An example phased microphone array with 32 microphones in a spiral configuration which was developed at the TU Delft, is shown in figure 2.2. The three main components mentioned earlier are clearly distinguishable in the photo: the physical microphone array, the data acquisition box and the post-processing.

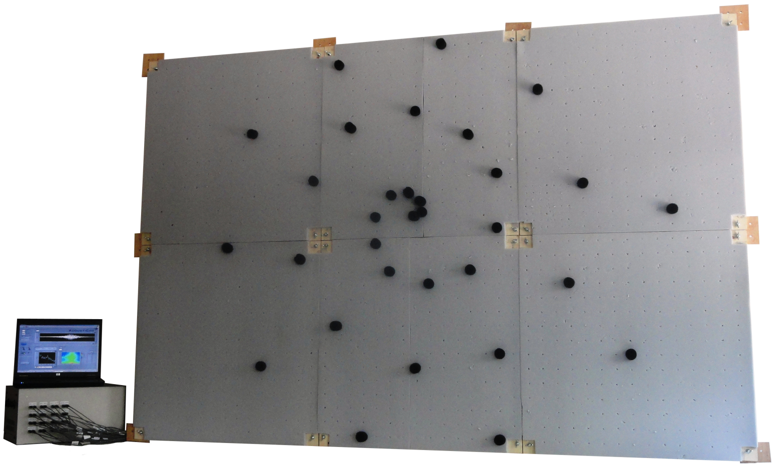

Figure 2.2: Example phased microphone array with 32 microphones

The working principle of an acoustic array is as follows. If a sound source is observed with an acoustic array, the emitted sound waves propagate through the air and excites the microphone membranes. The microphone transforms the sound pressure wave into an electrical signal, which is processed by so-called front-end electronics. For instance the electrical signal could be sent through a high- and low-pass filter to eliminate very high and low frequencies and an amplifier to cover the full dynamic range of the analogue to digital converters (ADC). At that stage the analogue signal is converted to a discrete digital signal and gets sampled by the data acquisition system. From there it is sent to a computer where the audio files are stored. It is of paramount importance that all the microphone channels are sampled at the same time because during the final step, the post processing, the time delay between the different channels is used for sound source localisation. This post processing uses a beamforming algorithm, many different variations exist but they all follow the same principle. For reference the conventional frequency domain beamformer described by Sijtsma (2010) will be detailed here.

The method is based on modelling the microphones amplitude and phase response to a unit strength source at a position of interest, called the "steering vector" $\bar{g}$. This steering vector contains the modelled response of each microphone per frequency for a selected point in the scan plane. Figure 2.3 shows a sketch of the situation. Where X_m represents the microphone position vector of microphone m, ξ the position vector of the source in the scan plane. r_m is the distance between that source in the scan plane and microphone m. In mathematical terms the elements of the (simplified) steering vector for an array with M microphones are given by equation 2.3. In this equation Δt_m is the travel time of the signal between the source and microphone m, which is equal to r_m/c assuming the speed of sound remains constant. f represents the frequency of interest.

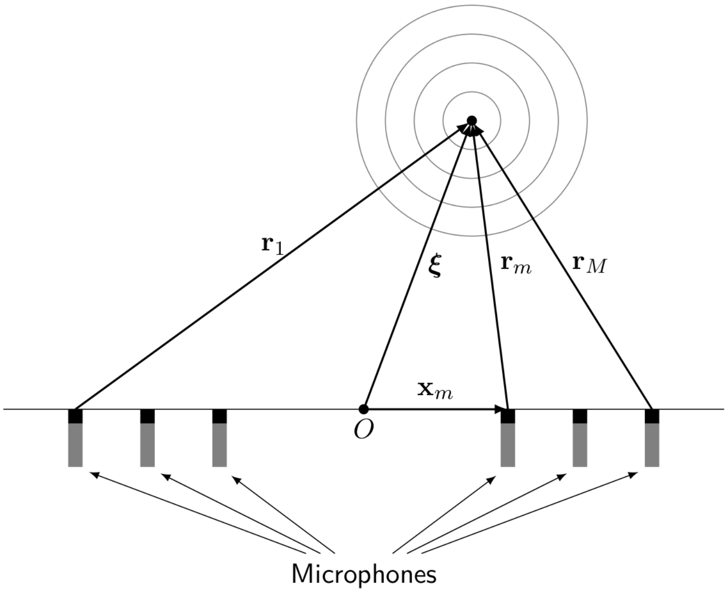

Figure 2.3: 2D sketch of source and microphone array, (Midden, 2013)

$$g_m = \frac{-e^{-2\pi i f \Delta t_m(X_m,\xi)}}{4\pi \|X_m - \xi\|} \qquad for \qquad m = 1, 2, .., M \tag{2.3}$$

This simulated signal is then compared to the actual recorded signal in the frequency domain $\bar{p}$ by solving the minimization problem $\|\bar{g} * a - \bar{p}\|$. The solution for the relative amplitude a

is then given by:

$$|a| = \frac{\bar{g} \cdot \bar{p}}{\|\bar{g}\|^2} \tag{2.4}$$

The actual source power at the location of interest is then given by $P = \frac{1}{2}|a|^2$. Repeating this process for many different locations in a physical space (usually a plane) results in a source map of that region. An example source map is given in figure 2.4, with this technique sound sources can be identified.

The spatial resolution element (the smallest distinguishable element) of this technique is defined as the width of the main lobe in the source map, 3 dB below the peak value (Sijtsma, 2004). A rule of thumb is used to estimate the size of the resolution element for an acoustic camera given by equation 2.5, where Z is the distance between the array and the source, D the diameter of the array and f the frequency of interest. The actual size of the resolution element obtained during a measurement also depends on the signal to noise ratio and coherence of the microphones and is greatly influenced by the type of beamformer used. It is therefore difficult to exactly determine the resolution element for a specific measurement.

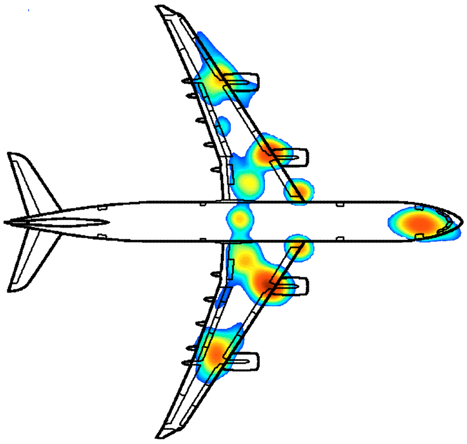

Figure 2.4: Source map of Airbus A340 during approach, (Sijtsma, 2004)

$$resolution\ element\ [m] = \frac{425 \cdot Z}{D \cdot f} \tag{2.5}$$

2.1.3 Applications

The technique described above can be applied in many fields. This literature review focuses on the application of acoustic arrays for observing aero-acoustic sound. The two major fields of application are aircraft fly-overs (Stoker et al., 2003) (Sijtsma and van der Waal, 2004) and wind tunnel measurements (Sijtsma and van der Waal, 2004), those will be discussed next. Other, less relevant, aero-acoustic applications are full scale turbo-fan engine (Siller et al., 2008) and windmill (Oerlemans and Méndez López, 2005) measurements, those will not be treated.

For aircraft fly-over measurements (Sijtsma and van der Waal, 2004) a fairly large array (up to 13 by 13 m) is placed in line with the runway at an airport. The large array is required to obtain the desired resolution on the aircraft. When an aircraft lands or takes-off a measurement can be performed. For post processing the aircraft fly-over measurement there are two possibilities. A moving source beamformer can be used to compensate for the movement of the aircraft or only a very short timespan (0.2 to 0.5 s) is used so that the movement of the aircraft can be ignored during that interval (Midden, 2013). A typical test set-up is shown in figure 2.5 and a representative result was already given in figure 2.4.

Figure 2.5: Acoustic array measurement at Schiphol airport, (Sijtsma and van der Waal, 2004)

The second major field of application for phased microphone arrays in the field of aero-acoustics is wind tunnel measurements (Sijtsma, 2010). Here a distinction can be made between facilities with an open jet test section and a closed test section. For a closed test section the microphones are usually embedded in the wall of the wind tunnel to form the array. For open jet measurements the microphone array has its own structure and is placed outside the airflow. The chamber in which the open jet exits is often made anechoic to greatly reduce the background noise. Since these measurements do not require equipment installed on the test model, they are sometimes performed simultaneously with aerodynamic measurements to save time and in an industrial context costs. A closed section test set-up is depicted by figure 2.6(a) and an open jet facility can be seen in figure 2.6(b). In both figures the microphones are located in the red area.

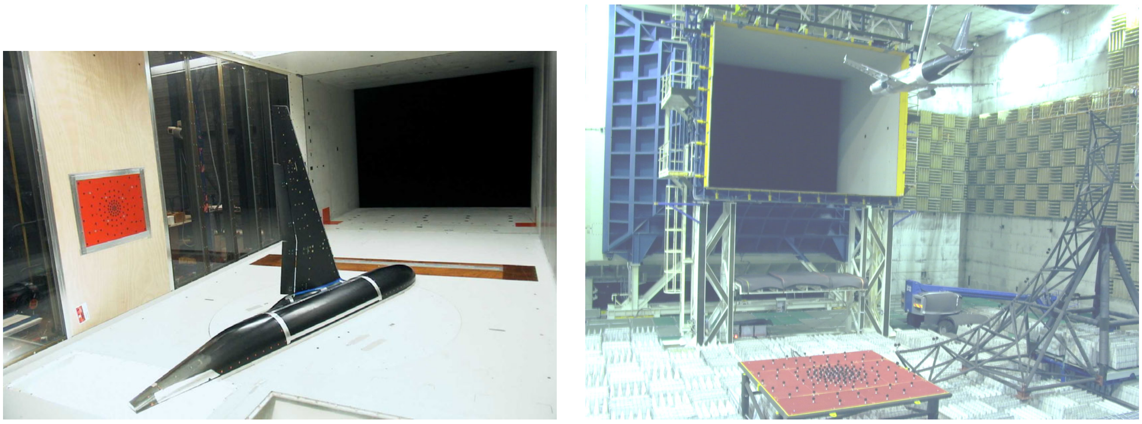

(a) Closed test section DNW-LST (b) Open jet configuration in DNW-LLF

Figure 2.6: Closed and open test section acoustic measurements, (Sijtsma, 2010)

2.1.4 Limitations

The main limitation during aircraft fly-over measurements is the uncertainty of the environment (Midden, 2013). In order to get accurate results from the beamforming algorithm the path the sound wave follows from its origin to the microphone needs to been known as good as possible. For fly-over measurements that usually poses several problems. The atmospheric conditions like temperature, pressure and local wind vector along the sound waves paths are unknown. More importantly the exact position of the aircraft is usually unknown as well. All these factors have a negative effect on the resolution obtained by the beamforming algorithm. A second drawback of fly-over measurements is that a moving source is observed. Although correction models exist for moving sources, since the exact speed of the aircraft is not known, beamforming on moving sources remains difficult even with these correction models. Furthermore such a moving source beamforming algorithm is computationally very expensive compared to a stationary measurement (Midden, 2013).

Wind tunnel tests have the advantage of a more controlled environment but introduce several new problems for acoustic measurements. In a closed test section the microphones record a high self noise due to the turbulent boundary layer interacting with the microphone membrane (Jaeger et al., 2000). In addition to that the sound produced by the model is reflected by the wind tunnel walls, this reduces the signal to noise ratio (SNR) of the obtained data (Ehrenfried et al., 2007). When using an open jet facility the microphone array can be placed outside the airflow eliminating the interaction between a turbulent boundary layer and the microphones. The problem in open jet wind tunnels is that there is a free shear layer between the source and the microphones which leads to spectral broadening of the signal (Sulaiman, 2011). In addition to that the sound waves are refracted over a shear layer. These distrotions will be discussed in section 2.3. These two effects make the beamforming algorithm less accurate and the measurement in general becomes more difficult.

2.2 Aerodynamic properties of free and wall bounded shear layers

To begin this section on the aerodynamic properties of a turbulent shear layer and a turbulent boundary layer, some basic definitions are made. First of all, the thickness of a boundary layer is defined here as the distance between the surface and the point were $u/u_\infty = 0.95$. In case of a shear layer the thickness is found between the points $u/u_\infty = 0.95$ and $u/u_\infty = 0.05$. Two other useful quantities in the analysis of viscous flows are the displacement thickness δ^* and the momentum thickness θ. Assuming a constant density the following relations are found:

$$\delta^* = \int_{-\infty}^{-\infty} \left(1 - \frac{u}{u_\infty}\right) dy; \qquad \theta = \int_{-\infty}^{-\infty} \frac{u}{u_\infty} \left(1 - \frac{u}{u_\infty}\right) dy \tag{2.6}$$

A common manipulation made to quantities in the analysis of turbulent flows is Reynolds decomposition. It is a mathematical technique were a certain quantity is replaced by its mean and a fluctuating part. For example the streamwise velocity component $u = \overline{u} + u'$. Where $\overline{u}$ is the average streamwise velocity and u' are the fluctuations. These fluctuating components can represent the amount of turbulence in a flow by expressing the turbulent kinetic energy (TKE) defined as:

$$k = \frac{1}{2}(\overline{(u')^2} + \overline{(v')^2} + \overline{(w')^2}) \tag{2.7}$$

2.2.1 The turbulent free shear layer

At the interface between two uniform parallel streams of fluid with a different mean velocity, a free shear layer or mixing layer will develop. Momentum from the stream with the highest velocity will be transported towards the stream with the lower mean velocity. This means that from the interface on one stream will see a decrease in local flow velocity while the other stream undergoes the opposite. The geometry of a free shear layer and the resulting mean streamwise velocity profile are depicted in figure 2.7. In the case of an open jet wind tunnel, the flow with the lower velocity is the ambient air in the room which is at rest. At the interface large scale turbulent structures will develop. A flow visualisation of two mixing layers where the upper fluid has a velocity of 10 m/s and the lower fluid a velocity of 3.8 m/s clearly shows these large turbulent structures, see figure 2.8.

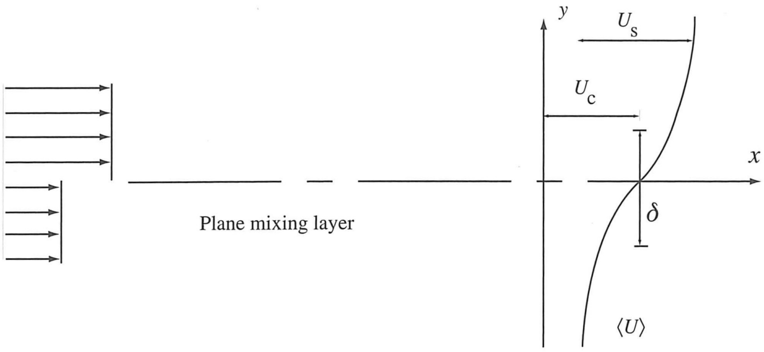

Figure 2.7: Geometry of a plane mixing layer, (Pope, 2000)

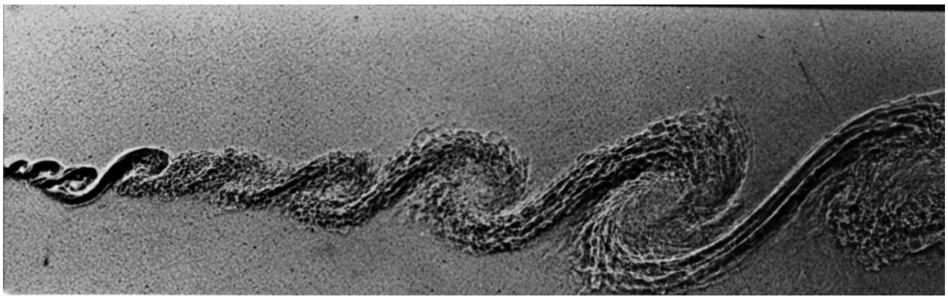

Figure 2.8: Visualization of large scale turbulent structures in a mixing layer, (Van Dyke, 1982)

The geometry of a typical open jet wind tunnel is depicted in figure 2.9. At the jet exit two mixing layers or shear layers start to develop. When the two shear layers join, the jet is fully developed and becomes self similar. Since measurements are carried out in the potential core of the jet, any aeroacoustic sound produced in a open jet wind tunnel will have to cross the shear layer. A solution for the velocity profile in a shear layer is given by Gortler (White, 1991). In this equation x is the axial position behind the origin of the shear layer and y the lateral distance with $y = 0$ at the lip-line. The parameter σ represents the spreading of the shear layer and can change for different facilities or conditions.

$$\frac{\overline{u}}{u_\infty} = \frac{1}{2}\left(1 + erf(\frac{\sigma y}{x})\right) \qquad \sigma \approx 13.5 \tag{2.8}$$

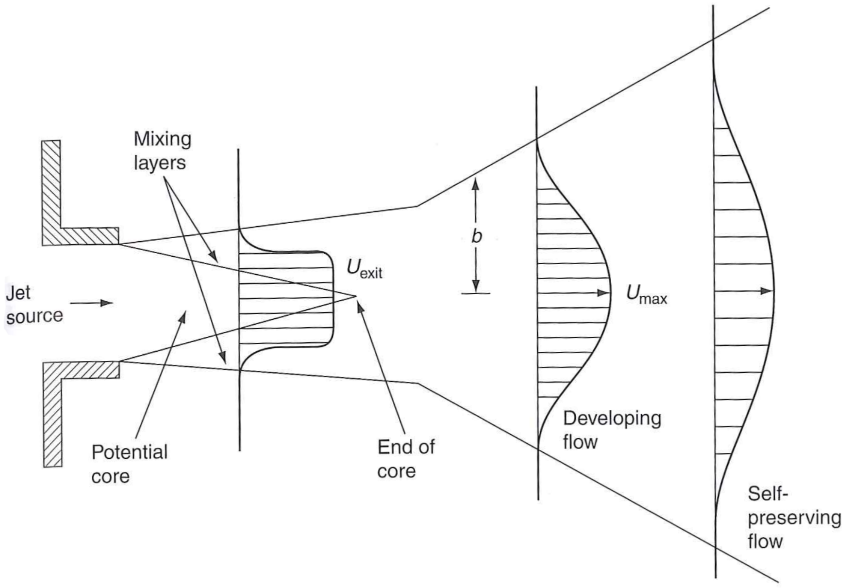

Figure 2.9: Geometry of developing jet, (White, 1991)

For a simple linear velocity profile along the shear layer, the shear layer thickness is equal to six times the momentum thickness. Using equations 2.6 and 2.8, a simple relation for the shear layer thickness is found.

$$\delta_{sl}(x) = 6 \cdot \theta = \frac{6}{4} \int_{-\infty}^{\infty} 1 - erf(\frac{\sigma y}{x}) dy = \frac{6}{\sqrt{2\pi}} \frac{x}{\sigma} \tag{2.9}$$

This theory has been confirmed by a large number of experiments (White, 1991), figure 2.10 for example shows mean axial velocity profile obtained from a hot-wire experiment and the analytic Gortler solution from Krober et al. (2013). In addition to the mean velocity profile, the turbulent intensities for u'_{rms} and v'_{rms} are given by Krober et al. (2013). Figures 2.11(a) and 2.11(b) can be used as a reference for new measurements.

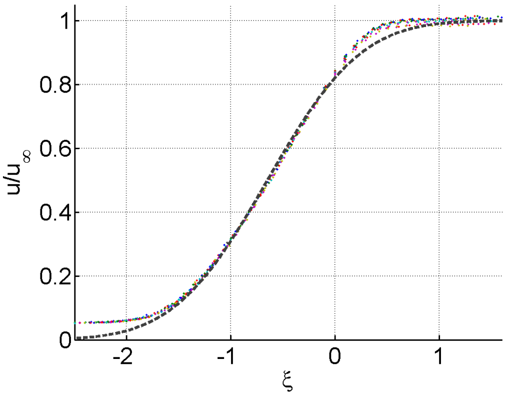

Figure 2.10: Normalized mean axial velocity profiles from hot-wire measurement (coloured points) and analytic Gortler solution (dotted line). Flow velocity of 60 m/s , (Krober et al., 2013)

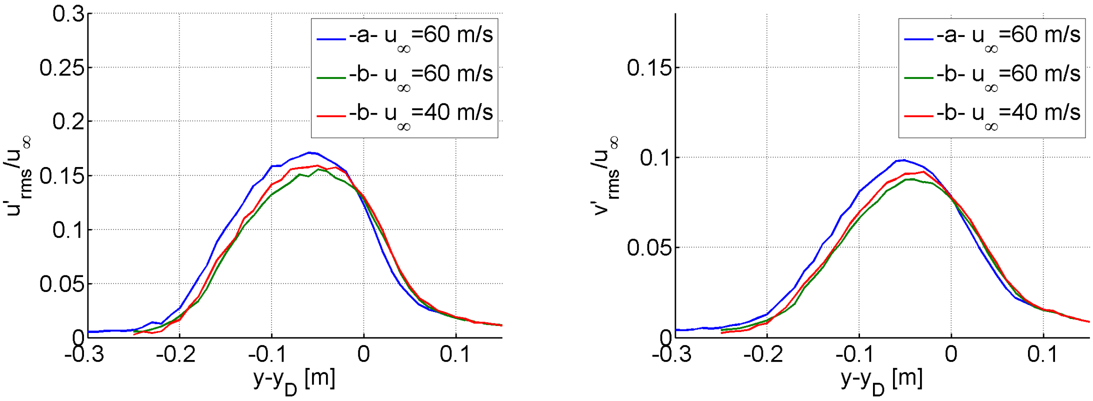

(a) Axial velocity fluctuations (rms)

(b) Lateral velocity fluctuations (rms)

Figure 2.11: Turbulent intensities from hot-wire measurements in shear layer, (Krober et al., 2013)

2.2.2 The turbulent boundary layer

When a fluid flows past a solid surface a boundary layer will develop. The typical shape of the mean velocity distribution and thickness of such a boundary layer can be seen in figure 2.12. Initially the boundary layer will be laminar but after transition has occurred the boundary layer will become turbulent. Prandtl (White, 1991) derived simple approximations for the mean velocity profile, thickness and the momentum thickness of a turbulent boundary layer.

$$\frac{\overline{u}}{u_\infty} \approx \left(\frac{y}{\delta_{bl}}\right)^{1/7}; \qquad \frac{\theta}{\delta_{bl}} \approx \frac{7}{12}; \qquad \frac{\delta_{bl}}{x} \approx \frac{0.16}{Re_x^{1/7}} \tag{2.10}$$

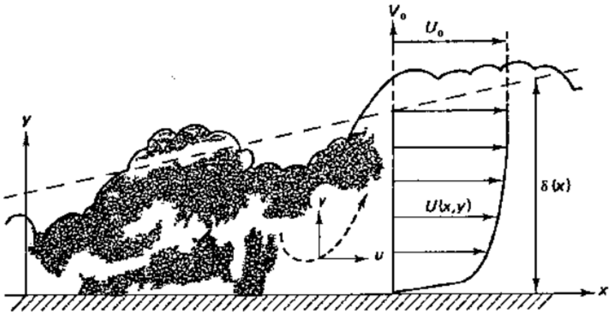

Figure 2.12: Typical shape of the mean velocity profile in a boundary layer, (Tennekes and Lumley, 1990)

For a more detailed analysis of the turbulent boundary layer, the flow is usually divided into three parts (Pope, 2000).

- The inner layer: This region is closest to the wall and governed by the "Law of the Wall" which is valid for $0 < y/\delta < 0.1$ (Pope, 2000). In this region the flow does not depend explicitly on the free stream conditions since it is governed by the viscous shear with the wall.
- The outer layer: In this region the flow does depend on the free stream conditions and is independent from the wall conditions since the flow is now dominated by turbulent shear. The flow in the outer layer is described by the "Defect Law" (Pope, 2000). Which is valid for values of $y^+ > 100$. Where y^+ is the non-dimensional wall distance.
- The overlap region: The final region connects the inner and outer layer. In this region both turbulent and viscous shear are important. It is important that the outer and inner layer are smoothly connected by the "Logarithmic Law" (Pope, 2000).

The mean velocity profile and turbulent quantities of a turbulent boundary layer have been investigated previously. As reference the results of a flat plate measurements done by Klebanoff (1955) are given in figure 2.13. The graph contains the mean velocity profile as well as the profiles for the fluctuating velocity components

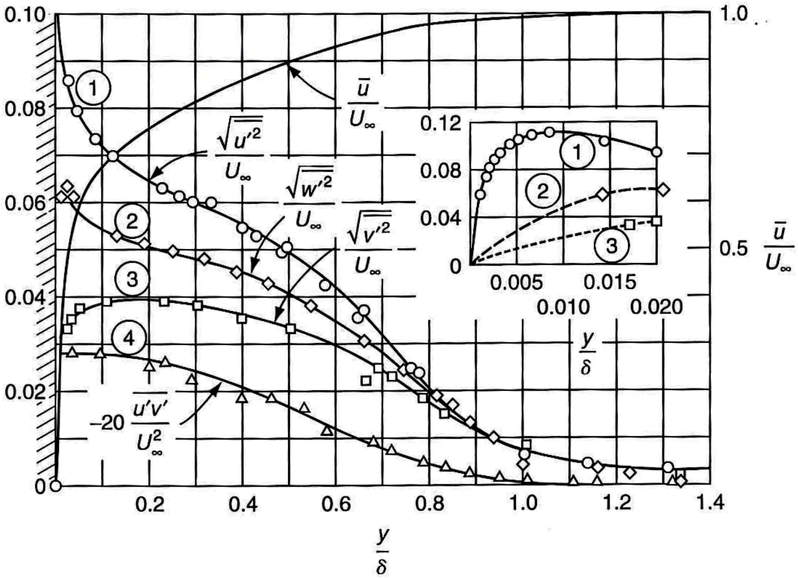

Figure 2.13: Flat plate measurements by Klebanoff (1955), (White, 1991)

2.3 Sound propagation trough a turbulent shear layer

2.3.1 Shear layer refraction

When a sound wave passes through a shear layer it changes its direction of propagation due to the different properties inside and outside the jet. The following section summarizes the description of this phenomena and a correction method which was given by Allen et al. (2002). In this analysis the shear layer is modelled as an infinity thin cylindrical vortex sheet which is located at the nozzle lip line. The geometry of this problem is sketched in figure 2.14. In this figure R_m is the straight distance between the source location and the microphone location, R_t is the orthogonal distance between the source and the shear layer, Θ_m is the angle between wind tunnel axis and the source-microphone vector, Θ is the propagation angle, Θ_0 is the angle between the shear layer and the shear layer-microphone vector, also called the refraction angle. Θ' is the source emission angle. This emission angle is not equal to the propagation angle (Θ). The wave was originally emitted in the direction of Θ' but was swept downstream by the airflow.

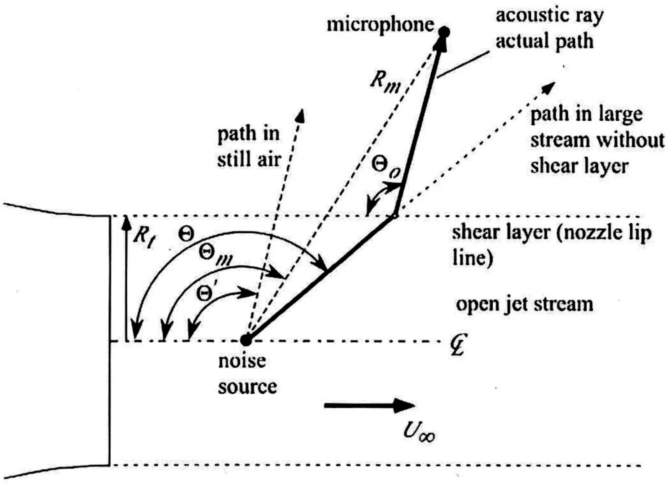

Figure 2.14: Shear layer refraction, (Allen et al., 2002)

From figure 2.14 and some basic geometric formulas the following relation can be derived:

$$R_m \cdot cos(\Theta_m) = R_t \cdot cot(\Theta) + (R_m \cdot sin(\Theta_m) - R_t) \cdot cot(\Theta_0) \tag{2.11}$$

The propagation angle is related to the emission angle by the following equation in which M is the free stream Mach number.

$$\Theta = tan^{-1}\left(\frac{sin(\Theta')}{cos(\Theta') - M}\right) \tag{2.12}$$

A relation between the refraction angle and emission angle is provided by Snell's law. In this relation c_0 is the speed of sound outside the jet while c_t is the speed of sound inside the jet.

$$M = \frac{1}{cos(\Theta')} - \frac{c_0/c_t}{cos(\Theta_0)} \tag{2.13}$$

Equations 2.11 - 2.13, can be solved iteratively for a given microphone position, source position and flow properties. This was done for M=0.3, $R_m/Rt = 4$ and $c_0/c_t = 1$ and very good agreement was found between the calculated values and table 1.2 provided in the works of Allen et al. (2002).

The refraction caused by a free shear layer poses some extra restrictions on the measurement. When sound waves are propagating parallel to the shear layer, they cannot cross it. This leads to a limit in shear layer to microphone angle that can be achieved, given by equation 2.14 (Allen et al., 2002). Due to this maximum angle, a zone of silence will occur around the jet, if only refraction is considered. A similar restriction applies in upstream direction. If sound waves are emitted at low angles, a limit will be reached where the wave will be completely reflected by the shear layer (Allen et al., 2002). The minimum propagation angle is given by equation 2.15.

$$\Theta_{0MAX} = 180 - cos^{-1}\left(\frac{1}{1+M}\right) \tag{2.14}$$

$$\Theta_{MIN} = 180 - cos^{-1}\left(\frac{-1}{1+M}\right) \tag{2.15}$$

Another artefact of shear layer refraction is that when a sound wave crosses the shear layer, it will be spread out over a larger area as can be seen in figure 2.15. Assuming that all acoustic energy is conserved, the sound pressure must decrease over the shear layer. Therefore the measured amplitude at the microphone will be lower when the sound has crossed a shear layer, compared to a measurement in still air. The relation given by equation 2.16 allows to correct for the difference in measured sound pressure (p'_b) to the actual sound pressure when no shear layer would be present (p'_c). The distances are derived from the geometry in figure 2.15 so that: $R_0 = \overline{bd}$, $R_a = \overline{ba}$ and $R' = \overline{en}$. The densities inside and outside the jet are represented by ρ_t and ρ_0 respectively.

$$p_c'^2 = p_b'^2 \left(\frac{\rho_t D_t^{-4}}{\rho_0}\right)\left(\frac{R_0 R_a}{R'^2}\right) \qquad with \qquad D_t = 1 - M \cdot cos(\Theta') \tag{2.16}$$

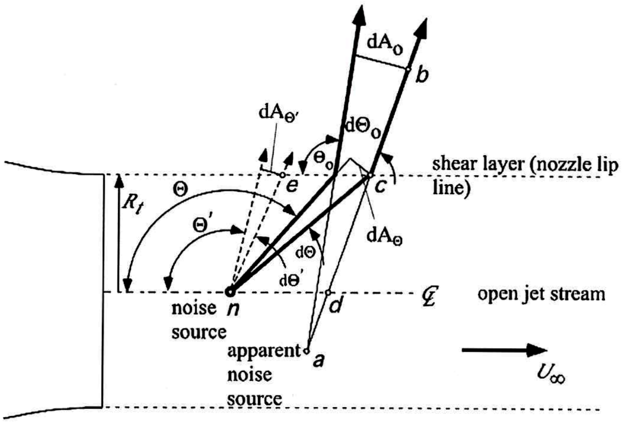

Figure 2.15: Wave spreading caused by shear layer, (Allen et al., 2002)

The suggested correction procedure by Allen et al. (2002) for shear layer refraction is as follows:

1. Calculate propagation geometry from equations 2.11 - 2.13 and use these values instead of un-refracted distances.
2. Apply microphone response corrections if necessary.
3. Correct for the sound pressure change caused by shear layer refraction using equation 2.16.
4. Correct for atmospheric absorption while propagating outside the jet.

The correction procedure given above is difficult and computationally expensive. Especially solving equations 2.11 - 2.13 is tedious since they have to be solved iteratively. A much faster and simpler method is suggested by Sijtsma (2010). In this faster method the elements of the simplified steering vector given by equation 2.3 are adapted to correct for the shear layer refraction. They are now given by:

$$g_m = \frac{-e^{-2\pi i f \Delta t_e m(X_m,\xi)}}{4\pi\sqrt{(\bar{M}_{corr}\cdot(X_m-\xi))^2+\beta^2\|X_m-\xi\|^2}} \qquad for \qquad m=1,2,..,M \tag{2.17}$$

with:

$$\Delta t_e m = \frac{1}{c\beta^2}\left(-\bar{M}_{corr}\cdot(X_m-\xi)+\sqrt{(\bar{M}_{corr}\cdot(X_m-\xi))^2+\beta^2\|X_m-\xi\|^2}\right) \tag{2.18}$$

Where $\bar{M}_{corr}$ is the average Mach vector between the source and the microphone and $\beta = 1 - \|\bar{M}_{corr}\|^2$. It is evident that when $\bar{M}_{corr} = 0$ the original formulation of the steering vector given by equation 2.3 is obtained. The method was compared to the more sophisticated method from Allen et al. (2002) and it was concluded that this simple method is valid for a Mach number below 0.25.

2.3.2 Different views on spectral broadening

When a sound wave passes trough a shear layer it does not only changes direction by refraction, but the frequency of a single tone also gets spread out over a wider (broader) range of frequencies. This phenomenon is referred to as spectral broadening. Because the phenomenon is complex and not completely understood, different theories on how the signal gets broadened exist. Three different views on the working principle of spectral broadening will be presented in this section.

Spectral broadening by time delay variations

Sulaiman (2011) suggests that spectral broadening is caused by a varying time delay on the signal. It states that the sound wave is mainly distorted by the large eddies in the shear layer. One part of the sound wave gets convected at a higher velocity while the other part is convected at a lower velocity. The effect of a single large eddie is depicted in figure 2.16. Tanking into account that there are many eddies in a shear layer, and they are convected along the shear layer leads to a very irregular pattern of time delay variations. These eventually lead to the change in amplitude and phase observed in spectral broadening. From figure 2.16 it can be derived that the approximated time the sound wave needs to pass through the shear layer is given by:

$$\Delta t = \frac{\delta_x}{c_0} \tag{2.19}$$

Where δ_x is the shear layer thickness and c_0 the speed of sound. In the work of Sulaiman (2011) it is assumed that the amplitude of the time delay variation, caused by the eddie, is half the maximum difference in time needed for the wave to cross the shear layer. This assumption leads to the following approximations for the amplitude of the time delay variation, a expressed in seconds:

$$a = \frac{1}{2}\left(\frac{\delta_x}{c_0 - v} - \frac{\delta_x}{c_0 + v}\right) = \frac{\delta_x v}{c_0^2 - v^2} \tag{2.20}$$

Where v is velocity of the eddie. Assuming this is much smaller than the speed of sounds allows for a simplification:

$$a = \frac{\delta_x v}{c_0^2} \tag{2.21}$$

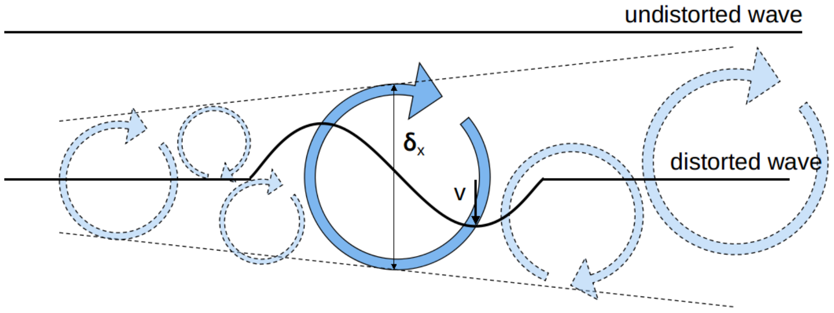

Figure 2.16: Spectral broadening by large eddie

Based on the same model, the location of the shoulders in the spectrum the can be predicted with equation 2.22, where U_c is the convective velocity of the eddie and l is the eddie length scale. The convective velocity of the eddie can be approximated by $U_c = U_\infty/2$ and the length scale could be approximated by the shear layer thickness, given by equation 2.9.

$$f_{shoulder} = f_{source} \pm \frac{\sqrt{2}}{2\pi}\frac{U_c}{l} \tag{2.22}$$

Spectral broadening by scattering

Another take on spectral broadening is presented by Krober et al. (2013). They state that when a sound wave passes through a shear layer it will be refracted as a result of the mean velocity gradient in a shear layer (indicated by Path I in figure 2.17), this was already discussed in section 2.3.1. The amplitude of this wave will be decreased since a part of the energy will be reflected (red arrow in figure 2.17). In addition to that it is stated in the report by Krober et al. (2013) that the sound wave will be scattered by the turbulent structures in the shear layer which causes the energy of the wave to be redistributed over different frequencies and directions. This is their interpretation of spectral broadening. In figure 2.17 it is indicated how that scattering would lead to the typical shape found by spectral broadening. Sound waves that are originally emitted in a different direction, (Paths II in figure 2.17) are affected by the directional scattering in the shear layer. As a result of that, these scattered waves end up in the same place as the unscattered wave represented by Path I. Due to the convection of the turbulent structures in the shear layer, the incident sound waves undergo a frequency

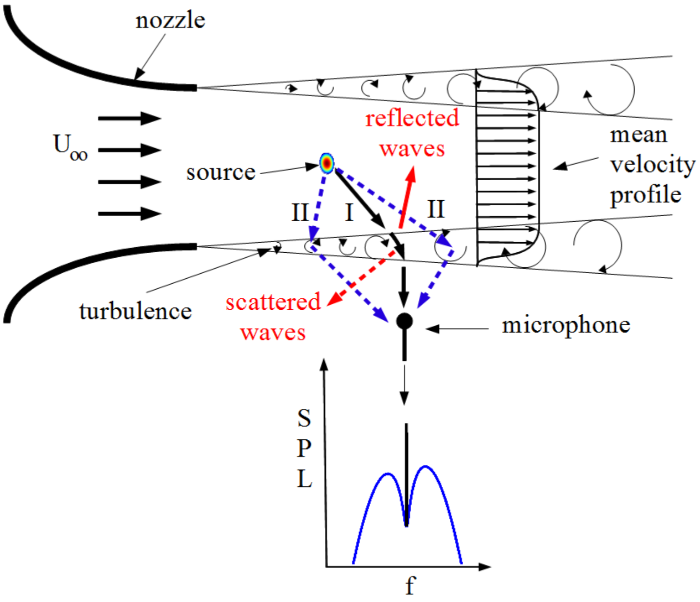

Figure 2.17: Spectral broadening by scattering of sound on turbulent structures, (Krober et al., 2013).

shift. The resulting frequency spectra found by this scattering is also depicted in figure 2.17. Note that in this figure the upper vortices should turn in the other direction.

Krober et al also make a distinction between weak and strong scattering. If the received frequency spectra of a single frequency source consists of a reduced peak with two side lobes, it is called weak scattering. When the original source frequency is completely lost by the broadened spectrum, it is referred to as strong scattering.

Spectral broadening by scattering and diffraction

A third view on the physical principles behind spectral broadening is presented by Campos (1977). In this case the shear layer is modelled by an irregular and unsteady interface across which the properties of the flow change discontinuously. Such a model is adequate when the wavelength of the sound wave is much larger compared to the scale of the turbulent structures. For high frequencies, with a small wavelength this model does not suffice. Therefore a correction based on geometric acoustics is applied to compensate for the interaction between the high frequency waves and the turbulent structures in the shear layer.

Figure 2.18 a represents the case were the wavelength is much larger than the shear layer thickness. In such a case the wave will be refracted as discussed in section 2.3.1 and part of the energy will be reflected by the shear layer. A theoretical derivation is made to calculate the reflected and transmitted energy, R and T respectively. They are expressed relative to the amplitude a_0, which is the amplitude of the sound with in a medium at rest. For a source within the jet the amplitude factor is given by:

$$a_1 = (1 - Mcos(\theta))^2 a_0 \tag{2.23}$$

Where M is the jet Mach number and θ the angle between the velocity of the jet and the angle of incidence. For this the transmitted and reflected energy are calculated as follows:

$$R = \frac{1 - a_1}{1 + a_1}; \qquad T = \frac{2}{1 + a_1} \tag{2.24}$$

As stated before these estimations for the transmission and refraction ratio are only valid for large wavelengths. For high frequency tones, the sound wave will interact with the turbulence inside the shear layer, as shown in figure 2.18 b. It is derived that the total phase-shift caused by the turbulent shear layer is proportional to the mean wave number and Mach number of the turbulence. So for a high frequency tone, the total distortion will consist out of transmission and reflection effects caused by the difference in fluid properties, combined with a phase distortion caused by the turbulence in the shear layer.

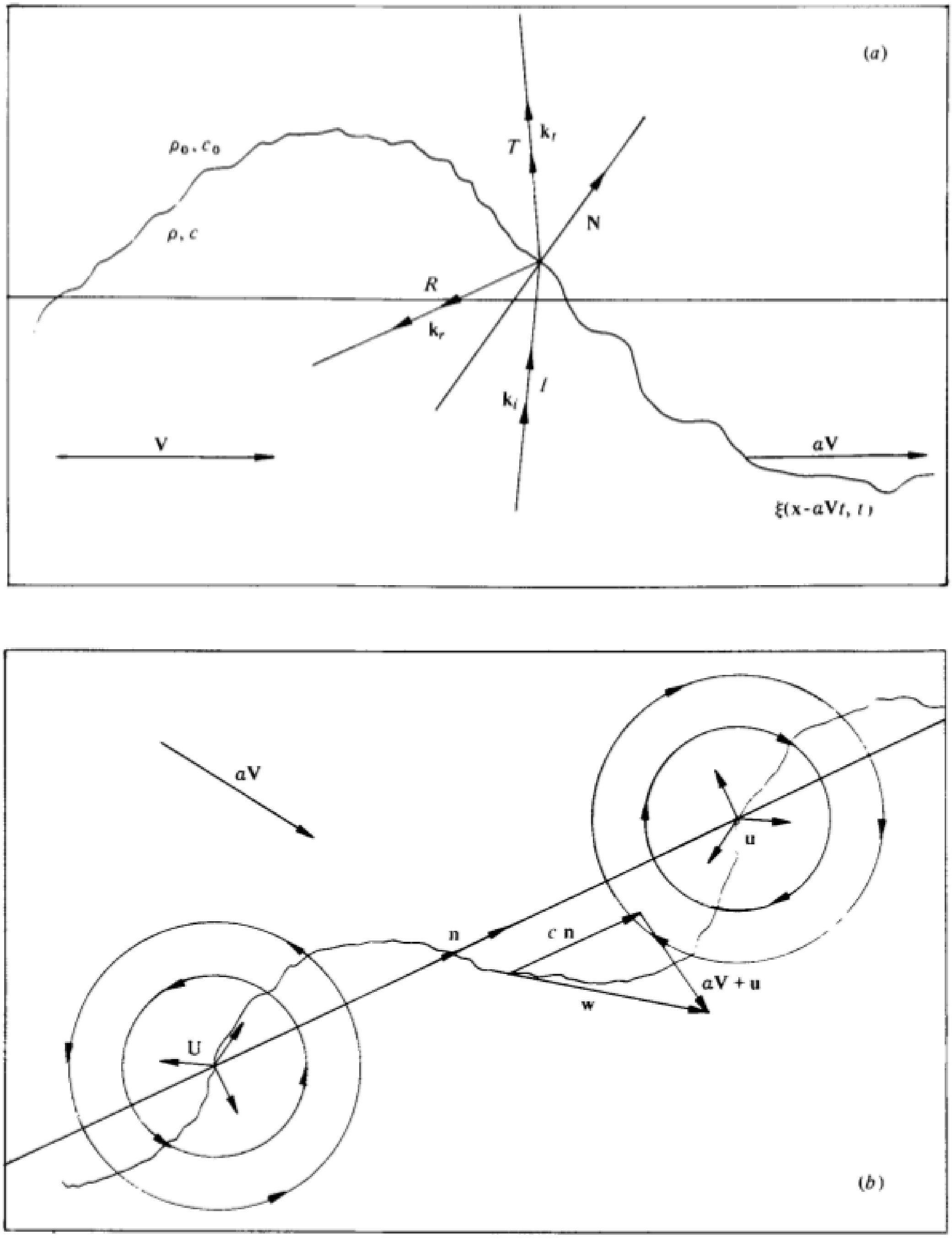

Figure 2.18: (a) Scattering by an irregular unsteady interface, (b) Diffraction of rays in a region of turbulence, (Campos, 1977).

2.3.3 Experimental characterization of spectral broadening

Both Sulaiman (2011) and Krober et al. (2013) present an experimental investigation on spectral broadening. The results of the two investigations are in good agreement. The most relevant results from Sulaiman (2011) will be presented here to indicate the relation between the amount of spectral broadening and the flow properties or acoustic path. In these experiments done by Sulaiman (2011) a source was mounted flush in an extension plate at the exit of an open jet wind tunnel. On the other side of the open jet a series of calibrated microphones were placed to determine the spectral broadening through a shear layer. A schematic representation of the experimental setup used by Sulaiman (2011) is given in figure 2.19. The shear layer was characterised with the use of a hot wire anemometer, for more details about the hardware and data acquisition system see the report of Sulaiman (2011).

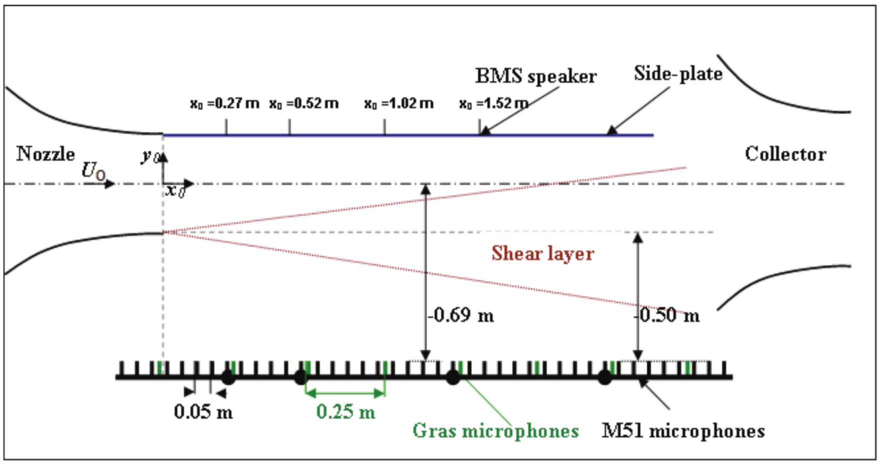

Figure 2.19: Top view of experimental setup used by Sulaiman (2011)

Firstly the influence of flow velocity was investigated by keeping the source and microphone position fixed and the frequency constant to 4 kHz. Figure 2.20 indicates that the spectral broadening is worse at higher free stream velocities. During the second measurement series the velocity was kept constant at 60 m/s and the frequency of the source signal was varied. It is clear from figure 2.21 that higher frequency signals are affected much more by the shear layer. This is because the size of the turbulent structures becomes larger compared to the wavelength of the sound waves at higher frequencies. For 32 kHz and higher the original peak (source frequency) has disappeared, which indicates strong strong scattering.

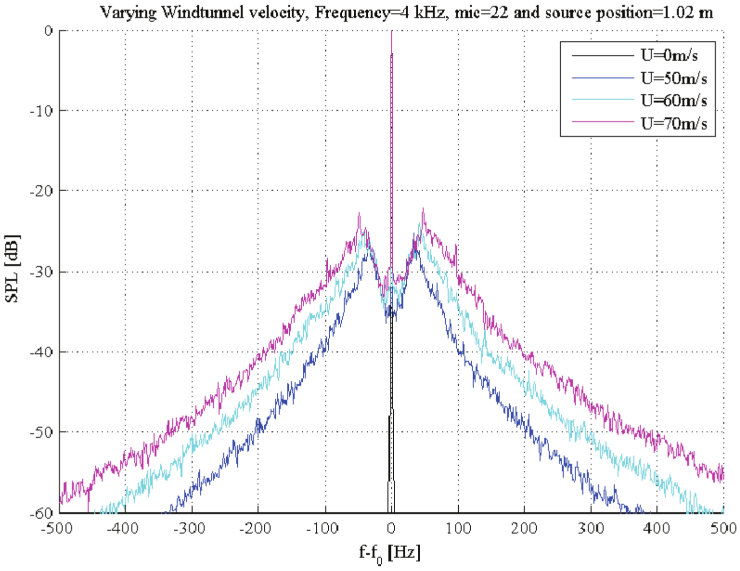

Figure 2.20: Spectra for varying flow speed, source at f=4 kHz, (Sulaiman, 2011)

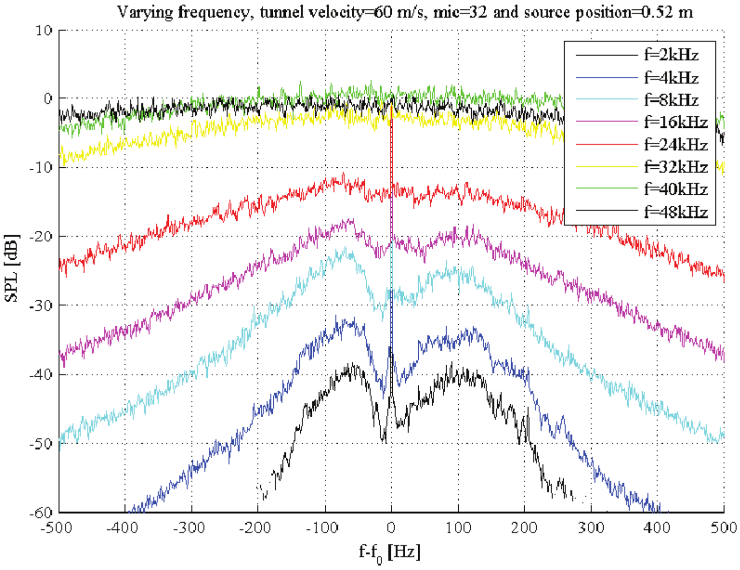

Figure 2.21: Spectra for varying frequency at U_∞ =60 m/s, (Sulaiman, 2011)

During the third test series the axial position of the source and receiving microphone were varied. This was done to evaluate the influence of the shear layer thickness. The more downstream, the thicker the shear layer will be. From figure 2.22 it can be seen that for a thinner shear layer the source peak is more distinguishable; the difference between the peak level and shoulder level is higher. During the next test series the axial position of the receiving microphone was again varied but this time the source position stayed fixed. Microphone 37 was on the same axial position as the source which was producing a tonal noise of 8 kHz and the flow speed was 60 m/s. A lower microphone number corresponds with a more upstream position while a higher microphone number is placed further downstream. During this test several effects have a role on the received signal. A more downstream microphone position means that the sound has to pass through a thicker shear layer, this will increase the spectral broadening as observed in the previous test. In addition to that the increased angle between the source and the microphone will lead to an oblique path through the shear layer. This causes an even longer path through the shear layer compared to an aligned microphone leading to even more spectral broadening, see figure 2.23.

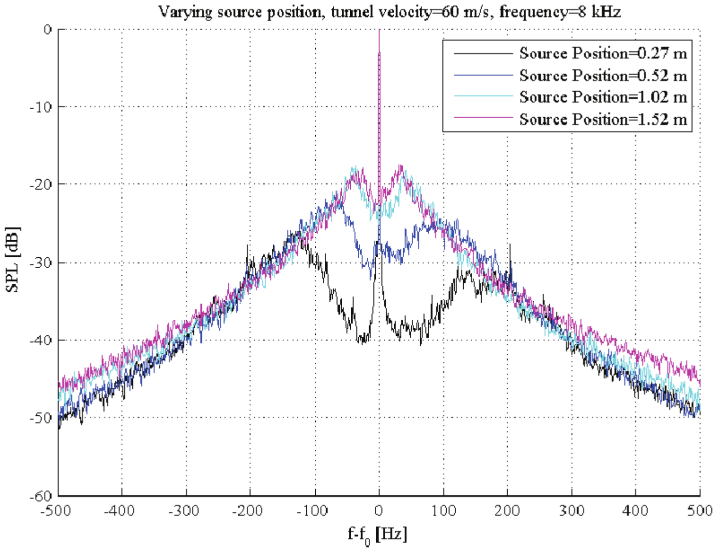

Figure 2.22: Spectra for varying source position, source at f=8 kHz and U_∞ =60 m/s, (Sulaiman, 2011)

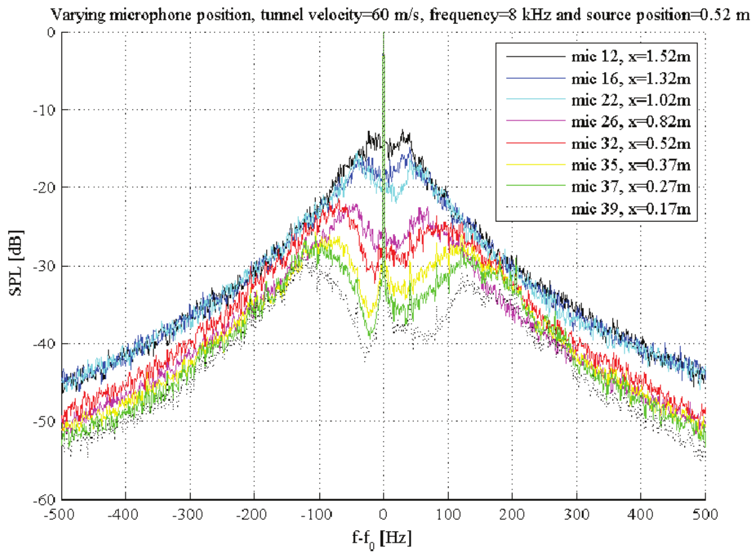

Figure 2.23: Spectra for varying microphone position, source at f=8 kHz and U_∞ =60 m/s, (Sulaiman, 2011)

2.4 Conclusions

The major drawback of performing aero-acoustic measurement in an open jet wind tunnel is the distortion of the sound waves caused by the free shear layer. The sound wave will be refracted because of the different propagation properties inside and outside the jet. In addition to that the frequency spectrum of the wave will be broadened due to the interaction between the sound wave and the turbulent structures inside the shear layer. This spectral broadening is particularly problematic when examining objects which produce a tonal noise, e.g. open rotors, vortex shedding. Spectral broadening of a sound wave propagation through a shear layer has been investigated by several institutes and to reduce the effects, the use of an acoustically transparent wall is suggested.

Chapter 3

Previous work on ATW

In a conventional wind tunnel facility where acoustic testing is done, the sound can escape from the flow by using an open jet configuration. This implies that the flow is both acoustically and aerodynamically open. This aerodynamically open flow leads to large turbulent structures which interact with the sound waves passing through them, as explained in section 2.3. The aim of using an acoustically transparent wall (ATW) in a wind tunnel is to create a test section that is acoustically open but aerodynamically closed. This would greatly reduce the turbulence at the interface and therefore the interaction with the sound waves. Different attempts have been made to improve aero-acoustic wind tunnel measurements by eliminating the shear layer by installing an ATW. The main results from various works will be presented in this section. Initially wall mounted microphones were recessed over a small distance and covered with an acoustically transparent material. After this the transparent material was used in open jet facilities to form a acoustically transparent wall (ATW).

3.1 Reduction of microphone self noise

An innovative solution to reduce the microphone self noise created by the interaction between the turbulent boundary layer and the microphone, was presented by Jaeger et al. (2000). In his improved configuration the microphones were no longer mounted flush into the wind tunnel wall, but were recessed (by 12.7 mm) in order to separate them from the flow. Secondly the microphones were covered with a porous material that should act like an aerodynamic surface but must allow sound to pass through. This concept is schematically represented in figure 3.1(a) and a photograph of the final implementation is shown in figure 3.1(b). From previous test it was concluded that the optimal material would be a thin, light, porous surface with low acoustic impedance but strong enough to act as an aerodynamic surface. This surface would then be tensioned over the microphone array similar to a how drum head is tensioned over a rim.

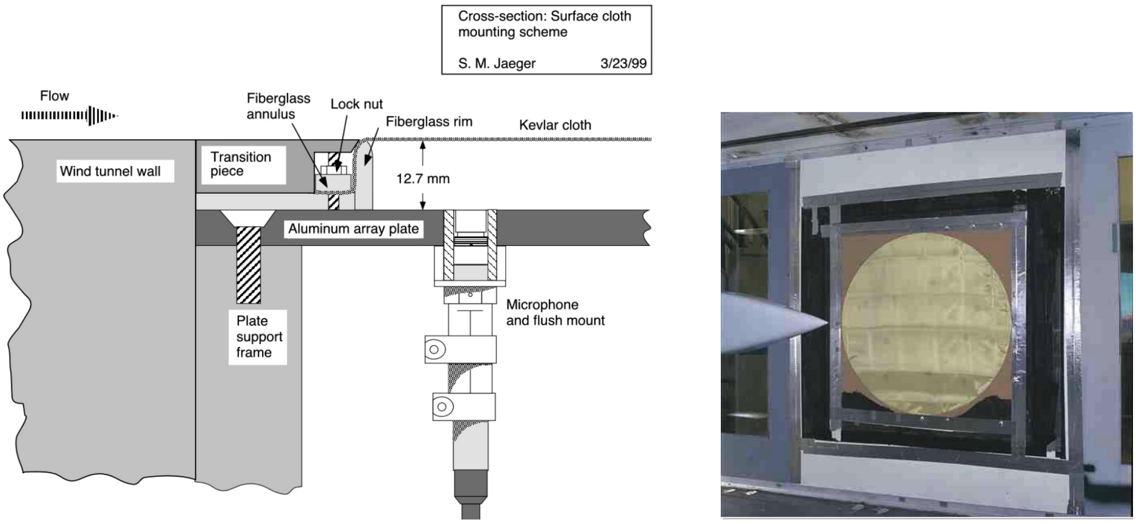

(a) Cross-sectional view of recessed array design

(b) Photograph of recessed 70 element array with Kevlar cloth

Figure 3.1: Implementation of recessed array design, (Jaeger et al., 2000)

Three materials were selected for testing: Technetics FM-125 fibreglass cloth, 100 MKS Rayl stainless steel and Kevlar. The fibreglass cloth disintegrated immediately when the wind tunnel was running because of its low resistance to shear forces. The stainless steel sheet performed better but fatigued under unsteady loads. The Kevlar performed excellent as surface material. Therefore three different types of Kevlar were selected for further testing: Kevlar 120 (7.9 $gram/cm^2$) thin weave, Kevlar 124 (7.9 $gram/cm^2$) crow's foot weave and Kevlar 500 (22.0 $gram/cm^2$) thick weave. It was found that the thick weave Kevlar influenced sound passing through the cloth a lot, the distortion caused by the thin weave and the crow's foot weave was much lower as can be seen in figure 3.2. Both these weaves were used in wind tunnel test and found to be working well.

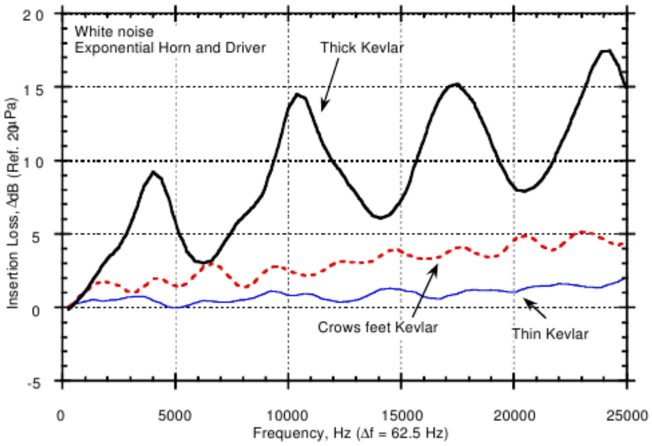

Figure 3.2: Amplitude loss through different materials, (Jaeger et al., 2000)

3.2 Acoustically transparent walls

The idea of adding an acoustically transparent wall (ATW) to an open jet wind tunnel was investigated very early by Bauer (1976). The basic concept is to extend the open jet wind tunnel exit with an aerodynamic surface that eliminates a turbulent shear layer from developing and replaces it with far less turbulent boundary layer. This would lead to less spectral broadening of the signal and less coherence loss for acoustic microphone arrays. The key here is to obtain an aerodynamic surface that confines the flow and allows sound to propagate through it with as little distortion as possible. This is similar to the material required for reducing the microphone self noise.

Bauer (1976) wanted to perform acoustic measurements on aircraft models and components. An open jet facility was not sufficient for his needs because the rapid growth of the shear layer thickness limited the size of the models and the increased background noise from the turbulence inside the free shear layer polluted the measurements. To eliminate both these problems Bauer (1976) used a material called Brunsmet. It consists out of a stainless steel perforated backing plate covered with many fine steel wires on one side. The steel wires are sintered together to the back plate. The back plate had a thickness of 0.635 mm and the hole diameter was 1 mm. The overall open area of the back plate was 34 %.

Bauer mainly tested the concept for amplitude loss. The ATW was mounted on one side of the wind tunnel while the other side was hard walled. The drive fan of the wind tunnel was used as natural noise generator. No research was done with a model or controlled source in place. The calibrated microphone was then placed 40 inches behind the ATW as can be seen in figure 3.3(a). It was concluded that the transmission loss through the ATW was low, a sound pressure level drop of 1 dB was found uniformly over all frequencies, as indicated by figure 3.3(b). Furthermore high frequency noise was observed, the noise is probably due to the interaction of the boundary layer with the holes in the back plate. It is suggested that a different type of supporting structure for the fine steel wires may resolve this effect.

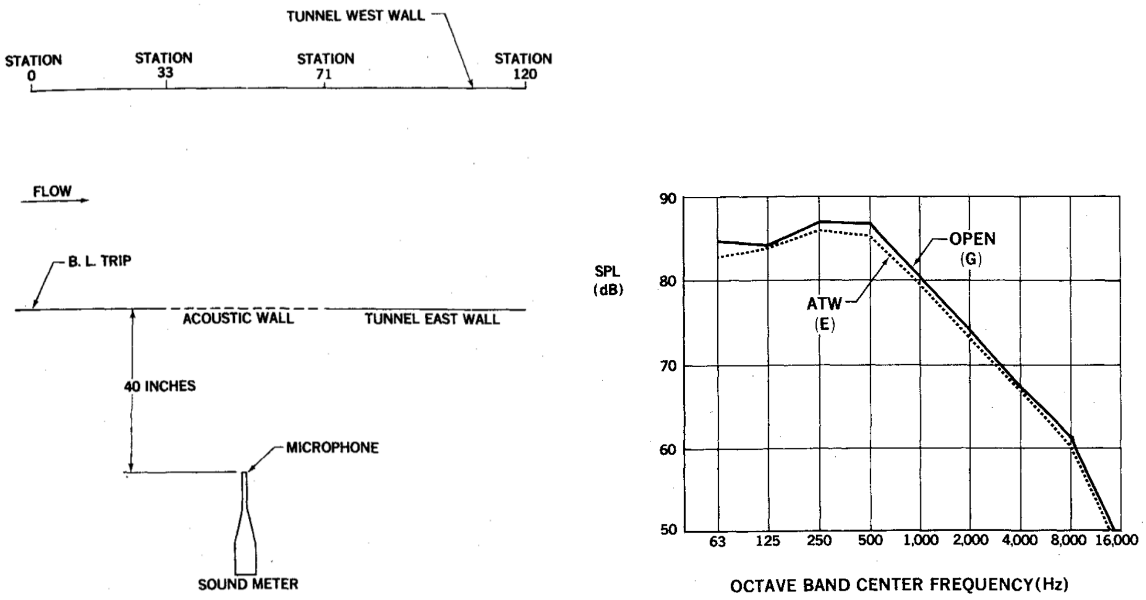

(a) Test setup used by Bauer (1976)

(b) Comparison of sound transmission in open and ATW configuration

Figure 3.3: Test setup and sound transmission results, (Bauer, 1976)

The research done by Jaeger et al. (2000) inspired people at Virginia Tech to convert their stability wind tunnel into an aero-acoustic wind tunnel (Carmargo et al., 2005) (Remillieux et al., 2008). To achieve the best possible environment for aero-acoustic testing, they tried to eliminate all current issues with acoustic facilities by using a new wind tunnel design. The main interest with respect to this research is the test section. The test section is fully closed and incorporates two large Kevlar windows for acoustical transparency. The other parts are perforated metal bonded with Kevlar, to minimize reflections in the closed section. The Kevlar windows are tensioned to prevent deformation under load. Behind the two Kevlar windows two anechoic chambers are constructed. These eliminate all reflections above 140 Hz. A horizontal cross section and several dimensions of the wind tunnel can be seen in figure 3.4.

Many aerodynamic, acoustic and calibreation tests were performed on this aero-acoustic facility, an extensive discussion on those test can be found in the report of Carmargo et al. (2005). The most relevant results and conclusions with respect to this research project will be discussed here. First of all it was found that the Kevlar walls lead to a boundary layer as opposed to a free shear layer. The thickness of the boundary layer was roughly twice the thickness of the original hard-wall test section. The overall noise level in the test section was reduced by 10 to 16 dB, this is however not only due to the Kevlar windows but also due to acoustic treatment of the whole circuit. Aerodynamic test have shown that the correction required for the lift interference is reduced by 40 to 50 % when compared to a free jet. Finally phased array measurements were performed as practical demonstration of acoustically transparent test section.

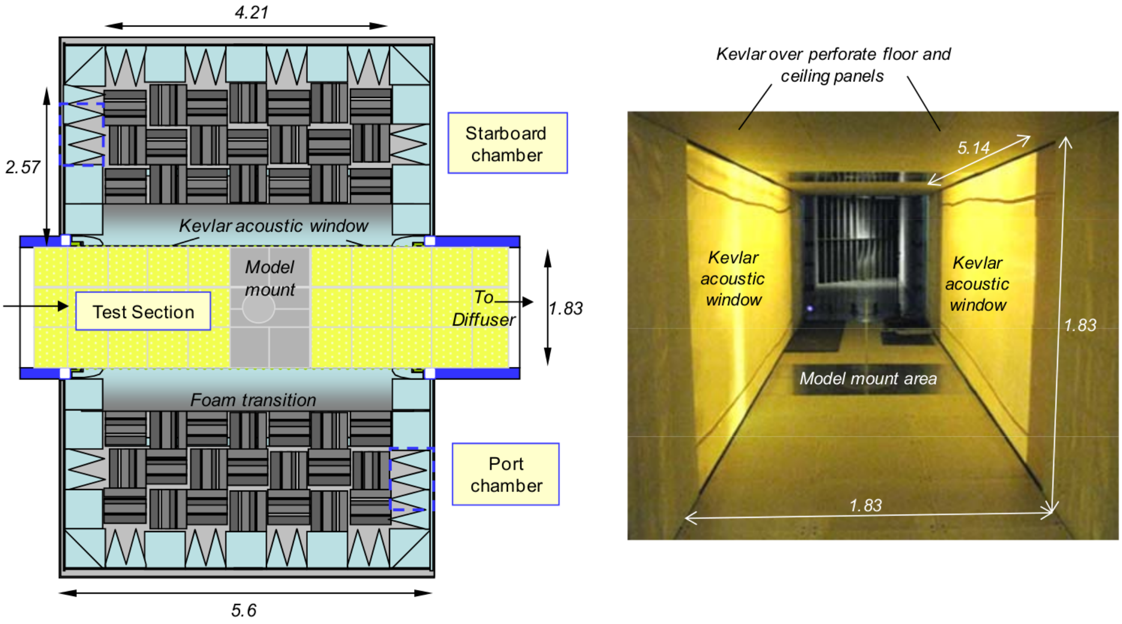

Figure 3.4: Left: horizontal cross section of VT stability wind tunnel and anechoic chambers. Right: photograph of the test section with Kevlar ATW, photo taken from upstream. Dimensions in meters. (Remillieux et al., 2008)

The successful conversion of the Virginia Tech stability wind tunnel into an aero-acoustic wind tunnel inspired several other institutes to investigate the use of Kevlar as acoustically transparent material. The Japanese Aerospace Exploration Agency (JAXA) also converted their stability wind tunnel to an acoustic facility based on the work done at Virginia Tech (Ito et al., 2010). They followed the same concept of Kevlar windows with anechoic chambers behind them. This Second successful implementation validated the concept.

Since the configuration implemented at Virginia Tech and JAXA is a major change to the wind tunnel test section, it is a long and expensive process. A more simple alternative was investigated at the NLR (Nationaal Lucht- en Ruimtevaartlaboratorium). At the NLR an acoustically transparent extension plate for the KAT (kleine anechoische tunnel, *small anechoic tunnel*), was designed and tested (van Dun and Tuinstra, 2011). This omitted the need for redesigning and building a whole new test section, but still transformed the shear layer into a boundary layer. Since the jet already exited in an anechoic environment, there was no need to add anechoic chambers behind the ATW. The acoustically transparent wall mounted at the jet exit was again constructed from tensioned Kevlar, as shown in figure 3.5.

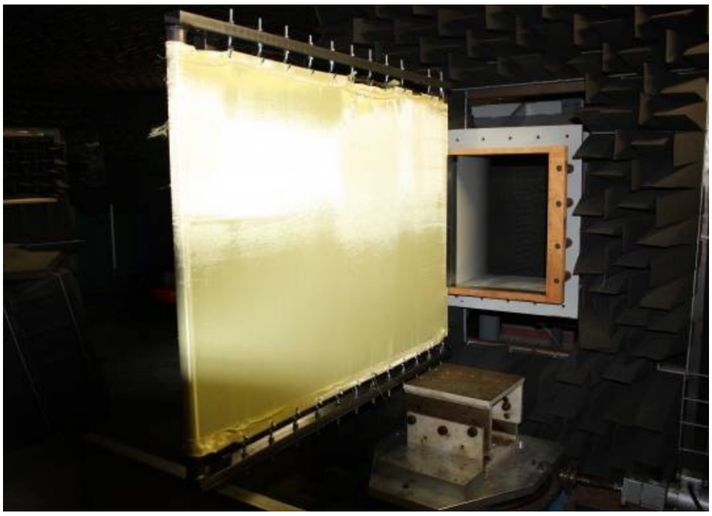

Figure 3.5: Jet exit of KAT wind tunnel with ATW extension plate (van Dun and Tuinstra, 2011)

The newly designed acoustically transparent screen was tested both aerodynamically and acoustically at the NLR. The results from the aerodynamic test confirmed the stability of the construction. More importantly the acoustic test revealed much less spectral broadening of the signal when the screen was installed. Various frequencies were tested at a flow speed of 60 m/s. The measured spectra can be seen in figures 3.6(a) and 3.6(b). A much more distinguishable peak is visible when the ATW was installed. The remaining challenges stated in the report of van Dun and Tuinstra (2011) are: the high self noise of the wall and the Kevlar material which is tedious to work with.

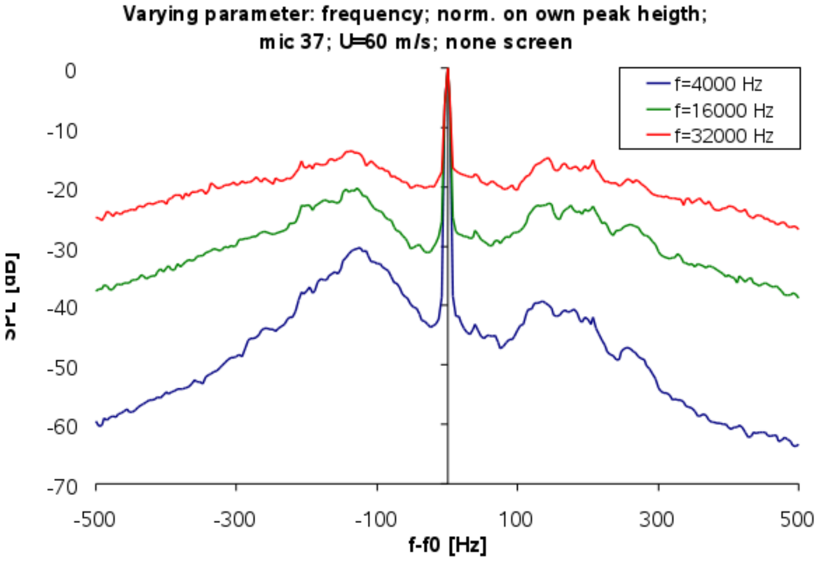

(a) Without screen

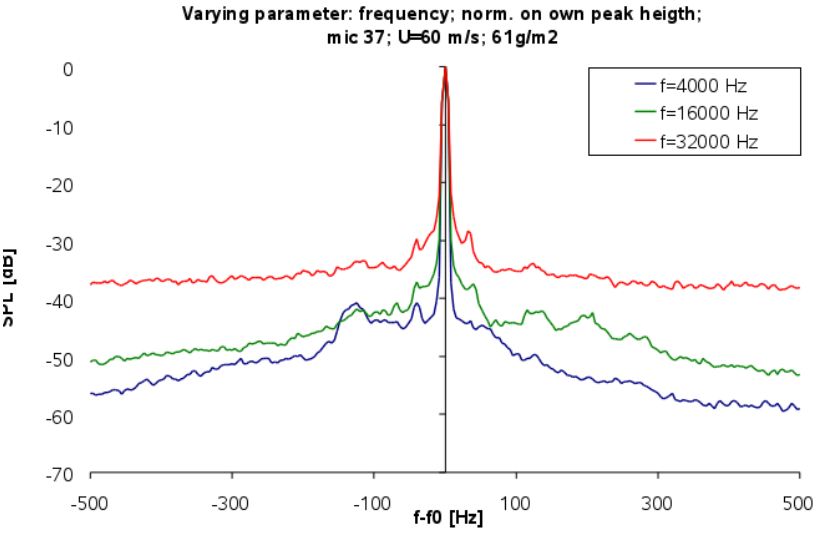

(b) With screen

Figure 3.6: Spectra acquired through shear layer (a) or through ATW (b) indicating spectral broadening at different frequencies, (van Dun and Tuinstra, 2011)

3.3 Conclusions and problem statement

The implementation of an acoustically transparent wind tunnel test section has been done in a few institutes. In all cases they have significantly improved aero-acoustic measurements by reducing the distortion (spectral broadening) of the sound signal. With this less distorted signal more accurate sound source localisation could be done by the beamforming algorithm. However, so far these ATW's have not been characterized in detail. Although they distort the sound signal much less when compared to a turbulent shear layer, some effects remain and new distortions are found. In general the spectral broadening (mainly caused by turbulence (Sulaiman, 2011)) is greatly reduced, but the ATW damps the sound wave leading to a smaller amplitude (Jaeger et al., 2000). Furthermore the addition of an ATW produces noise itself. Current ATW configurations are made from tensioned Kevlar cloths. These are not only expensive and difficult to produce but also tedious to work with for skin and lungs. The main objective of this research project is to improve aero-acoustic wind tunnel measurements by evaluating the acoustic and aerodynamic properties of an acoustically transparent test section compared to a traditional open jet configuration. As alternative to the currently used tensioned fiber weave materials, the potential of perforated plates as ATW will be evaluated.

3.3.1 Problem statement

From the section on sound propagation trough a turbulent shear layer in the previous chapter (section 2.3) it is evident that spectral broadening of the signal is the main unwanted phenomenon observed during open-jet acoustic measurements. The higher the velocity of the flow or the frequency of the signal becomes, the more energy is broadened from the peak to the shoulders. Figure 2.21 already showed the scale of this problem and that eventually at very high flow speeds or source frequencies, the original peak disappears completely. This means that the agreement between the real-word problem being investigated and the experimental representation of it in the wind tunnel is reduced. The spectrum measured with a single microphone will include the shoulders and the peak energy will be reduced. Spectral broadening does not only affect single microphone measurements but also has a detrimental effect on acoustic array measurements. The distortion caused by the shear layer will reduce the coherence between the microphones in the array. This limits the size and thus resolution of the array.

Initially one might think that these very high, not audible, tonal frequencies are not relevant an thus the phenomenon of spectral broadening is not troublesome. Hover physically scaling down a model to fit in the wind tunnel will result in higher frequencies generated by the airflow. In other words a sound of 32 kHz measured on a model aircraft could correspond to a 3200 Hz sound on the actual aircraft, making these high frequency sounds very relevant for wind tunnel testing. The broadening of tonal noise becomes more and more troublesome when examining contra rotation open rotors and propellers in open jet wind tunnels. Since these cases have very distinct peaks in their spectrum. The reduced coherence in a microphone array limits any open jet wind tunnel measurements were a high spatial resolution is required.

The use of an acoustically transparent wall projects many benefits for aero-acoustic testing. The effect of spectral broadening will be greatly reduced since both the thickness of the turbulent layer and the turbulent intensity is reduced over a wall bounded shear layer compared to a free shear layer. These two parameters directly determine the amount of spectral broadening as indicated by equation 2.21. This means that at high flow speeds and high tonal frequencies the signal will not be lost because of the extensive broadening and at lower frequencies more energy will remain in the peak. Secondly for microphone array measurements it means that the coherence between the microphones will be increased and thus a higher resolution can be achieved. An additional benefit of using acoustically transparent walls is that the test section now becomes semi-closed instead of open. This improves aerodynamic measurements and might allow acoustic and aerodynamic measurements to be carried out simultaneously. Carrying out aerodynamic and acoustic measurements at the same time would introduce a time saving during testing. The aerodynamic benefits of an acoustically transparent test section are however beyond the scope of this research and therefore not further investigated.

3.3.2 Summary of research methodology

From the theory presented in chapter 2 it was derived that a good acoustically transparent wind tunnel wall must allow sound waves to pass through it with as little distortion as possible. In addition to that the ATW must confine the flow and lower the amount of turbulence without causing any major disturbance to the flow. Since the ATW must fulfil both an acoustic and an aerodynamic purpose it was decided to initially investigate the acoustic and aerodynamic characteristics separately. At first acoustic measurements were performed to characterize how different porous material transmit sound waves. Secondly an aerodynamic investigation of the boundary layer over these porous materials was carried out. From those experiments the turbulent parameters related to spectral broadening (wall normal fluctuations v' and shear/boundary layer thickness δ) could be extracted. Finally the acoustic and aerodynamic effects were combined in a series of aero-acoustic wind tunnel measurements. This allows for an evaluation and performance analysis of the complete system.

Chapter 4

Experimental apparatus and set-up

During this research project multiple experimental campaigns aim to determine the characteristics of various acoustically transparent materials. The goal of this chapter is to outline the different materials and experimental set-ups used. First the acoustic and aerodynamic properties of different materials were investigated separately, only in the final stage the combination of sound waves with a flow field was considered. This leads to three different set-ups.

4.1 Acoustically transparent materials

The porous materials selected for these experiments where chosen based on previous applications of such materials and availability. A thin weave Kevlar cloth was included because it is a common choice for constructing an acoustically transparent wall (Remillieux et al., 2008), (van Dun and Tuinstra, 2011). As alternative to Kevlar, a glass fiber cloth was selected because it is cheaper and less stiff compared to Kevlar. The low stiffness should make tensioning the cloth more easy. The weave of both the Kevlar and glass fiber material is shown in figures 4.1(a) and 4.1(b) respectively. The fibrous materials were incrementally tensioned on a table and held in place by tape. When the desired level of tension was obtained they were placed onto a wooden frame where they were kept in place by double sided tape. One of the main recommendations by van Dun and Tuinstra (2011) is to search for different materials than Kevlar since it is tedious to work with and can irritate skin and lungs. It is suggested to explore the possibilities of perforated plates, which allows for easy constructions and can be made out of a non hazardous material. Therefore two perforated metal plates were included for examinations. Both had the same hole-pattern which is depicted in figure 4.2, but were made from different materials and had a different thickness. The hole centres are 5 mm apart and had a diameter of 3 mm, resulting in an opera area percentage of 32 %. The final selection of materials and their relevant properties are summarized below. In most cases the effect of these different porous materials will be evaluated by comparing them with the a clean configuration where no material is present.

- Kevlar cloth: density: 61 g/m^2, thickness: 0.12 mm, open area: 65%
- Glass fiber cloth: density: 80 g/m^2, thickness: 0.088 mm, open area 65%
- Perforated steel: thickness: 2 mm, hole diameter: 3 mm, open area: 32%
- Perforated aluminium: thickness 1 mm, hole diameter 3 mm, open area: 32%

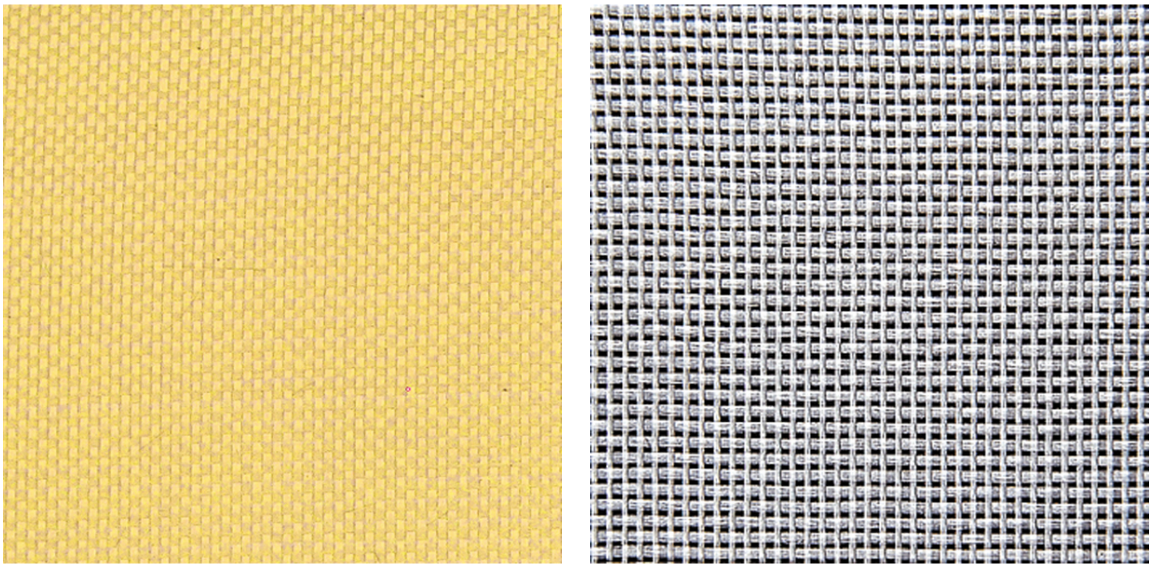

(a) Kevlar

(b) Glass fiber

Figure 4.1: Photographs of fiber weave materials, source: http://shop1.r-g.de

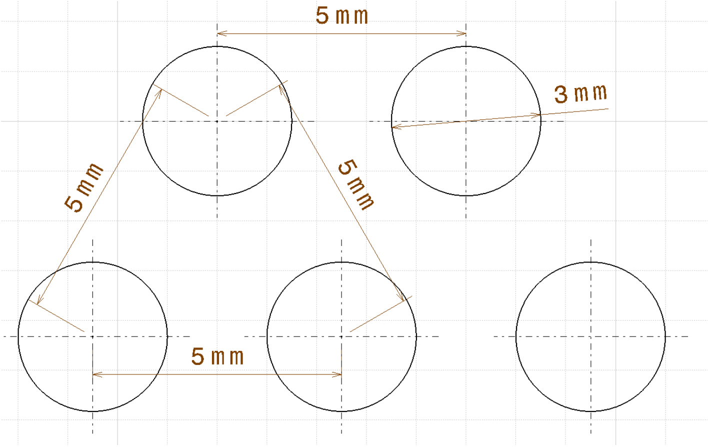

Figure 4.2: Hole pattern of perforated plates

4.2 Acoustic transmission experiments

A good acoustically transparent wall should allow sound waves to pass through with as little distortion of the wave as possible. To investigate how the selection of porous materials listed in the previous section allow sound transmission, a series of microphone measurements were conducted in an anechoic chamber. This section outlines the experimental set-up, how the microphone data was processed and the test program.

4.2.1 Experimental set-up

To eliminate background noise and reflections, the measurements were conducted in the anechoic chamber of the faculty of applied science at the TU Delft. The wedges installed in the room have a height of 1 m which means they damp out all sound waves above 80 Hz. A photograph of the test set-up is shown in figure 4.3(a) and sketch of the top view is given by figure 4.3(b). A MC-501 speaker was placed at a distance of 40 cm away from the material specimen. This corresponds to the width of the wind tunnel test section used for the aero-acoustic experiments. Sound absorbing foam was used to form a tunnel from the speaker to the material to ensure no sound would refract around the material. Note that in figure 4.3(b) only the side-walls are drawn, the top and bottom part were also closed with the same sound absorbing material. Behind the material specimen a B&K free field microphone (type 4190) was placed to record the signal. The microphone was connected to a B&K type 2669L pre-amp and a B&K Nexus conditioning power supply type 2690-52. The technical properties of this microphone system are summarized in table 4.1 The microphone signal was recorded using a computer with an ADI SoundMAX AD1984A audio card. The speaker was powered by a simple E60 amplifier module which was controlled by the same host computer. The amplifier had only one setting which was the gain. All measurements were done with the same gain setting for the amplifier, except for one signal which was produces with a 10 dB lower gain.

Table 4.1: Technical specifications of single microphone system

Property	Quantity
Microphone diameter	0.5 in
Frequency range	6.3 Hz - 20 kHz
Dynamic range	14.6 - 146 dB
Inherent noise	14.6 dB A
Sensitivity	50 mV/Pa

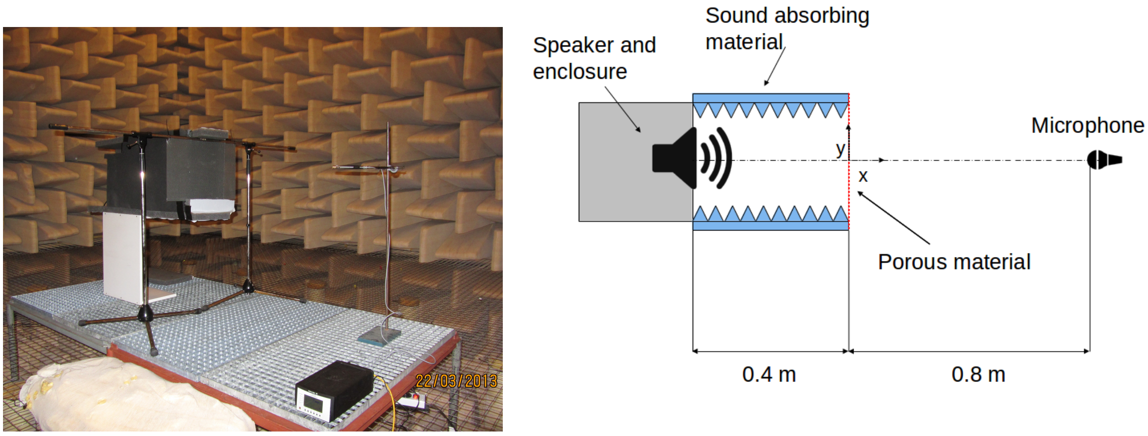

(a) Photo of experiment

(b) Top view sketch

Figure 4.3: Test set-up of acoustic transmission measurements

4.2.2 Microphone data processing

All processing of the recorded signal was done with a combination of Matlab and Python scripts. A fast Fourier transform (FFT) was used to calculate the direct Fourier transform of the recorded signal and convert the time domain microphone signal to a frequency domain spectrum. The resulting frequency spectra were calibrated using a B&K type 4231 acoustical calibrator which produced 94 dB at 1000 Hz. By taking the recorded power at 1000 Hz during the calibration measurement and using it as a reference value in equation 4.1, the frequency spectra could be calibrated. Figure 4.4 shows the spectrum from the calibration measurement after calibration, a 94 dB peak at 1000 Hz confirms the calibration.

$$X_{dB} = 20 * log_{10}(\frac{V}{V_{ref}}) + 94\ [dB] \tag{4.1}$$

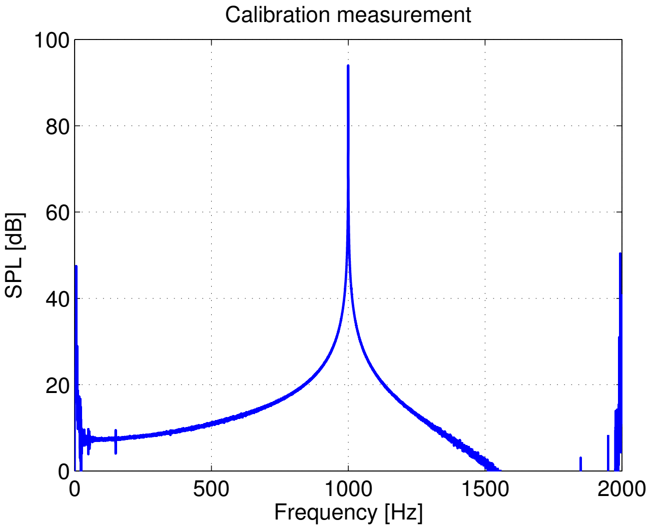

Figure 4.4: Frequency spectrum after calibration

To determine the spatial amplitude variations during the second series of measurements the root mean square (rms) value of the recorded signal was calculated. For a discrete set of samples $x_1, x_2, .., x_m$ with m elements the rms value is given by equation 4.2. For a pure sine wave the rms value of the signal should correspond to the amplitude of the wave divided by $\sqrt{2}$.

$$x_{rms} = \sqrt{\frac{1}{m}(x_1^2 + x_2^2 + ... + x_m^2)} \tag{4.2}$$

4.2.3 Test program for microphone measurements

For the first series of acoustic transmission measurements the microphone was placed at an axial position of 0.8 m behind the material specimen as shown in figure 4.3(b). At 0.8 m behind the material specimen all sounds above 1000 Hz can be considered to be in the far-field, which is typically the case for microphone measurements in a wind tunnel environment. All materials listed in section 4.1 were compared to the case where no material specimen was present. To determine their acoustic characteristics four different source signals were used each 10 seconds long (t_e). The five configurations tested and the five types of source signals are summarized below.

Configurations
- Clean, reference measurement
- Glass fiber cloth
- Kevlar cloth
- Perforated steel plate
- Perforated aluminium plate

Signals
- Pure harmonic tones at 100, 500, 1000, 2000, 3000 Hz
- Frequency sweep from $f_0 = 1$ Hz to $f_e = 20$ kHz, from equation 4.3
- Frequency sweep from $f_0 = 1$ Hz to $f_e = 6$ kHz, from equation 4.3
- Same frequency sweep from 1 Hz to 6 kHz with a 10 dB lower amplitude

$$f(t) = f_0 + kt \qquad with \qquad k = \frac{f_e - f_0}{t_e} \tag{4.3}$$

During the first test series a repetitive pattern in the acoustic power transmission coefficient measured through both perforated plates was observed at higher frequencies. To further investigate this transmission coefficient pattern, the relation between this pattern and the position of the microphone was examined. Since both perforated plates showed the same pattern only the perforated steel plate was used for this series of measurements. Initially the x-position (defined in figure 4.3(b)) of the microphone was varied from 2 cm to 50 cm behind the plate in steps of 2 cm whilst keeping the y-position (lateral) constant. For the second series the microphone was placed 31 cm behind the perforated plate, after which the lateral position was increased until 32 cm in steps of 2 cm. During this series of measurements two source signals were used. Again a frequency sweep form 1 Hz to 20 kHz was used, but this time the sweep had a duration (t_e) of 60 seconds, to increase the frequency resolutions. In addition to that pure harmonic tones from 6000 Hz to 7000 Hz in steps of 100 Hz were used as well.

4.3 Aerodynamic experiments of the shear and boundary layer

The second experimental investigation in this research project is towards the aerodynamic properties of a turbulent boundary layer over different porous materials. From the theory outlined in section 2.3.2 it is clear that turbulent structures cause distortion on a sound wave. More specifically the thickness of that turbulent region and the velocity fluctuations in the direction of the propagating sound wave are in direct relation to the amount of distortion, as demonstrated by equation 2.21. Therefore these aerodynamic measurements aim to determine the thickness of the boundary layer over different porous materials as well as the velocity fluctuations normal to the free stream (v'). Since in a typical open-jet configuration these correspond to the velocity fluctuations in the direction of the propagating sound wave. For reference a solid wall was included and for comparison the center part of a free shear layer was measured as well. The aerodynamic parameters were determined by performing a series of particle image velocimetry (PIV) measurements. The technique of PIV was selected because it captures instantaneous velocity vector fields which means that u and v can be analysed separately. A series of these vector fields would then yield the desired statistical quantities of the flow. This section will present the experimental apparatus used and the set-up of the experiment.

4.3.1 Experimental set-up and data acquisition

The M-tunnel at the aerodynamics laboratories of the TU Delft was used in its open jet configuration, which means the maximum velocity was limited to 35 m/s. The exit of the wind tunnel is 0.4 m by 0.4 m. The free stream velocity in the wind tunnel was measured by a pitot tube connected to a Mensor digital pressure gauge, model 2101. A small Labview program sampled the value of the dynamic pressure and converted it to flow velocity. The test-section of this experiment is shown by a photograph in figure 4.5 and schematic representation of the complete test set-up is given in figure 4.6.

Figure 4.5: Photo of test region, with the glass fiber wall installed

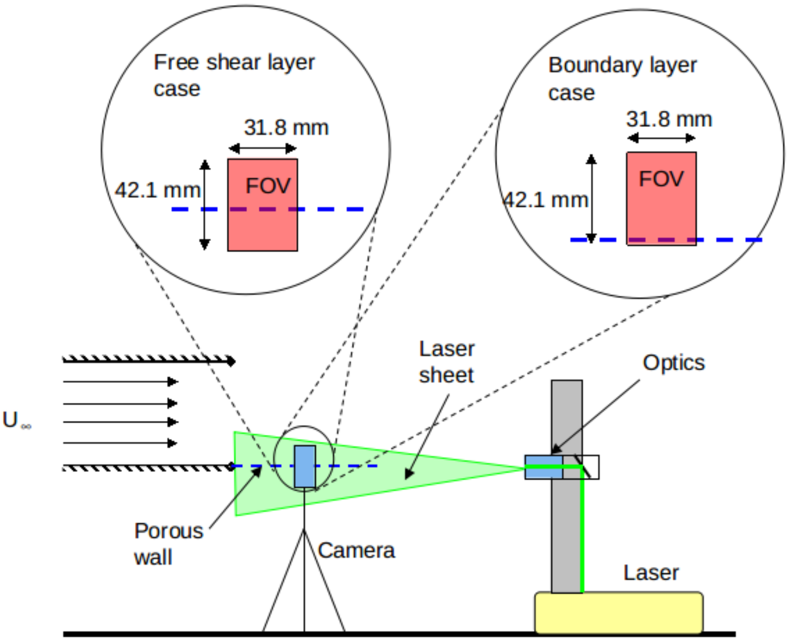

Figure 4.6: Schematic representation of experimental set-up

As can be seen in the schematic representation of the set-up, the laser was placed on the ground with a mirror positioned at the head to reflect the beam upwards. Another mirror combined with several lenses was used to form the light sheet parallel to the flow. The center of the light sheet was aligned with the bottom wall of the wind tunnel since the different porous materials would also be placed there. The laser used, was a Spectra-Physics Quanta-Ray which is a double pulsed Nd:YAG laser emitting visible green light at a wavelength of 532 nm. The images were acquired with a LaVision Imager Intense camera combined with a Nikon lens which had a focal length of 60 mm. Both the laser and camera were triggered by a LaVision programmable timing unit (PTU) which operated them at 10 Hz and was controlled through the DaVis software. Finally the seeding generator was placed at the inlet of the wind tunnel and was controlled manually, the mean particle size (d_p) was 1 μm. The technical details of the system are summarized in table 4.2.

Table 4.2: Technical specifications of PIV hardware and set-up

Parameter	**Quantity**
Camera sensor size	1376 x 1040 pixels
Pixel pitch	6.45 μm x 6.45 μm
Field of view	42.1 mm x 31.8 mm
Magnification factor, M	≈ 0.2
Lens to sensor distance	72.6 mm
Lens to laser sheet distance	346.2 mm
f#	8
Pulse delay, Δt	30, 45, 60 μs for U_∞ = 20, 15, 10 m/s respectively

With parameters listed above the resulting particle image diameter (d_τ) can be calculated with equation 4.4 and was found to be 12.46 μm. This is just under twice the pixel pitch and should allow for good imaging of the particles. The displacement of the particles (Δs) is estimated with equation 4.5. For an interrogation window of 64 by 64 pixels the resulting displacement of 120 μm corresponds with a displacement of 30 % of the interrogation window. This is slightly higher than the standard 25% displacement but the longer pulse delay was done intentionally because the velocities in the boundary layer are expected to be lower compared to the free stream velocity.

$$d_\tau = \sqrt{(Md_p)^2 + (2.44\lambda(1+M)f\#)^2} = 12.46\mu m \tag{4.4}$$

$$\Delta s = MU_\infty \Delta t = 120\mu m \tag{4.5}$$

The system was calibrated by means of a calibration plate with millimetre paper through the DaVis software. Next the Nikon lens was focused on the particles itself while running the laser and wind tunnel at low power. For each measurement 1000 image pairs were acquired to allow for statistical analysis of the flow.

The different porous materials were placed on a wooden frame which fitted into another wooden support structure that extended the bottom wall of the wind tunnel. All edges were covered with tape to make the wall and mounting as smooth as possible. Figure 4.5 shows a photo of the glass fibre fabric installed on the wooden frames, mounted at the bottom wall of the wind tunnel exit.

4.3.2 PIV data processing

For the post processing of the PIV data, again DaVis was used. The first step in processing the images was subtracting a background image. This was needed to reduce the reflections of the laser light. Especially with the light coloured glass fiber and Kevlar cloth reflections were an issue, spoiling the region closest to the wall. Next the sliding minimum was subtracted from the images. The actual cross-correlation was done with a multi-pass algorithm with an initial window size of 64 by 64 pixels and a final window size of 16 by 16 pixels with 50 % overlap. A pre-shift of 8 pixels was applied. The PIV processing parameters are summarized in table 4.3.

Table 4.3: Parameters for post-processing of PIV measurements

Parameter	**Quantity**
Initial window size	64 by 64 pixels
Final window size	16 by 16 pixels
Overlap	50 %
Pre-shift	8 pixels
Obtained spatial resolution element	0.25 mm
Number of double frames	1000

Once the instantaneous velocity vector fields were calculated, they are used to calculate both the mean and rms values of the velocity components u (streamwise) and v (normal to the stream). These statistical manipulations again resulted in vector fields which then were spatially averaged in streamwise direction over a small distance (approximately 0.5 cm) to obtain the desired velocity profiles. This final step combined with the plotting was done by a Python and Matlab script.

4.3.3 Test program for PIV measurements

The test program for the PIV measurements is given in table 4.4. As shown in the table the same free stream velocities are tested over four porous materials and a free shear layer. The laser pulse separation time is adjusted to the free stream velocity to obtain the same free stream pixel displacement for each measurement as calculated in section 4.3.1. These are the only to varying parameters, the other settings remain constant for all PIV measurements.

Table 4.4: Test matrix for PIV measurements

Configuration	U_∞ [m/s]
Glass fiber	10, 15, 20
Kevlar	10, 15, 20
Perforated steel	10, 15, 20
Solid wall	10, 15, 20
Free shear layer	10, 15, 20

4.4 Aero-acoustic experiments with ATW

After completing the aerodynamic and acoustic characterization separately, the final measurements series aims to characterize the complete system. Both a qualitative and quantitative performance assessment will be made of the different configurations. In this series of experiments a wind tunnel test section with wall-mounted speakers was used to evaluate the effect a flow has on the received signal. The test section was open on one side allowing a shear layer to develop or a porous material to be installed. The emitted signals were recorded with both a single calibrated microphone and a 64 element microphone array.

4.4.1 Experimental set-up and data acquisition

Since a low background noise was preferable for these aero-acoustic measurements, the vertical low turbulence tunnel at the TU Delft was used, hereafter called the V-tunnel. The open jet tunnel originally had a circular exit with a diameter of 0.6 m. This was not suited for the current campaign because a curved shear layer would complicate the post-processing of the microphone array measurements and would make installation of the porous materials very complicated. Therefore a nozzle was designed and constructed which transforms the exit to a 0.4 m by 0.4 m square exit. A description of the design, construction and validation of the nozzle can be found in appendix A. With the new nozzle the maximum velocity of the V-tunnel was increased to approximately 55 m/s. The flow speed was again measured by a pitot tube connected to a Mensor digital pressure gauge, model 2101. The complete set-up of the experiment, with letters indicating each major component, is depicted in figure 4.7(a). Each component of the set-up will be detailed below.

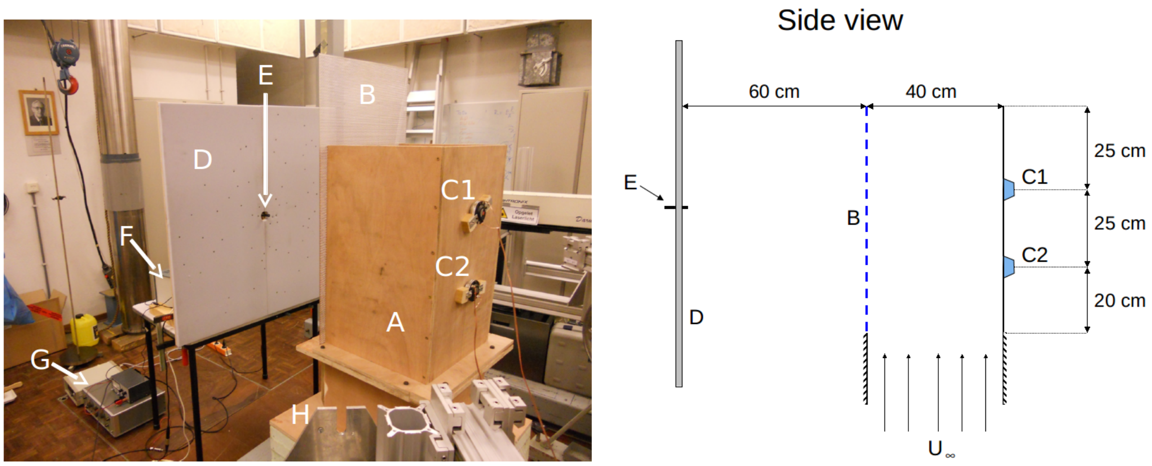

(a) Photograph of test set-up

(b) Side view of set-up

Figure 4.7: Representation of test set-up

Test-section

The test-section indicated by the letter ”A” in figure 4.7(a) is placed at the exit of the new nozzle (”H”) and is constructed from solid wood. It forms a box of 0.4 m by 0.4 m by 0.7 m from which one wall is removed such that a free shear layer can develop. Instead if a porous wall is installed a turbulent boundary layer develops. In figure 4.7(a) a perforated plate was installed indicated by the letter ”B”. In total three different configurations were tested. First reference measurements were performed with no porous material in place. Secondly a sheet of perforated aluminium, detailed in section 4.1 was attached to the test section. In addition stiffeners were added to the bottom and top of the plate to reduce vibrations. Thirdly, a glass-fiber cloth was tensioned over a wooden frame of 0.4 m by 0.7 m and attached to cover the open side of the test-section. Since during the previous aerodynamic measurements it was already difficult to tension Kevlar over a 0.4 m by 0.4 m frame it was decided not to use Kevlar for this campaign.

Opposite of the open face two 1 in BMS compression drivers type 4540ND were installed (”C1” and ”C2”), their placement can be seen in figure 4.7(b). Speaker ”C1” is mounted 45 cm downstream of the nozzle exit and speaker ”C2” is placed 20 cm downstream. They were powered through a regular audio amplifier. The signals were sent to one of the two speakers, the exact combinations are given in the test-matrix of this campaign which is provided in table 4.6. The different signals used to characterize the three configurations are listed below:

- Pure harmonic tones at 4 kHz, 8 kHz, 12 kHz and 16 kHz
- White noise
- Frequency sweep with $f_0 = 2$ kHz, $f_e = 20$ kHz and $t_e = 20$ s in equation 4.3

Measurement equipment

The microphone array represented by the letter ”D” in figure 4.7(a) consists out of 64 microphone elements connected to a custom data acquisition system (”F”). The microphones are fixed to a wooden support structure which is covered with sound absorbing foam. The microphone pattern, shown in figure 4.8, is a random configuration which was optimized to reduce side lobe levels in the beamforming algorithm. The custom data acquisition (DAQ) box samples all 64 channels simultaneously at a rate of 52083 Hz. Inside the same box the analog signals are sent through a high- and low-pass filter to prevent aliasing and an amplifier ensures the dynamic range of 16-bits is covered. The filters create an operating frequency range between 20 Hz and 25 kHz. The DAQ is connect to a PC which controls the measurements and receives the data over a standard Ethernet cable. Each measurement was taken over a period of 20 s.

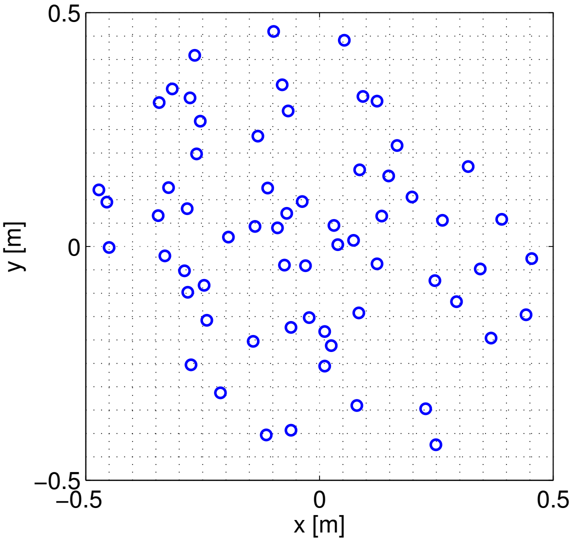

Figure 4.8: Microphone array pattern

The single microphone used to perform the calibrated measurements was a LinearX M51, indicated in figure 4.7(a) by the letter "E". The microphone was powered with 9 V direct current. The output signal of the element was amplified with a gain of 10 and also sent through a high- and low-pass filter. The cut-off frequencies for the single microphone were 20 Hz and 21.5 kHz. The power supply, amplifier and filters are represented by the letter "G". The microphone signal was sampled with a National Instruments cDAQ-9174 chassis at a rate of 40 kHz, again over a period of 20 s. The microphone was calibrated similar to the method explained in section 4.2.2. However this time a pistophone generating 114 dB at 250 Hz was used as calibrated source. The technical specifications of both the microphone systems are summarized in table 4.5.

Table 4.5: Technical specification of microphone systems

	Single microphone	**Microphone array**
Number of elements	1	64
Calibrated	Yes	No
Frequency range	20 Hz - 21.5 kHz	20 Hz - 25 kHz
Sample rate	40 kHz	52.1 kHz
Measurement time	20 s	20 s

4.4.2 Single microphone data processing

From the recorded time series of the single microphone the power spectral density (PSD) is calculated using the average periodogram method of Welch (1967). The algorithm uses segments of the complete signal to obtain an average estimation of the PSD. In this case the segments were selected to be 40000 samples long in order to obtain a frequency resolution of 1 Hz. With an overlap of 50 % this resulted in a PSD computed from 39 segments. To further process the data the background level for each configuration and flow speed is subtracted from the corresponding measurement. An example PSD after processing is depicted in figure 4.9, the vertical blue lines indicate the predicted position of the shoulder frequencies ($f_{shoulder}$, see equation 2.22) based on the theory presented by Sulaiman (2011). To easily compare the spectral broadening at different frequencies, the PSD of the tonal sound source measurements are repositioned around the emitted source frequency, such that $\Delta f = f - f_{source}$. This means that all peaks are centred around 0 Hz.

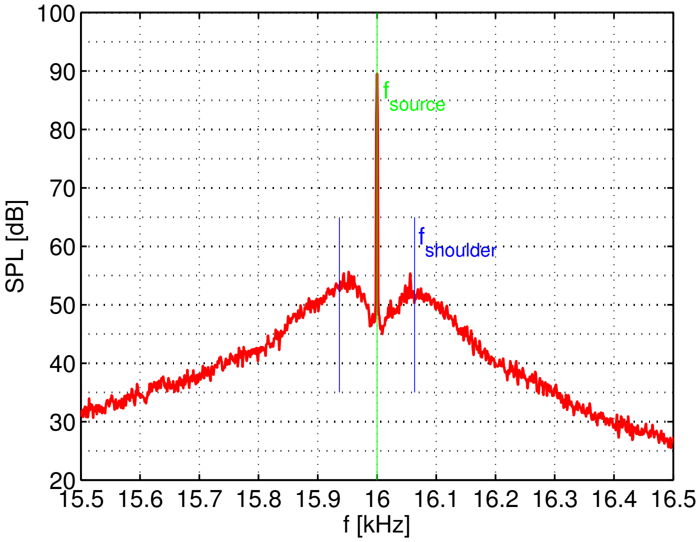

Figure 4.9: PSD of acoustic pressure acquired for case with tonal noise source located in open jet (frequency 16 kHz), $U_\infty = 30$ m/s. Additionally frequency of the shoulders is indicated based on prediction of equation 2.22.

4.4.3 Microphone array data processing

The data recorded by the microphone array system is processed with the conventional frequency domain beamformer as described in section 2.1.2. Although more advanced beamforming algorithms are known to have a better spatial resolution, this method is selected because it is the most general and robust. For all source plots the axes system is relative to the array with the origin at the center of the array. The y-direction is found in streamwise direction whilst the x-direction is defined normal to that. Finally the z coordinate represents the distance between the array and the scan plane, which is equal to 1 m for all cases. The field of view is selected as $-0.15 \leqslant x \leqslant 0.15$, $-0.25 \leqslant y \leqslant 0.25$ and $z = 1$. This FOV does not exceeds the limits of the test section and is based on the expected location of source "C1" at $y = 0.13\ m$ and "C2" at $y = -0.12\ m$. For some source maps only the upper or lower part of the field of view is used to focus on one of the two sources. The points in the FOV will be evaluated every 0.005 m, which is well below the expected resolution of the beamformer (see equation 2.5).

Since the microphone array system is still in development it has not been calibrated for sensitivity yet. Therefore, the response of the array is unknown and most likely not linear over all frequencies. Thus, each source plot will be scaled with a reference value and is placed on a logarithmic scale. Typically the maximum of the source plot is taken as reference and a range of 12 dB is used. An example of an unscaled and scaled source plot of a single source at 8 kHz is shown in figure 4.10. The scaled source map removes all the levels below 12 dB, thus cleaning the plot. Transferring the data onto a logarithmic scale makes sense for acoustic data since the human hearing system also works on a logarithmic scale. In figure 4.10 one can see that some of the background points become distinguishable with the logarithmic scale while they are uniform to the background in the raw beamforming output.

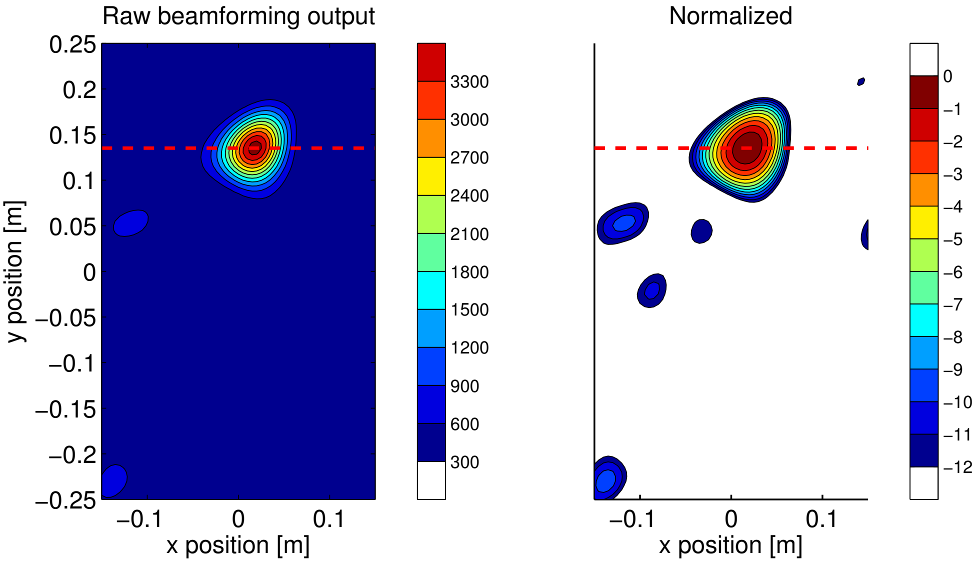

Figure 4.10: Example of source plot scaling on 8 kHz tonal source. Left data reported in sound power calculated by beamforming algorithm, right after normalizing with peak power and in dB.

The maximum flow speed used during these tests is 30 m/s, this results in a Mach number below 0.1. Therefore the correction for the refraction of acoustic waves over the shear layer can be done with the model presented by Sijtsma (2010). This is a fast but accurate way of correcting for the shift in source location. A more detailed description of this technique was already given in section 2.3.1. Figure 4.11 demonstrates how this technique corrects for the difference in acoustic path length when a flow is present. As before a single frequency sound of 8 kHz was emitted through source "C1", however this time the wind tunnel was running at 30 m/s. In the uncorrected source plot shown in figure 4.11 the source is detected above the expected location (indicated by the red dashed line). When the correction is applied the source is repositioned correctly.

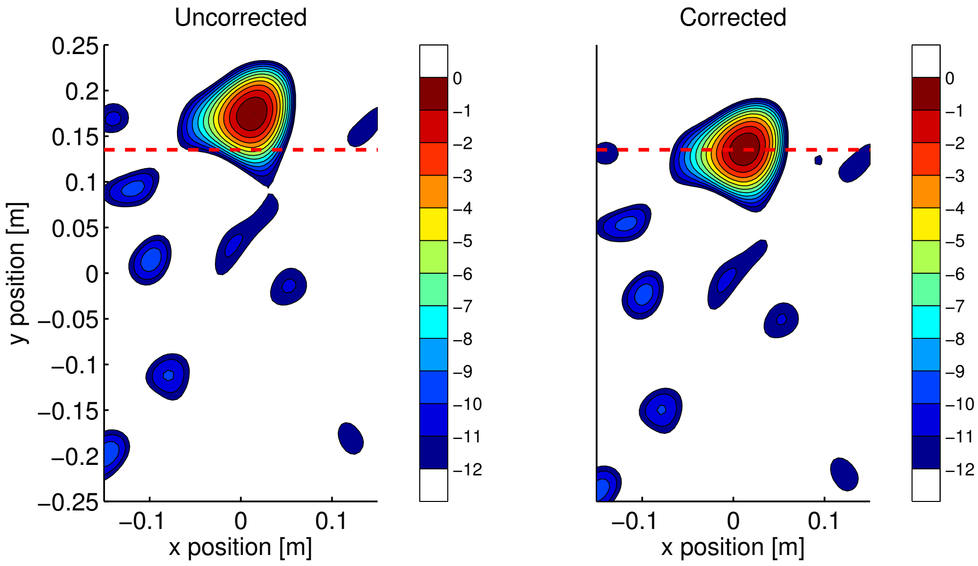

Figure 4.11: Source plots indicating the effect of shear layer correction on 8 kHz tonal source measurement with $U_\infty = 30\ m/s$, red dashed line indicating the expected source position.

4.4.4 Test program for microphone and array measurements

The test program for the single microphone and microphone array measurements is identical since the measurements were performed simultaneously. The test-matrix is summarized in table 4.6. As shown in the table the same experiments are repeated at a free stream velocity of 0, 20 and 30 m/s. For each velocity the same signals were emitted from the upper and lower source. The complete matrix was repeated for the three configurations mentioned before: no porous material/shear layer, perforated metal plate, tensioned glass fiber cloth.

Table 4.6: Test matrix for aero-acoustic measurements, position of sources C1 and C2 indicated in figure 4.7(b)

Flow speed [m/s]	Source	Signal
0	na	background
0	C1	tones at: 4 kHz, 8 kHz, 12 kHz, 16 kHz
0	C1	white noise
0	C1	frequency sweep
0	C2	tones at: 4 kHz, 8 kHz, 12 kHz, 16 kHz
0	C2	white noise
0	C2	frequency sweep
20	na	background
20	C1	tones at: 4 kHz, 8 kHz, 12 kHz, 16 kHz
20	C1	white noise
20	C1	frequency sweep
20	C2	tones at: 4 kHz, 8 kHz, 12 kHz, 16 kHz
20	C2	white noise
20	C2	frequency sweep
30	na	background
30	C1	tones at: 4 kHz, 8 kHz, 12 kHz, 16 kHz
30	C1	white noise
30	C1	frequency sweep
30	C2	tones at: 4 kHz, 8 kHz, 12 kHz, 16 kHz
30	C2	white noise
30	C2	frequency sweep

Chapter 5

Results and discussion

In the current chapter the results of the three different experimental campaigns described in chapter 4 will be discussed. If available the results will be compared with measurements performed by other people mentioned in chapter 2. First the results from the acoustic transmission measurements will be presented and discussed in section 5.1. Next the results from the PIV experiments on the different porous materials will be given in section 5.2. Finally the results from the aero-acoustic wind tunnel experiment are treated in section 5.3

5.1 Acoustic transmission results

In this section the results from the two measurement series outlined in section 4.2 will be presented. With these results the acoustic transmission properties of the different porous materials are evaluated. The ideal material would transmit all acoustic energy without any distortion.

5.1.1 Transmission coefficient measurements

Initially the transmission of sound waves through the different porous materials was analysed by testing a wide frequency range. A source signal with a frequency sweep from 1 Hz to 20 kHz was driving the speaker. The recorded microphone signals were then processed as discussed in section 4.2 to obtain the frequency spectrum for the different porous materials. Each spectrum corresponding to a different material was compared to spectrum obtained in the clean configuration (no material at interface). The difference of each materials spectrum with the clean spectrum was calculated to obtain the acoustic power transmission coefficient (T), according to equation 5.1. Figure 5.1 shows this ratio for all porous materials tested. As expected the clean configuration has 0 dB loss over the whole frequency range. Both fabric materials show good transmission properties with a maximum power difference of 1.7 dB for glass fiber and 2.5 dB for Kevlar. The perforated plates also show very good transmission characteristics up to 7500 Hz, at higher frequencies some interaction takes place leading to (periodic) fluctuations in the transmission coefficient as can be seen in figure 5.1. A closer look at the graph corresponding to the perforated steel plate reveals that there are 12 peaks between 10 kHz and 15 kHz. This means that the response pattern repeats itself every 417 Hz.

$$T = SPL_{clean} - SPL \; [dB] \tag{5.1}$$

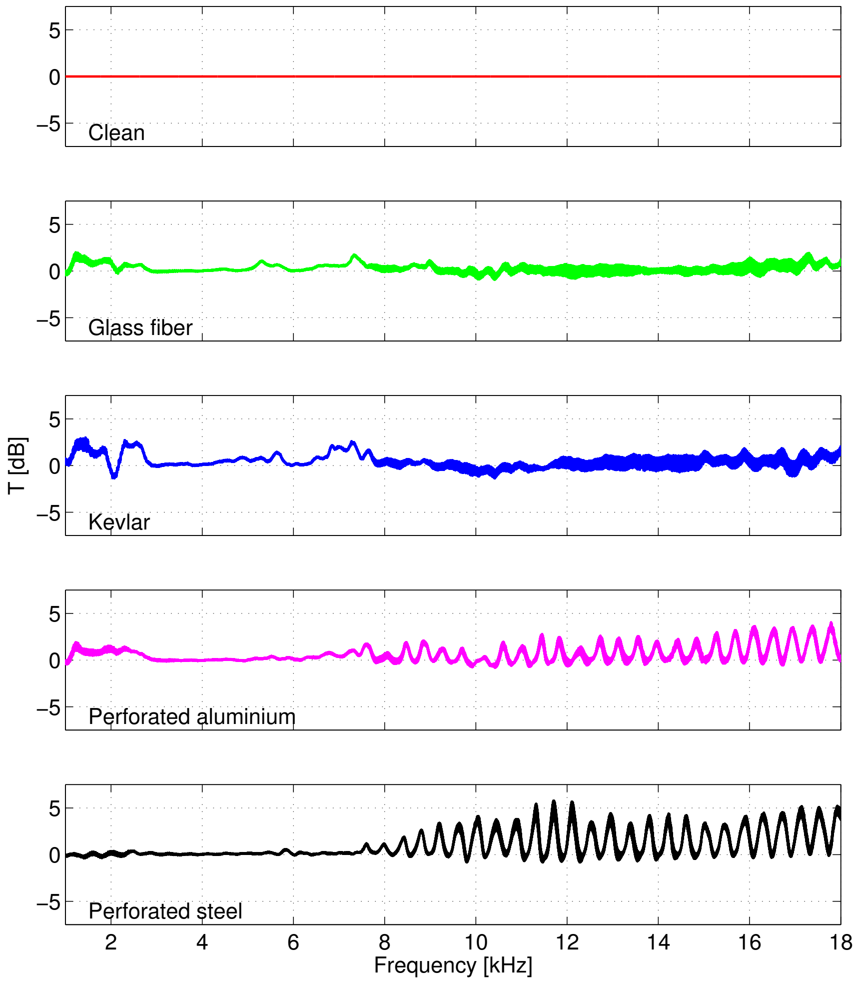

Figure 5.1: Acoustic power transmission coefficient as function of frequency for different porous materials.

It is important that the acoustically transparent material acts similar to the case when no material is used. Therefore the acoustic power measured behind the porous material should directly correspond to the power of the source. In this second acoustic transmission test the power difference between two recordings is considered. The first recording was made with a frequency sweep from 0 Hz to 6 kHz as source signal. The second recording on the other hand used the same signal but it was now produced with a 10 dB less power. The power difference between those two measurements is calculated by subtracting the lower amplitude PSD from the higher one as indicated by equation 5.2. Ideally this difference should be 10 dB over the whole frequency range. However in figure 5.2 it can be seen that even in the clean configuration some deviations from this 10 dB power difference occur. Furthermore it can be seen that all tested materials show a similar power reduction to the clean configuration.

$$\Delta SPL = SPL_{0dB} - SPL_{-10dB} \tag{5.2}$$

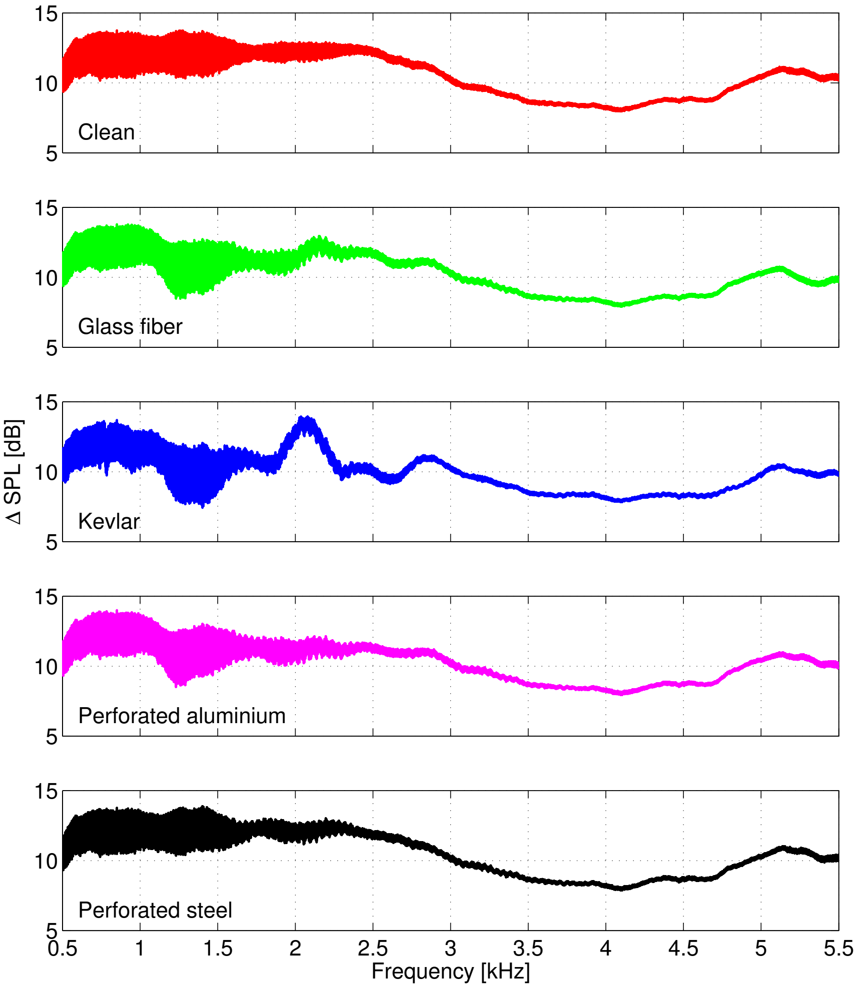

Figure 5.2: Difference in SPL measured for different porous materials with amplifier settings 0 dB and -10 dB.

5.1.2 Effect of microphone position

As described in section 4.2 a second series of acoustic transmission measurements was performed to further investigate the distortion pattern found at higher frequencies with the perforated plates. In this test only the perforated steel plate was used and the microphone was placed at different positions. The x coordinate is defined as the normal distance behind the perforated plate while the y coordinate is the lateral deviation from the center of the set-up as shown in figure 4.3(b).

The first analysis of the sound transmission properties at the different x-positions was done by using recorded frequency sweeps from 1 Hz to 20 kHz. The measured power spectra obtained at an axial position of 100, 180, 340 and 480 mm behind the perforated plate are depicted in figure 5.3. A few effects can be observed here. First of all it appears that the distortion gets greater with increasing distance between the porous plate and the microphone. At a distance of 100 mm almost no distortion is observed except for a sudden drop at 9 kHz, while at a distance of 480 mm an amplitude difference up to 3 dB in the pattern is measured. Another noticeable fact is that the distortion of the signal only becomes significant at frequencies higher than 6000 Hz. Finally it can be seen that two peaks in the power spectra are again approximately 417 Hz apart.

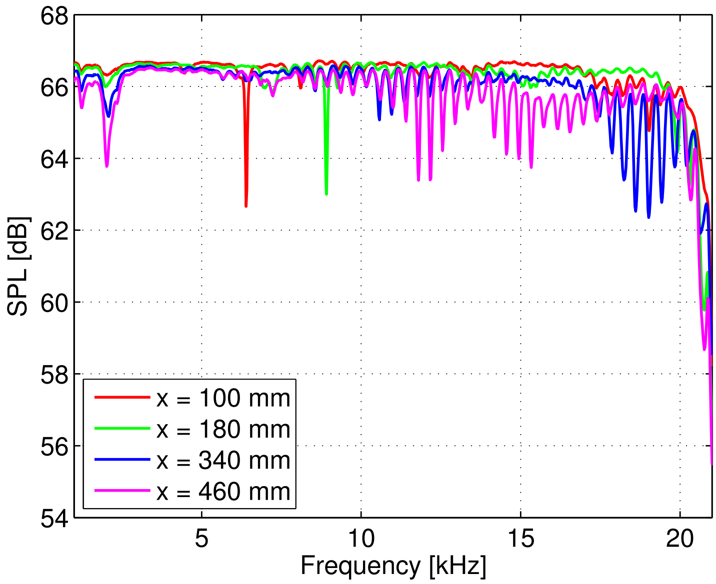

Figure 5.3: Acoustic pressure PSD measured through perforated steel plate, with frequency sweep emitted by loudspeaker at different distances x behind the porous interface.

To further investigate the separation of 417 Hz observed in the acoustic pressure PSD oscillations visible in figures 5.3, pure harmonic tones at different frequencies were transmitted through the perforated plate and recorded. The tones varied from 6 kHz to 7 kHz, in steps of 100 Hz allowing for reconstruction of the 417 Hz period. The x-position of the microphone was again changed from 20 to 500 mm with increments of 20 mm. The resulting acoustic pressure rms at a distance of 200, 300 and 400 mm behind the plate can be seen in figure 5.4. The pressure rms change caused by the perforated plate is noticeable for all positions, but similarly to the power spectra, the distortion gets more severe further behind the perforate plate. The separation of 417 Hz observed before is well captured with these measurements, over the span of 417 Hz, the acoustic pressure rms change goes trough one cycle.

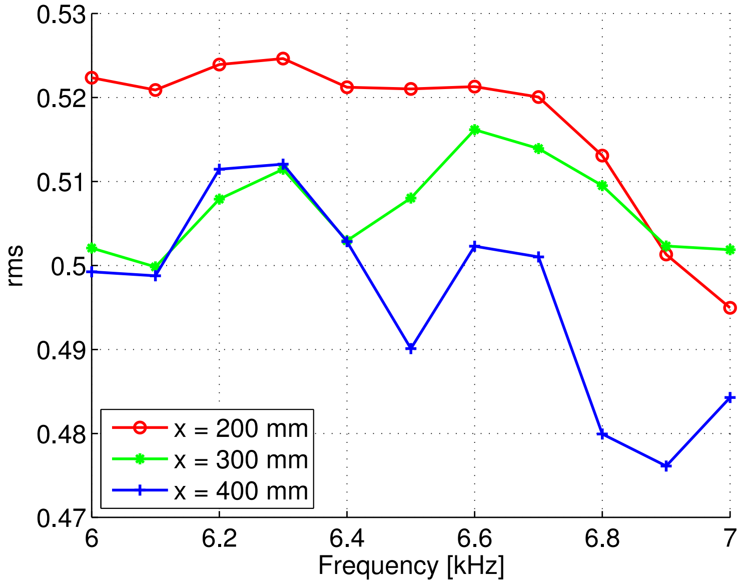

Figure 5.4: Acoustic pressure rms measured through perforated steel plate, with discrete frequencies emitted by loudspeaker at different distances x behind the porous interface.

In another set of measurements the x-position of the microphone was kept constant at 310 mm, and the y-position was varied from 0 to 300 mm with steps of 20 mm. Figure 5.5 shows the acoustic pressure rms at y positions of 80, 140, 200 mm for frequencies of 6000 to 7000 Hz. The pattern with a 417 Hz peak separation is again clearly visible. Similar to the trend observed for a changing x-position, the distortion increases with increasing distance from the centreline.

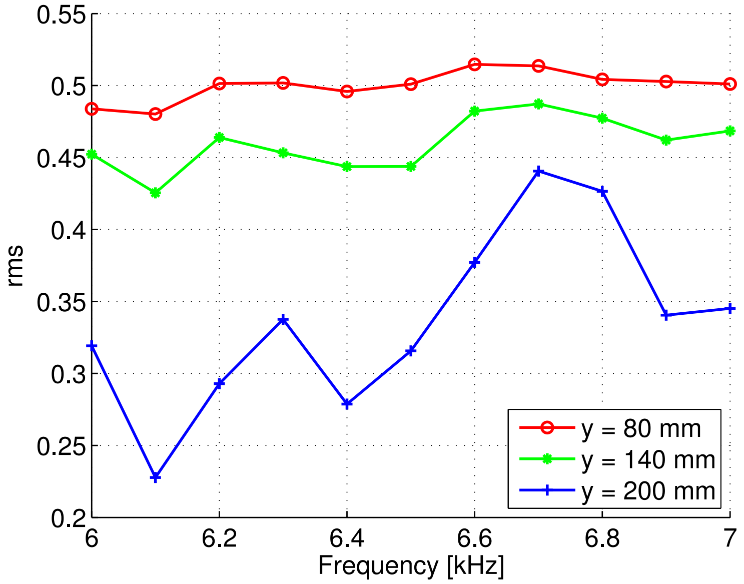

Figure 5.5: Acoustic pressure rms measured through perforated steel plate, with discrete frequencies emitted by loudspeaker at different lateral locations y.

5.1.3 Distortion pattern of perforated plates

A further analysis of the 417 Hz separation pattern reveals that the distortion is due to reflections. The path length associated with a period of 417 Hz is calculated with equation 5.3 and found to be 0.82 m. This corresponds to twice the distance between the loudspeaker and the perforated plate. Because the perforated plates have a smaller open area ratio compared to the fiber weaves, more acoustic energy gets reflected back towards the source. That wave then reflects once more on the hard casing of the speaker leading to the extra path length of twice the speaker to plate distance. The reflections can also be revealed when calculating the autocorrelation of the recorded microphone signal. Figure 5.6 shows the autocorrelation of a white noise measurement. The lag on the signal is expressed as extra path length by using $\Delta t \cdot c$. The first peak next to the zero-lag peak in the autocorrelation is located at $\Delta t \cdot c = 0.12$ m. This added path length could correspond with the distance between the microphone and the microphone tripod or an internal part in the speaker. The relfected sound waves from this first peak in the autocorrelation are found for all materials tested and also in the clean configuration. For the autocorrelation of the measurement done through the perforated plate, a peak is also visible at $\Delta t \cdot c = 0.82$ m, which again corresponds to twice the source to plate distance. Furthermore it can be seen in figure 5.6 that for both the clean and Kevlar configuration there is no second peak in the autocorrelation at $\Delta t \cdot c = 0.82$ m.

$$\Delta t \cdot c = \frac{c}{\Delta f} = \frac{340}{417} = 0.82m \tag{5.3}$$

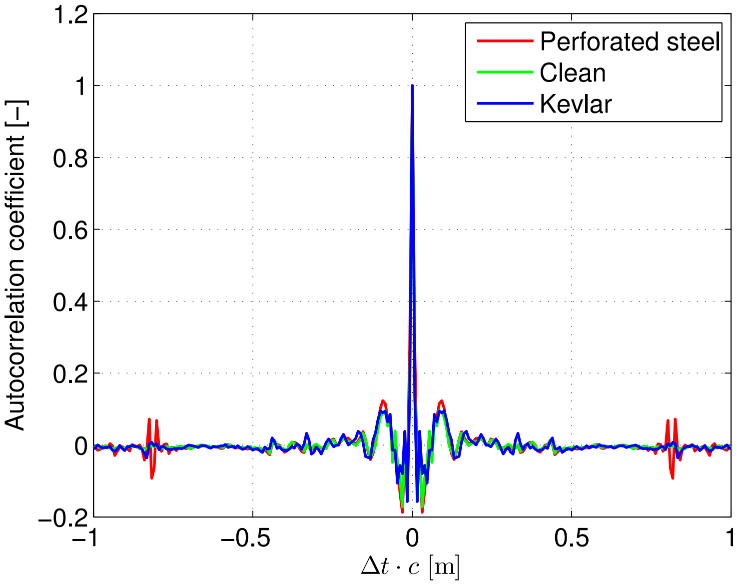

Figure 5.6: Autocorrelation coefficient of acoustic pressure measurement through different porous materials of white noise signal emitted by loudspeaker.

With this information the resonance frequencies origination from the reflections between the speaker and the perforated plate can be calculated using equation 5.4. Where d is the distance between the speaker and the perforated plate. These resonance frequencies correspond with the peaks visible in figure 5.1.

$$f_{resonance} = \frac{N \cdot c}{2 \cdot d} \qquad for \qquad N = 1, 2, 3, ... \tag{5.4}$$

5.2 Aerodynamics shear and boundary layer results

This section will present the results of the PIV measurements detailed in the test program given in section 4.3.3. A comparison with theoretical predictions and previous measurements from literature will be made. This section only contains the results for the mean streamwise velocity component and the normal velocity fluctuations since these are are directly related to the amount of spectral broadening caused by a turbulent region.

5.2.1 Mean streamwise velocity profiles

Figure 5.7 shows the mean streamwise velocity profile over a flat solid plate extracted from the PIV measurements compared with a theoretical approximation given by equation 2.10. The measured points (red dots) are in reasonable agreement with the theoretical approximation (blue line), except for the region close to the wall. At the wall the mean streamwise velocity should be zero, while the PIV results indicate a value of 60 % which is not physical. Since these results will only be used to determine the thickness of the turbulent bouldary layer ($\delta_{95\%}$), this does not impose a problem.

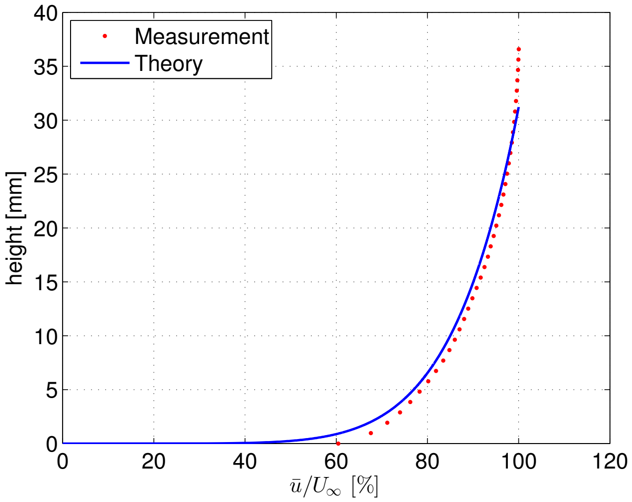

Figure 5.7: Mean streamwise velocity profiles $\bar{u}(y)/U_\infty$ determined from PIV measurements (red dots) and from theory, see equation 2.10 (blue line) for $U_\infty = 20$ m/s.

The mean streamwise velocity profiles over the porous surfaces are shown in figure 5.8 for different free stream velocities. It must be noted that the region close to the wall was not well captured by the PIV experiment and displays non-physical results, this region is indicated by a hatched patch. As mentioned in section 2.2.2, the outer part of the boundary layer should be independent of the wall conditions. For the measurements at free stream velocities of 10 and 20 m/s this is the case, since all profiles coincide in the outer layer. The measurements at 15 m/s does show some differences between the various walls, which could be due to variations in the test conditions.

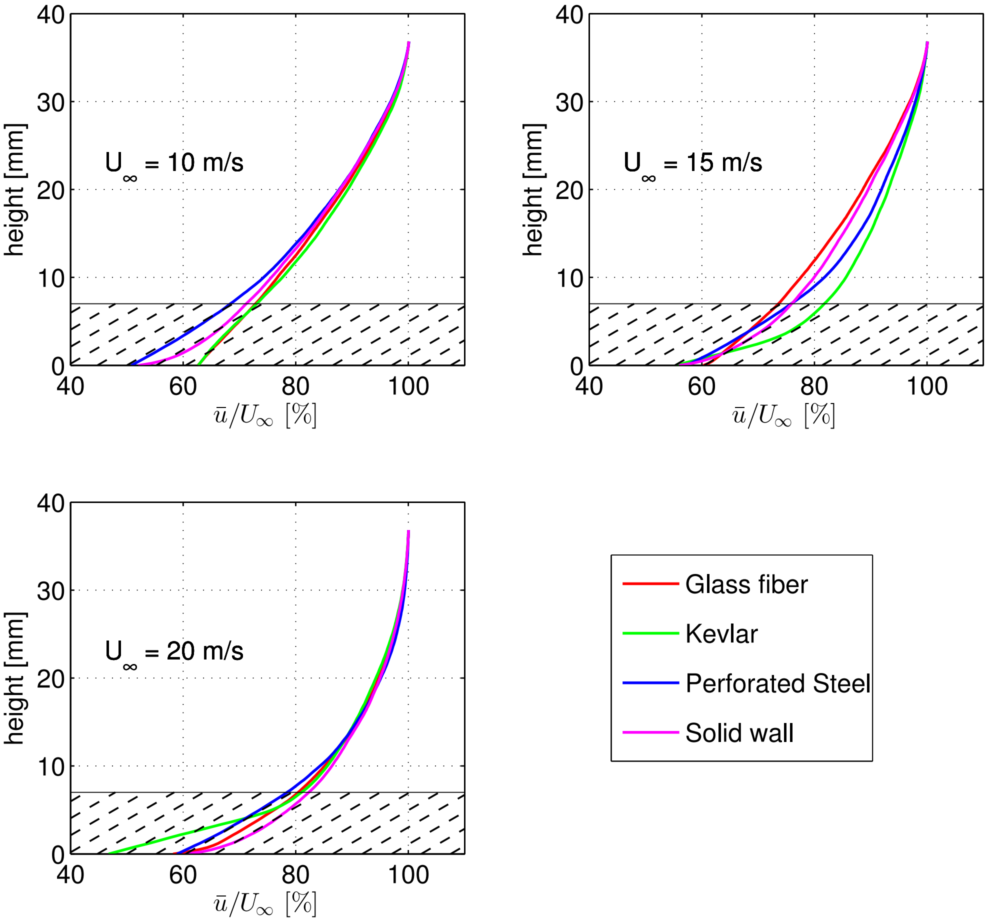

Figure 5.8: Mean streamwise velocity profiles $\bar{u}(y)/U_\infty$ determined from PIV measurements, hatched region indicates non-physical results.

Since a free shear layer is much thicker compared to a turbulent boundary layer and the same field of view was used for all PIV measurements, only the center region of the shear layer is captured. The mean velocity profile in this center region is depicted in figure 5.9 together with a theoretical estimation of the mean velocity profile. The centreline of the free shear layer is indicated by a black dash-dotted line and is located at $\overline{u}/U_\infty = 50\%$. The theoretical mean velocity profile was calculated the from the Gortler solution given by equation 2.8 with $\sigma = 13.5$ and $x = 0.5$ m. A close match is observed between the measured results and the theoretical approximation.

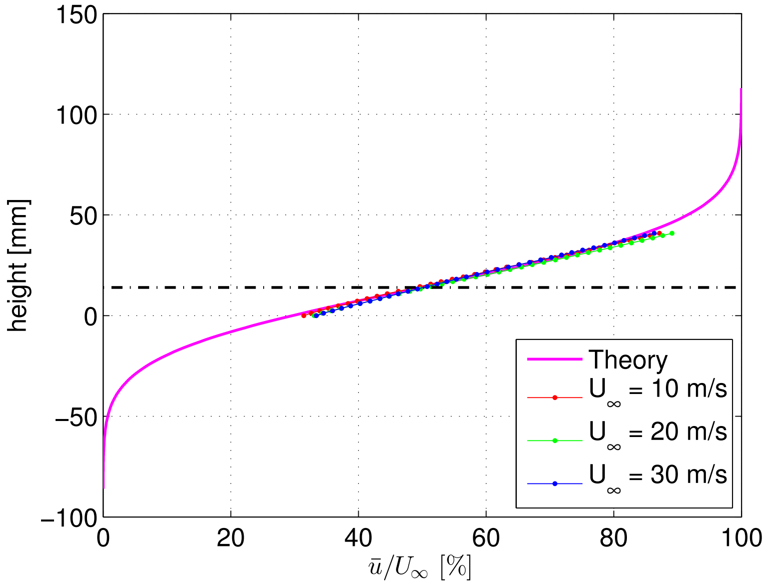

Figure 5.9: Mean streamwise velocity profiles $\bar{u}(y)/U_\infty$ determined from PIV measurements (dotted lines) and from theory, see equation 2.8 (pink line). Black dash-dotted line indicates free shear layer axis.

5.2.2 Wall normal velocity fluctuations

The processed PIV results for the rms profiles of the wall normal velocity fluctuations (v'_{rms}) are given in figures 5.10. The measured profiles have the same shape when compared to the profile for v'_{rms}/U_∞ given in figure 2.13 (line 3). The maximum value indicated in that graph for a smooth solid plate is just under 4 %. This very close the the value measured in this experimental campaign for the solid wall (cyan lines in figure 5.10). This is also the lowest value of $(v'_{rms}/U_\infty)_{max}$ measured. Closely followed by the glass fiber and Kevlar cloth with values of 4.2 % and 4.5 % respectively. The perforated steel plate shows a much higher level of wall normal fluctuations with a value of almost 8 % for $(v'_{rms}/U_\infty)_{max}$. This can be due to the increased roughness of the plate and because of the larger holes compared to the pores in the fiber weave materials. These larger holes will allow more flow to pass through the interface, which relaxes the wall compliance condition of $v = 0$ at the wall. Although the fiber weaves have higher open area ratio compared to the perforated plate, their pores are so small that viscous forces will resist the flow passing through the interface more compared to the large holes of the plate.

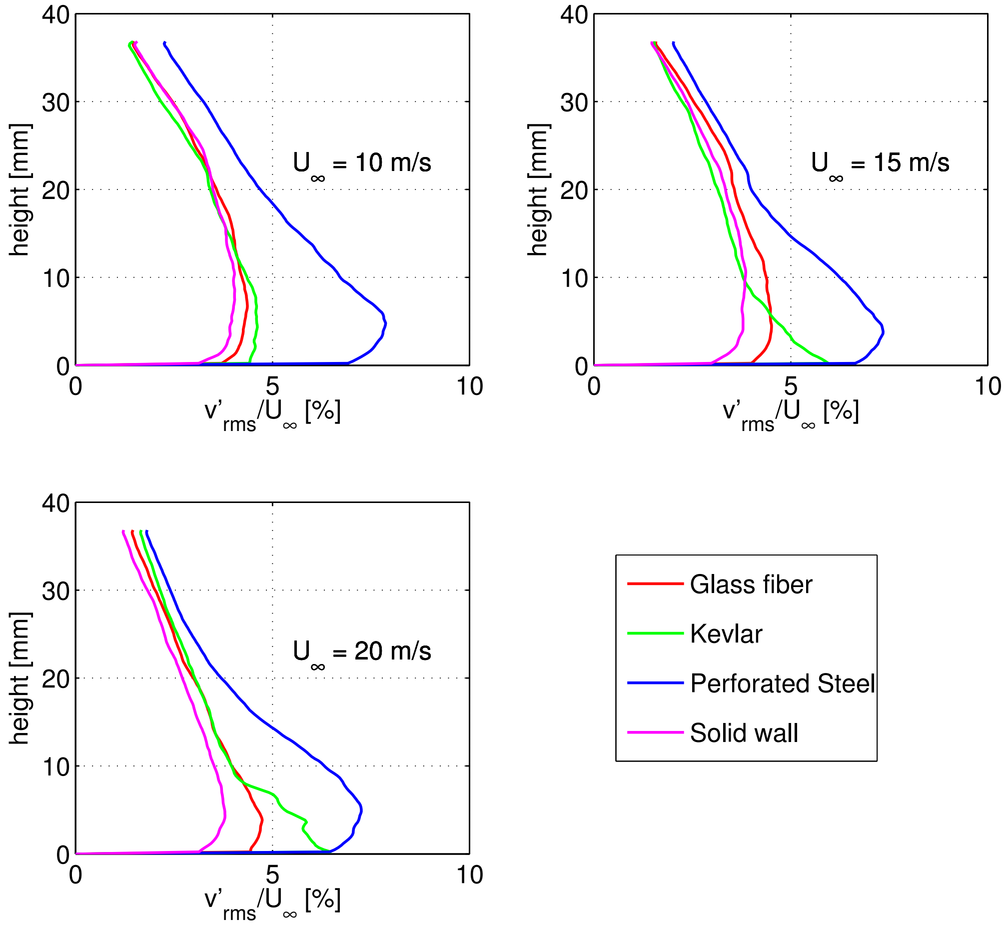

Figure 5.10: Rms profile of wall normal velocity fluctuations $v'_{rms}(y)/U_\infty$ determined from PIV measurements.

The results obtained at 15 m/s and 20 m/s free stream velocity (top-right and bottom-left in figure 5.10) are very similar to the results obtained at 10 m/s (top left), except for the Kevlar cloth. For the latter case, close to the surface the wall normal velocity variations seem to increase drastically. This might be due to the lower tension applied on the Kevlar compared to the glass fibre. Because Kevlar has a very high stiffness, it was difficult to apply the desired tensioning during manufacturing. This resulted in more movement of the cloth due to the airflow when compared to the glass fibre cloth.

The turbulent fluctuations inside a free shear layer are higher when compared to the boundary layer measurement presented before. The maximum value found for v'_{rms}/U_∞ from the shear layer measurements is between 10.5 % and 10.6 % for all free stream velocities, as can be seen in figure 5.11. The peak is expected at the center of the shear layer which is at y = 14 mm for this experiment. This is consistent with the location where $\overline{u}/U_\infty = 50\%$ in figure 5.9. The measured values for $(v'_{rms}/U_\infty)_{max}$ are also similar to the results of a series of hot wire measurement performed by Krober et al. (2013) and shown in figure 2.11(b).

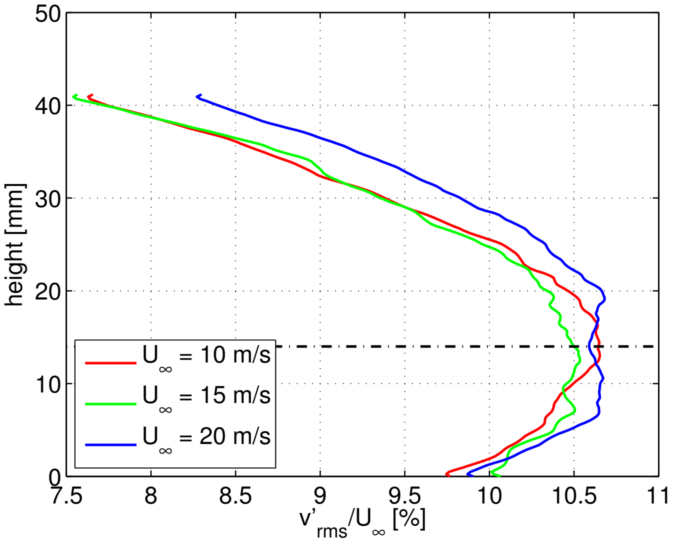

Figure 5.11: Rms profile of wall normal velocity fluctuations $v'_{rms}(y)/U_\infty$ determined from PIV measurements. Black dash-dotted line indicates free shear layer axis.

5.2.3 Effect of aerodynamic parameters on acoustic distortion

From the theory presented by Sulaiman (2011) which was summarized in section 2.3.2 the approximate amplitude of the time delay variations on an acoustic wave caused by a turbulent region can be estimated. As stated before this amplitude is dependent on the velocity fluctuations in the direction of the propagating sound wave, which is v' in a typical open-jet configuration and the thickness of the turbulent region (δ). Both these quantities were extracted from the PIV measurements to estimate the amplitude of the time delay variations.

For the shear layer measurements the thickness of the layer ($\delta_{95\%}$) is determined by making a fit of the theoretical expression given by equation 2.8 as indicated in figure 5.9. For the boundary layer measurements, the thickness ($\delta_{95\%}$) is directly extracted from the profiles shown in figure 5.8, by looking at the point where $\overline{u}/U_\infty = 95\%$. The obtained values are given in table 5.1. The boundary layer thickness measured at $U_\infty = 15$ m/s, is higher than expected. The difference with the measurements at 10 m/s should be greater. As mentioned before this could be due to variable test conditions. According to Sulaiman (2011) the maximum value for v' can be estimated based on the maximum rms value. The maximum value for v'_{rms}/U_∞ extracted from the velocity profiles shown by figures 5.10 and 5.11 are also given in table 5.1.

With these two parameters the amplitude of the time delay variations is estimated with equation 5.5 (Sulaiman, 2011), and are given in table 5.1. In the final column of that table the amplitudes are expressed as a percentage of the amplitude measured with a free shear layer to give an indication of the reduction in amplitude caused by using a porous wall.

$$a \approx \frac{\delta \cdot v'_{rms,max}}{c_0^2} \tag{5.5}$$

Table 5.1 shows that a porous wall can greatly reduce the amplitude of the time delay variations caused by turbulence. From these estimations it can be seen that a glass fiber wall can reduce the maximum amplitude by 94 %. Even the perforated metal plate reduces the amplitude by 90 %. The boundary layer over the perforated plate might have the highest levels of wall normal velocity fluctuations of all porous materials, the fact that it is much thinner compared to a free shear layer, results in a significant reduction of the amplitude of the time delay variations. Combined with the ease of construction, makes the perforated steel plate still a viable option for constructing an ATW.

Table 5.1: Estimation of maximum time delay variations on an acoustic wave with equation 5.5, based on PIV measurements.

	U_∞ [m/s]	$\delta_{95\%}$ [mm]	$(v'_{rms}/U_\infty)_{max}$ [-]	a [μs]	a/a_{sl} [%]
Shear layer	10	190	0.107	1.75	100
	15	190	0.105	2.60	100
	20	190	0.107	3.51	100
Solid wall	10	27.7	0.040	0.097	5.5
	15	27.2	0.039	0.136	5.2
	20	20.2	0.038	0.133	3.8
Glass fiber	10	27.2	0.044	0.103	5.9
	15	27.4	0.045	0.161	6.2
	20	20.46	0.047	0.168	4.8
Kevlar fiber	10	26.7	0.046	0.107	6.1
	15	23.3	0.059	0.180	6.9
	20	21.2	0.065	0.237	6.8
Perforated steel	10	27.7	0.079	0.189	10.8
	15	24.8	0.073	0.236	9.1
	20	19.9	0.073	0.251	7.1

The analysis carried out above estimates the maximum time delay on an acoustic wave. In order to get a more general idea of the amount of distortion, the amplitude can be approximated with an integral expression given in equation 5.6. Since the field of view of the PIV experiment was not large enough to capture the whole region in which v fluctuates, the experimental data first needs extrapolation before the integration can be done. For the boundary layer measurement the top part of the normal velocity fluctuations profiles have a linear trend. This linear part was simply extend until $v'_{rms} = 0$ as can be seen in figure 5.12. Because only the very center part of the shear layer was captured a more advanced curve fit is required. A Gaussian curve is fitted on the data measured for v'_{rms} as depicted in figure 5.13. In all these extrapolated plots the solid line represents the added part while the square symbols represent the experimental data. The results from integrating these profiles along y and dividing by the speed of sound squared to estimate the amplitude of the time delay variations are given in table 5.2.

$$a \approx \int \frac{v'_{rms}}{c_0^2} \cdot dy \tag{5.6}$$

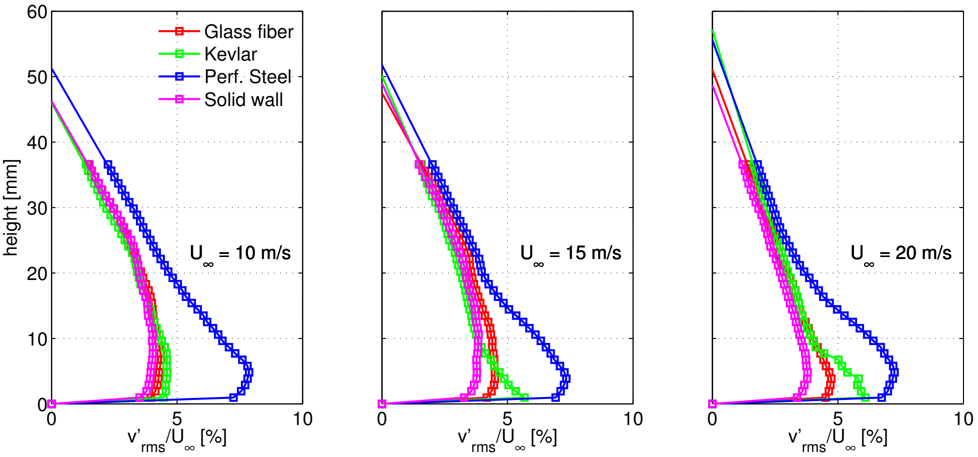

Figure 5.12: Rms profile of wall normal velocity fluctuations $v'_{rms}(y)/U_\infty$ determined from PIV (square symbols) and extrapolation to free stream conditions (solid line).

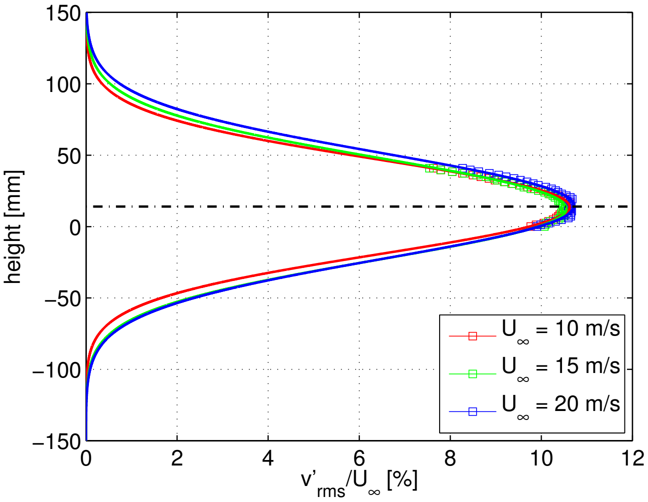

Figure 5.13: Rms profile of wall normal velocity fluctuations $v'_{rms}(y)/U_\infty$ determined from PIV (square symbols) and extrapolation to free stream conditions (solid line). Black dash-dotted line indicates free shear layer axis.

The integral results in table 5.2 show the same trends as the results for the maximum time delay variations given in table 5.1. Again the glass fiber cloth seems to perform best of all the porous materials. However even the perforated plate shows a great reduction in amplitude when compared to a free shear layer. Later on these results will be compared to the actual amplitude of the time delay variations measured during the aero-acoustic wind tunnel experiments.

Table 5.2: Estimation of average time delay variations on an acoustic wave with equation 5.6, based on PIV measurements.

	U_∞ [m/s]	a [μs]	a/a_{sl} [%]
Shear layer	10	0.762	100
	15	1.23	100
	20	1.72	100
Solid wall	10	0.112	14.7
	15	0.161	13.1
	20	0.187	10.8
Glass fiber	10	0.116	15.2
	15	0.182	14.8
	20	0.219	12.7
Kevlar fiber	10	0.114	15.0
	15	0.171	13.9
	20	0.247	14.4
Perforated steel	10	0.179	23.6
	15	0.243	19.8
	20	0.313	18.2

5.3 Aero-acoustic measurements through ATW

In this section a selection of the results obtained during the aero-acoustic measurements performed in the V-tunnel will be presented. Firstly, the single microphone data will be treated after which the microphone array results are given. These sections are followed by a more in depth analysis of both series of results. Because presenting all results would be very repetitive and not contribute much to the discussion, two sample cases were selected. For the first case moderate spectral broadening was expected while for the second case increased spectral broadening is expected. For the first case a tonal sound of 12 kHz was emitted through source "C1" with a flow speed of 20 m/s. For the second case the frequency is increased to 16 kHz and the flow speed is increased as well to 30 m/s, which should lead to more spectral broadening. These two cases will be used to demonstrate the effect the different porous materials have on both the single microphone and microphone array measurements. Additionally other data will be discussed to relate back to previous measurements.

5.3.1 Single microphone

Figures 5.14(a) and 5.14(b) show the power spectral density measured through the free shear layer. In figure 5.14(a) it is shown how the spectral broadening changes with flow speed and figure 5.14(b) shows the relation between spectral broadening and source frequency. In both cases more energy is transferred from the peak towards the shoulders with increasing flow speed or frequency which corresponds to the expectations from theory and previous measurements done by Sulaiman (2011) and Krober et al. (2013) presented in section 2.3.2.

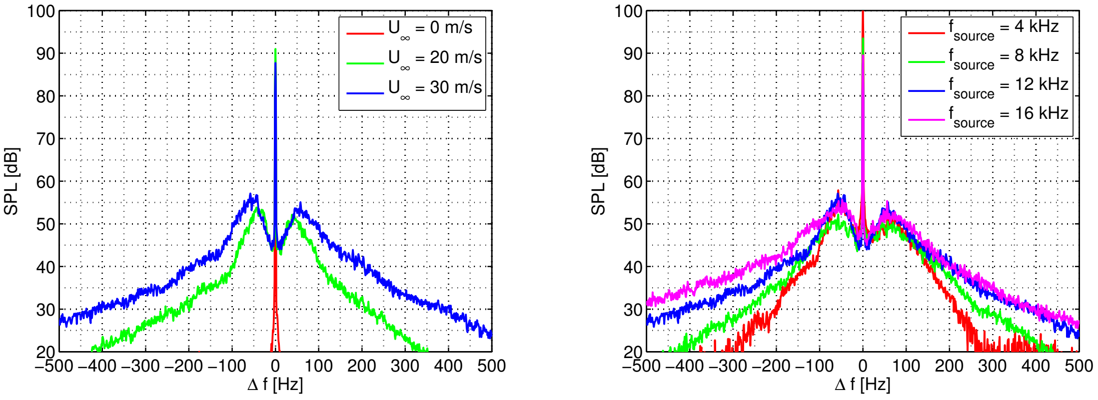

(a) For $f_{source} = 12$ kHz and varying free stream velocity.

(b) For $U_\infty = 30$ m/s and varying source frequency.

Figure 5.14: PSD of acoustic pressure acquired through free shear layer for case with tonal noise source located in open jet. Microphone at reference position (x=y=0), see figure 4.7(b).

The effect of installing an acoustically transparent wall is already visible in the 12 kHz case depicted in figure 5.15(a) and is even more pronounced in the 16 kHz case shown in figure 5.15(b). Both the perforated metal plate and tensioned glass fiber wall confine almost all acoustical energy within the peak while in the presence of a free shear layer the familiar shape of spectral broadening appears. The results obtained from measurements with lower source frequencies (see appendix B) also indicate a reduction in spectral broadening, but the difference between the free shear layer and the ATW's is reduced. A more detailed and quantified analysis of these results will be presented in section 5.3.3.

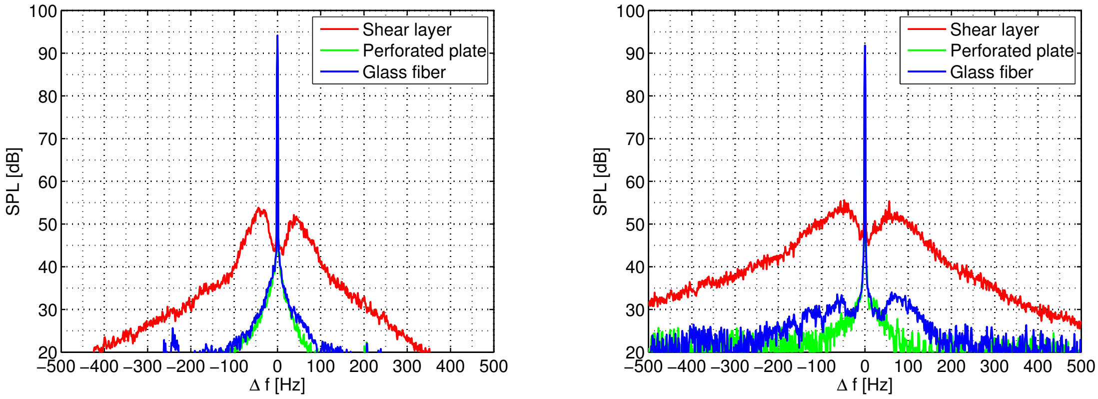

(a) $f_{source} = 12$ kHz and $U_\infty = 20$ m/s (b) $f_{source} = 16$ kHz and $U_\infty = 30$ m/s

Figure 5.15: PSD of acoustic pressure acquired through different porous materials for case with tonal noise source located in open jet. Microphone at reference position (x=y=0), see figure 4.7(b).

For each configuration a measurement of the background noise with the wind tunnel running was performed. The outcome of those measurements is shown in figures 5.16(a) and 5.16(b) for 20 and 30 m/s free stream velocity respectively. At 20 m/s the difference between the glass fiber wall and the shear layer is minimal, however the perforated plate has an elevated background noise level between 2 kHz and 10 kHz. When the flow speed is increased to 30 m/s also the glass fiber wall generates more background noise compared to the shear layer. Especially at higher frequencies (7 kHz and above) the difference is noticeable. The perforated metal plate now has an increased background noise level over almost the whole spectrum.

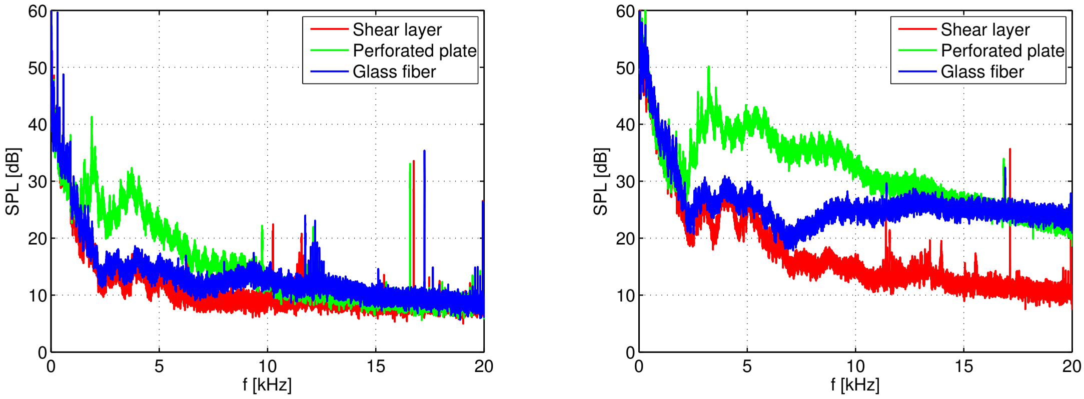

(a) $U_\infty = 20$ m/s

(b) $U_\infty = 30$ m/s

Figure 5.16: PSD of acoustic pressure acquired through different porous materials for wind tunnel background noise. Microphone at reference position (x=y=0), see figure 4.7(b).

5.3.2 Microphone array

To demonstrate the effect of spectral broadening on a microphone array, the case with a source emitting a tonal sound at 16 kHz and a free stream velocity of 30 m/s will be used. Figure 5.17 shows the source map obtained from data measured through a free shear layer. The portion of frequency spectrum used to obtain the the source map is indicated by a red line on the acoustic pressure PSD next to the source map. The acoustic pressure PSD is calculated from a single microphone element of the array close to the origin. For the initial analysis a wide frequency band (400 Hz) around the source frequency is used to calculate the source map. The dB scale of the source maps themselves are relative to the maximum power measured. Note that in these figures the flow goes from the bottom to the top. The red dashed line indicates the expected source location. One can see that through the free shear layer a source is detected above and below the expected source location. This shows that the interaction between sound waves and turbulent structures not only leads to spectral broadening for single microphone measurements, but also leads to spatial broadening when considering microphone array measurements.

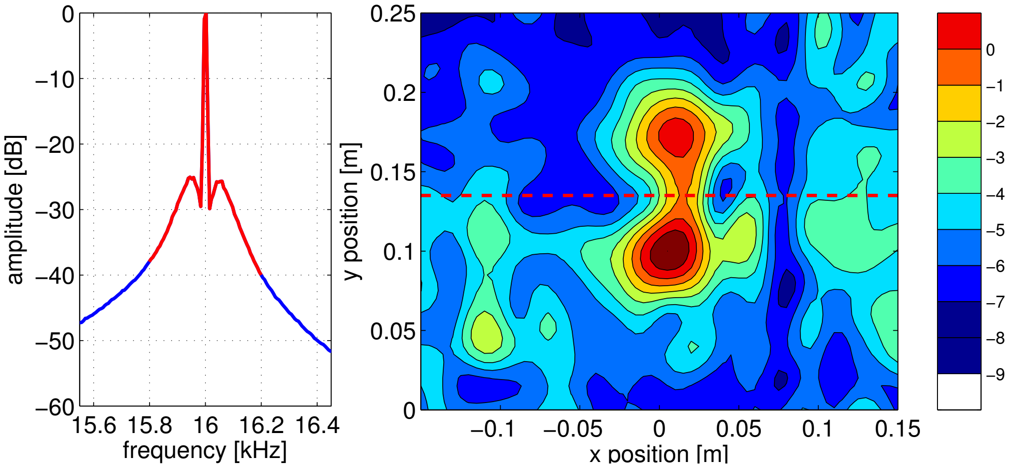

Figure 5.17: Left: PSD of acoustic pressure from single microphone; Right: source map calculated from microphone array data acquired through free shear layer. Red line on the PSD indicates frequency band used by the beamforming algorithm, red dashed line on the source map indicates expected source location. $U_\infty = 30$ m/s, $f_{source} = 16$ kHz.

Performing the same analysis on the data acquired through the perforated plate and the glass fiber wall results in figures 5.18 and 5.19 respectively. In both these cases the source is detected at the correct location and there are no signs spatial broadening. Similar to the single microphone results discussed in the previous section, the acoustic pressure PSD's show that more energy is confined in the peak.

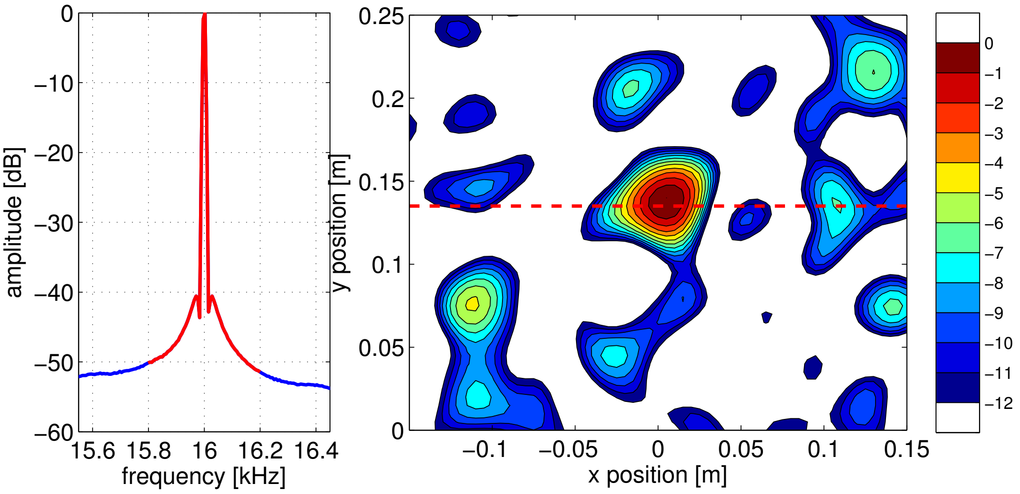

Figure 5.18: Left: PSD of acoustic pressure from single microphone; Right: source map calculated from microphone array data acquired through perforated metal plate. Red line on the PSD indicates frequency band used by the beamforming algorithm, red dashed line on the source map indicates expected source location. $U_\infty = 30$ m/s, $f_{source} = 16$ kHz.

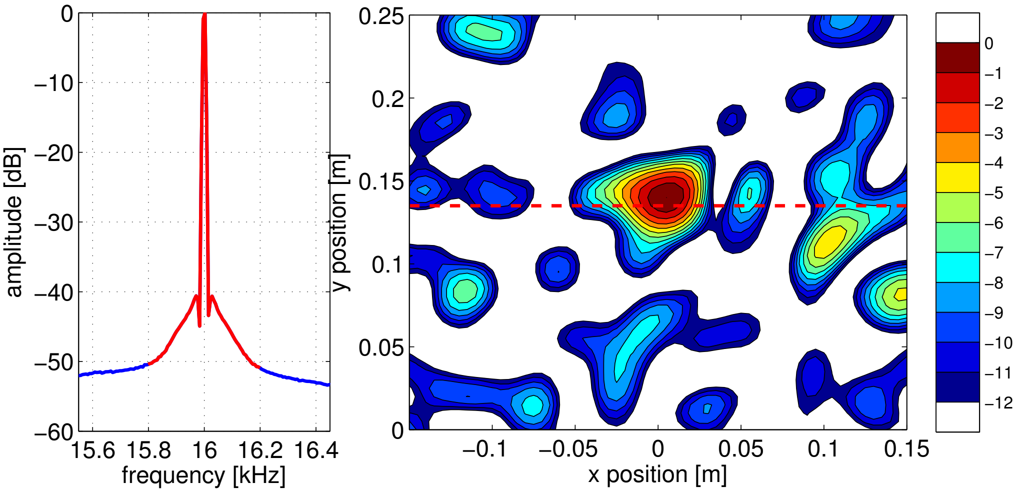

Figure 5.19: Left: PSD of acoustic pressure from single microphone; Right: source map calculated from microphone array data acquired through tensioned glass fiber wall. Red line on the PSD indicates frequency band used by the beamforming algorithm, red dashed line on the source map indicates expected source location. $U_\infty = 30$ m/s, $f_{source} = 16$ kHz.

To further investigate the spatial broadening observed through the free shear layer with the acoustic array, the broadened frequencies are processed separately with the beamforming algorithm. Note that this can be done for this characterization measurements since a known source is used but this is usually not the case for real measurements. Figure 5.20 shows the source maps obtained from measurements through the free shear layer for the main peak, left shoulder and right shoulder in the frequency spectrum. Analysing the source maps of the shoulder frequencies, a spurious source is detected above or below the actual source position. For this 16 kHz case measurements the power of these spurious sources calculated by the beamforming algorithm is higher than the actual peak itself. The spurious source related to the left shoulder is detected above the actual source position and has a 3 dB higher power than the peak. On the other hand the source related to the right shoulder is positioned below the actual source position and has a power level 5 dB above the peaks power level. Because these spurious sources have a higher power compared to the actual source, only the spurious sources are detected when analysing a wide frequency band as in figure 5.17. The same spurious sources appear when processing the data for the 12 kHz case, but then the power of the spurious sources is about 6 dB below the peak power. The source maps for the 12 kHz case can be found in appendix C.

Examining the same data for both acoustically transparent walls indicates a strong reduction of these spurious sources. Figure 5.21 depicts the source maps obtained through the perforated metal plate. Beamforming the left shoulder again results in a spurious source, however in this case the power of the source is around 30 dB lower compared to the main peak found in the top graph of figure 5.21. The source map of the right shoulder does not show a clear source but once more all the levels are 30 dB below the main peak power. Therefore when a wide frequency band is analysed of a measurement through the perforated plate, the actual source is detected as shown in figure 5.18. The results obtained through the tensioned glass fiber wall, given in figure 5.22 are very similar. Both the left and right shoulder result in a spurious source for this ATW but as for the perforated plate the levels are approximately 30 dB lower when compared to the main peak. This corresponds well to the results obtained for the 12 kHz case which are given in appendix C. Because the intensity of spectral broadening is less in the 12 kHz case, the levels of the spurious sources are 35 to 40 dB below their corresponding main peak.

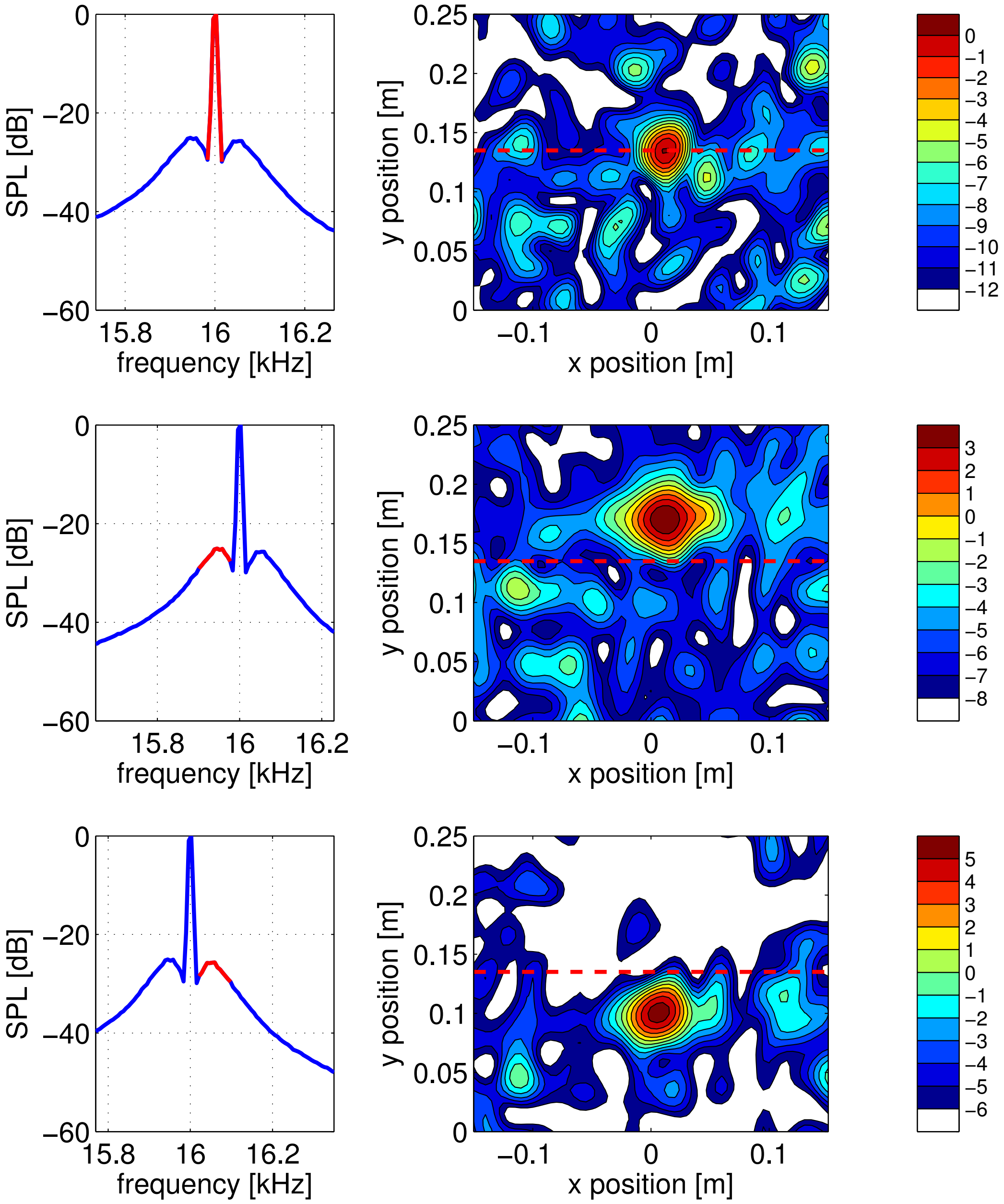

Figure 5.20: Left: PSD of acoustic pressure from single microphone; Right: source map of main peak (top) and shoulders (middle, bottom) calculated from microphone array data acquired through free shear layer. Red line on the PSD indicates frequency band used by the beamforming algorithm, red dashed line on the source map indicates expected source location. $U_\infty = 30$ m/s, $f_{source} = 16$ kHz.

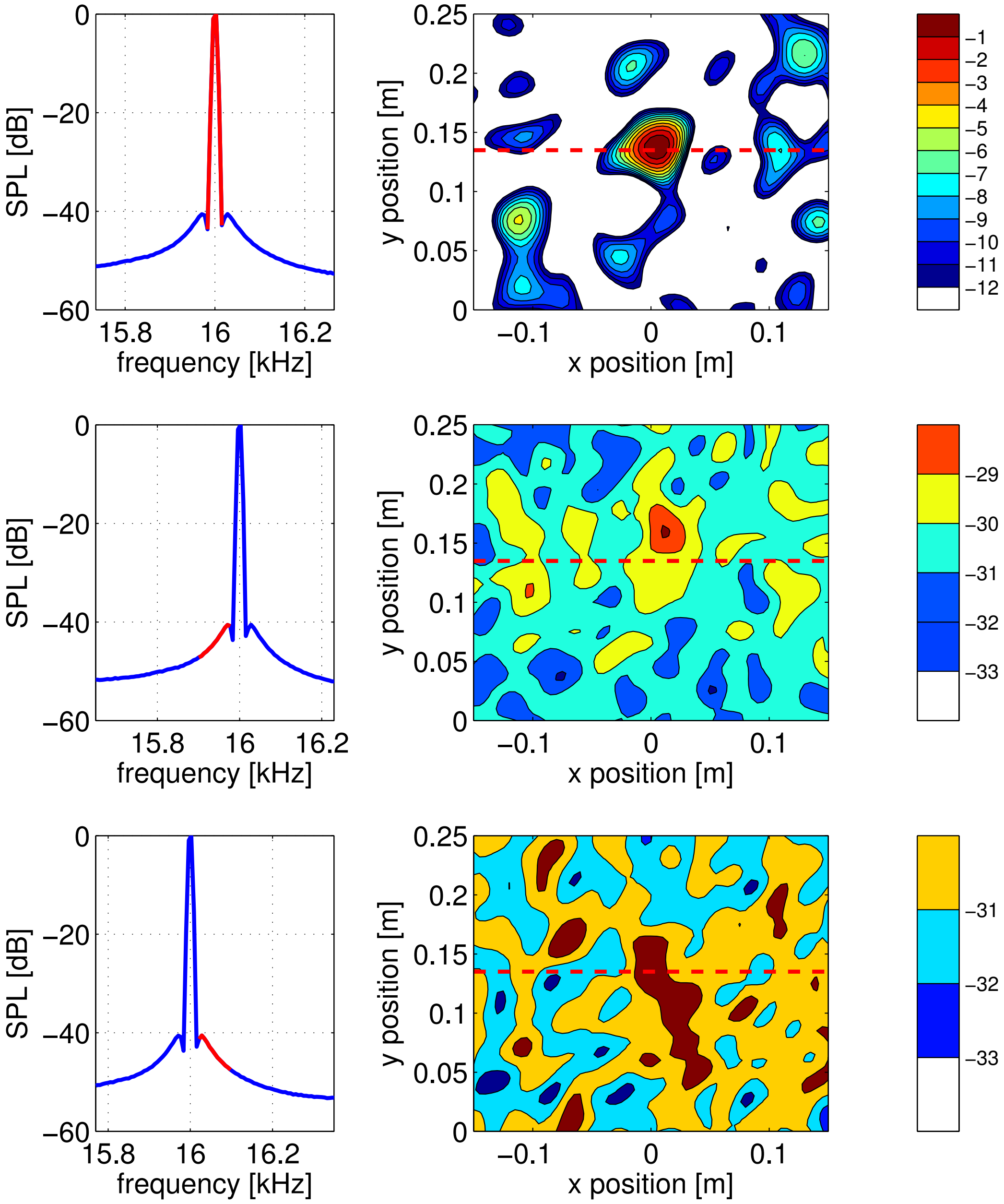

Figure 5.21: Left: PSD of acoustic pressure from single microphone; Right: source map of main peak (top) and shoulders (middle, bottom) calculated from microphone array data acquired through perforated metal plate. Red line on the PSD indicates frequency band used by the beamforming algorithm, red dashed line on the source map indicates expected source location. $U_\infty = 30$ m/s, $f_{source} = 16$ kHz.

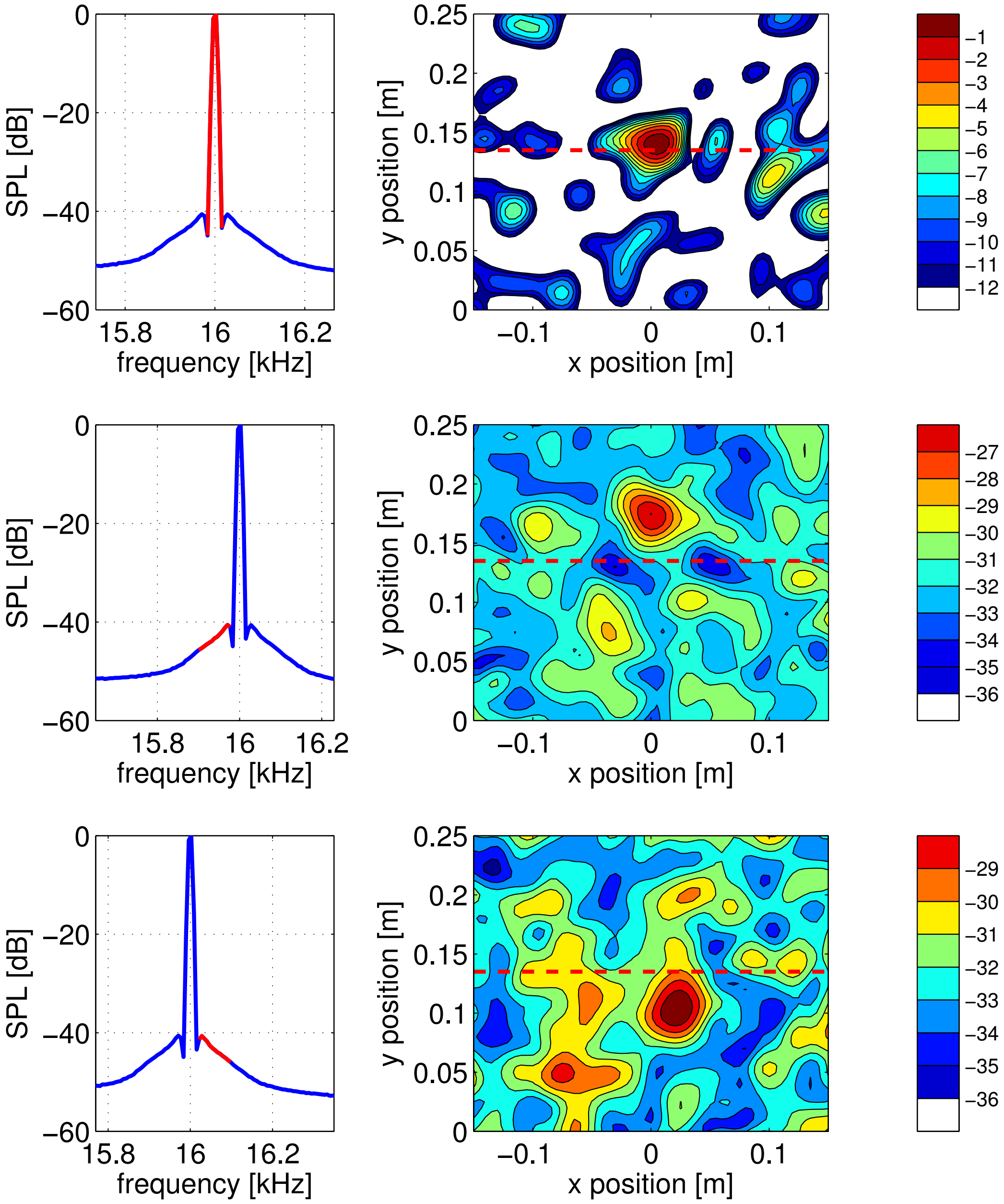

Figure 5.22: Left: PSD of acoustic pressure from single microphone; Right: source map of main peak (top) and shoulders (middle, bottom) calculated from microphone array data acquired through tensioned glass fiber wall. Red line on the PSD indicates frequency band used by the beamforming algorithm, red dashed line on the source map indicates expected source location. $U_\infty = 30$ m/s, $f_{source} = 16$ kHz.

5.3.3 Quantification of spectral broadening

The PSD's presented in section 5.3.1 already showed the spectral broadening that occurs when a tonal sound passes through a free shear layer. To quantify the amount of energy that is broadened, the ratio between the peak energy and the total energy in the spectrum is calculated with equation 5.7 and is referred to as E_{ratio}. This quantity was calculated for all tonal sound measurements. The E_{ratio} obtained when source "C1" was used, is plotted as function of frequency in figures 5.23(a) and 5.23(b) for free stream velocities of 20 and 30 m/s respectively. In both cases it can be seen that almost all energy is confined in the peak when one of the ATW's was used. In contrast to the measurements performed with the free shear layer where a drop in the E_{ratio} is observed with increasing frequency. The results obtained in case source "C2" was used are very similar and are given in appendix D. These results indicate that using ant ATW almost completely eliminates spectral broadening.

$$E_{ratio} = \frac{P^2_{peak}}{P^2_{total}} \tag{5.7}$$

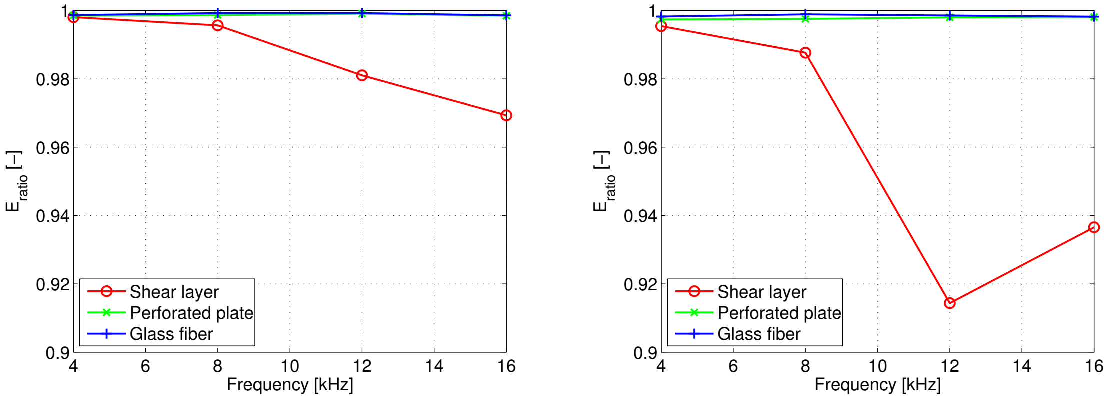

(a) $U_\infty = 20$ m/s

(b) $U_\infty = 30$ m/s

Figure 5.23: Ratio of peak over total energy (E_{ratio}) in the PSD of acoustic pressure acquired for various discrete source frequencies emitted by BMS compression driver "C1".

Sulaiman (2011) derived an expression for the E_{ratio} as function of frequency and amplitude of the time delay variations caused by the turbulence in a shear layer. This was done by approximating the broadened spectrum of a tonal source with a Taylor expansion. The resulting expression is given by equation 5.8.

$$E_{ratio} = 1 - \frac{1}{2}a^2(2\pi f)^2 \tag{5.8}$$

Equation 5.8 was used in combination with the amplitude of the time delay variations calculated from the PIV measurements, given in table 5.1, to approximate the E_{ratio}. The result for a free stream velocity of 20 m/s is depicted in figure 5.24. The evolution of this approximation of the E_{ratio} based on aerodynamic properties shows good agreement with the experimental results shown by figures 5.23(a) and 5.23(b). The actual values cannot be compared since the experiments were performed in a different wind tunnel and at different downstream locations.

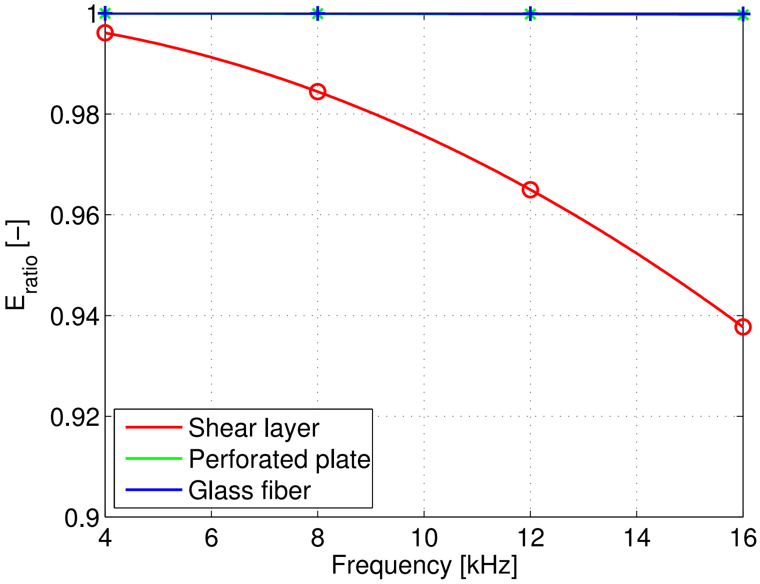

Figure 5.24: Ratio of peak over total energy (E_{ratio}) approximation based on aerodynamic properties from PIV measurements for $U_\infty = 20$ m/s.

5.3.4 Microphone array performance analysis

From the results presented in section 5.3.2 it was already clear that using an ATW has a substantial effect on the beamforming algorithm when a single frequency source is observed. In this section the performance of the microphone array will be evaluated to quantify the effects of spectral and spatial broadening caused by a turbulent region on a microphone array.

The first criterion for evaluating the performance of the array is the resolution element obtained in the source map. This resolution element is defined as the width of the main lobe in the source map, 3 dB below the peak value (Sijtsma, 2004). In chapter 2 equation 2.5 was given as an approximation of this resolution element. Using a lateral distance of 1 m and an array diameter of 0.9 m the estimated resolution for each frequency was found. Figure 5.25 shows this theoretical approximation together with the obtained resolution for the different configurations with the wind tunnel running at 30 m/s. In figure 5.25 it can be seen that both configurations with the ATW installed achieve a - 3dB beamwidth very close to the theoretical prediction for all frequencies. When the sound passed through a free shear layer the obtained resolution is also close to the theoretical prediction for the measurements up to 8 kHz. At 12 and 16 kHz the -3 dB beamwidth increases drastically. This is due to the spurious sources which are within 3 dB of the main peak and therefore form one larger source together with the actual peak. The results for a free stream velocity of 20 m/s is very similar and reported in appendix E.

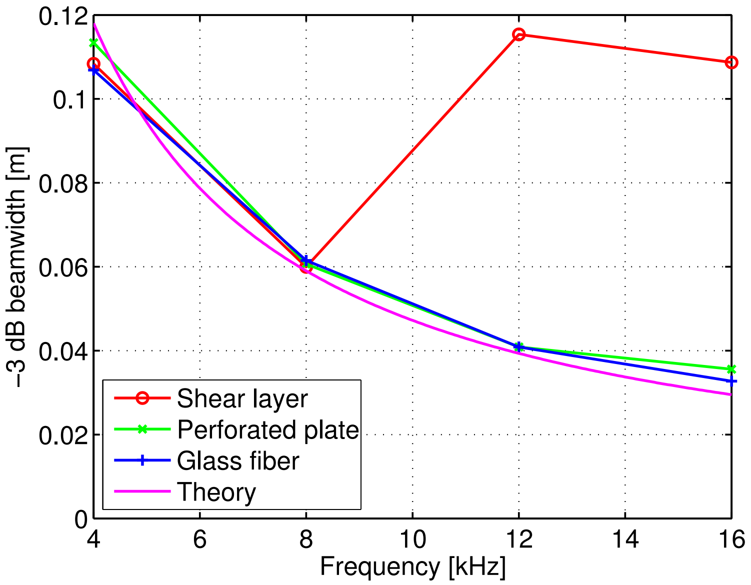

Figure 5.25: -3 dB beamwidth obtained by conventional beamformer using microphone array data acquired through different porous materials with BMS compression driver "C1" emitting discrete frequencies for $U_\infty = 30$ m/s.

The second criterion for evaluation the performance of the microphone array system is the power of the second peak in the source map. In the ideal case this second peak should not exist when performing these single source measurements. However due to the beamforming algorithm, background noise and spatial broadening there will always be a second peak detected. Since this second peak should ideally not be there, the lower its amplitude the better. This second peak is considered as an error in this point source case and therefore represents the noise floor of the measurement. The difference between the main peak en this second peak therefore represent the effective dynamic range of the measurement. The graph in figure 5.26 was calculated from the same data used to obtain the -3 dB beamwidth. This performance figure of the array does show some differentiation between the configurations. From 8 kHz on the perforated aluminium plate seems to have the lowest second peak power. The measurements done through a free shear layer have a second peak power above -6 dB which is typically used as dynamic range when analysing source maps. Therefore tonal source measurements above 12 KHz performed with the free shear layer configuration are not trustworthy. The second peak powers through the glass fiber cloth stay just below the -6 dB limit at higher frequencies.

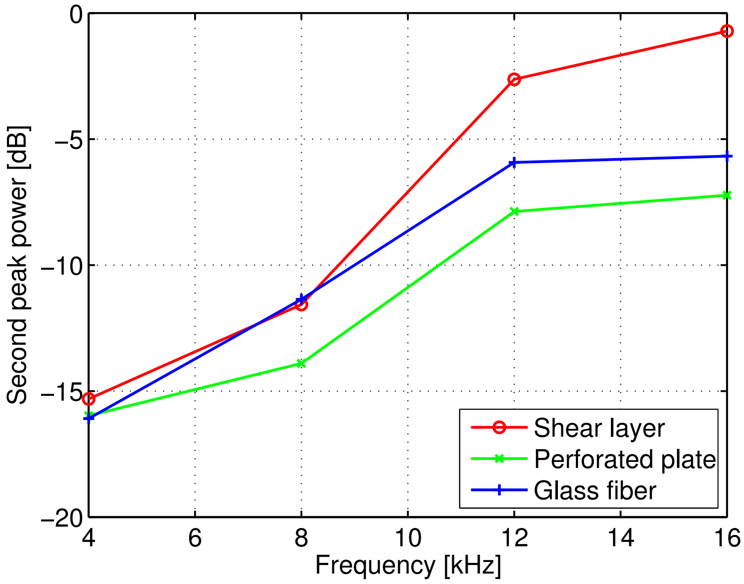

Figure 5.26: Second peak power obtained by conventional beamformer using microphone array data acquired through different porous materials with BMS compression driver "C1" emitting discrete frequencies for $U_\infty = 30$ m/s.

It is important to note that the resolution element and second peak power presented in this chapter were obtained with the conventional frequency domain beamformer described in section 2.1.2. Using a more advanced beamforming algorithm can greatly improve the performance of the microphone array. The conventional method was selected because it is still widely used for its robustness and consistency.

5.3.5 Analysis of the spurious sources

Figure 5.27 once more indicates how the spurious sources associated with the broadened frequencies can dominate over the actual source. In this figure a section is made at x=0.01 m in the source map, furthermore the frequencies related to actual peak and the broadened shoulders are processed and plotted separately. The data used corresponds to the 16 kHz case used before and is identical to the source map shown in figure 5.17. This section will further investigate the spatial broadening by looking at the interaction between a large eddie or vortex and a travelling sound wave. It is already known that the broadening in the frequency spectrum of a single microphone is due to the interaction between the sound wave and the large eddies (Sulaiman, 2011), (Krober et al., 2013). Therefore the interaction with the vortices will most likely be the main reason for the spurious sources found by the microphone array.

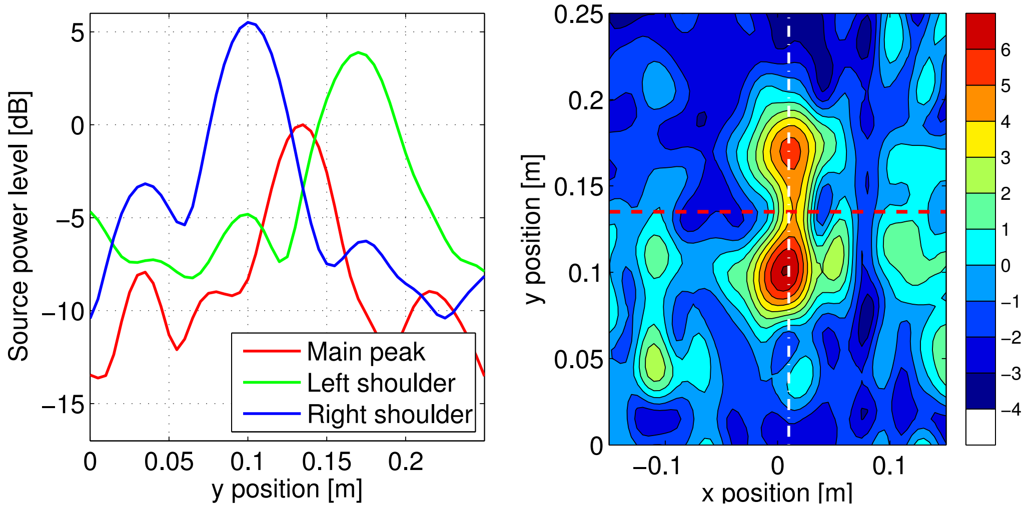

Figure 5.27: Right: source map calculated from microphone array data acquired through free shear layer, same as figure 5.17. red dashed line on the source map indicates expected source location. Left: Source power level at section x = 0.01 m, indicated by white dash-dotted line on source map. $U_\infty = 30$ m/s, $f_{source} = 16$ kHz.

The interaction between a sound wave and the turbulence inside a free shear layer will be investigated by performing a simple 2D simulation of the problem. The geometry is a simplified representation of the actual array measurements presented before. A single monochromatic source emitting sound waves with a frequency of 16 kHz is simulated at position x = 0.25, y = 1. The discrete vortices (corresponding to the shear layer lip line) are placed at y = 0.6. Finally the received signal will be evaluated at microphone positions x = 0, 0.1, 0.2, 0.3, 0.4 and 0.5 all at height y = 0. The microphones, source position and lip line on which the vortices lie are indicated on figure 5.30. The free stream velocity was set to 30 m/s.

A theoretical analysis of the interaction between a sound wave and a discrete vortex is given by Dowling (1975). After a complex derivation an approximate expression for the deflection of a sound wave passing through a vortex is obtained, given by equation 5.9. In this equation α is the angle at which the wave enters the vortex and ϕ is the angle along the vortex where the ray enters the vortex, as indicated in figure 5.28. M is the Mach number of the free stream and s is the ratio of the distance between two vortices and the radius of a single vortex, for this analysis s was set to 4. The final angle at which the wave continues after the interaction is represented by λ. It is stated in the report by Dowling (1975) that this approximate solution agrees well with the exact solution. Figure 5.29 shows how the sound rays are bend by the vortices. Note that these deflections are much higher compared to the normal shear layer refraction outlined in section 2.3.1.

$$\lambda = \alpha - \frac{Ms}{\pi} cos(\phi + \alpha) \tag{5.9}$$

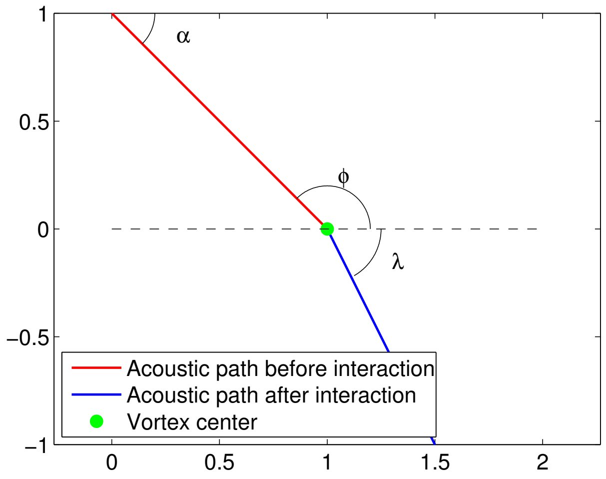

Figure 5.28: Definition of angles for equation 5.9

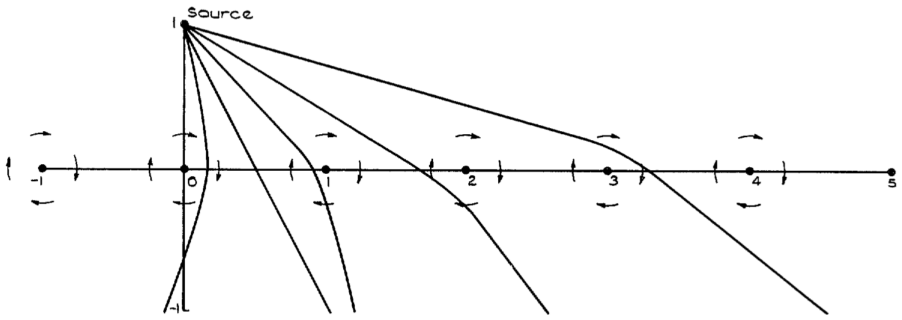

Figure 5.29: Paths of acoustic rays through vortices at M = 0.25, (Dowling, 1975)

Equation 5.9 was iteratively solved to calculate all possible paths between the source and the microphones in the simple test case described before. Since the path and deflection caused by the vortex depends on both the initial angle and the position were it enters the vortex, multiple paths between the source and a microphone are found, these are depicted in figure 5.30 for clockwise vortices.

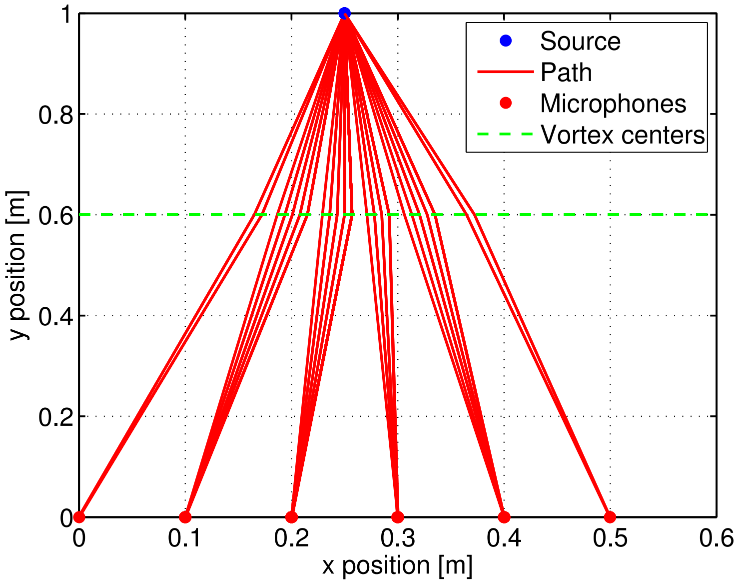

Figure 5.30: Simulation acoustic rays through clockwise vortices estimated with equation 5.9 with s = 4 and M = 0.0882 for a simple 2D test case described before.

Assuming an acoustic ray can encounter no large vortex, a clockwise or a counter-clockwise vortex when passing through a shear layer, three different sets of acoustic paths are calculated. Each set contains a different amount of paths depending on how many possible routes between the source and the microphone are found. For example, the outer microphones in figure 5.30 only have 2 possible acoustic paths through a clockwise vortex, while the inner microphones have up to 5 possible paths. Those sets of simulated signals were processed with the conventional beamforming algorithm. The three cases were calculated and plotted separately, as shown in figure 5.31. It can be seen that due to the interaction with the vortices again two spurious sources show up next to the actual source at x=0.25, similar to the phenomenon observed during the microphone array measurements. Since the interaction allows for multiple paths between the source and microphone, the spurious sources have a higher intensity compared to the actual source. Note that no acoustic energy losses are included in the simulation. The results of this simulation are remarkably similar to the results obtain during wind tunnel testing shown in figure 5.27.

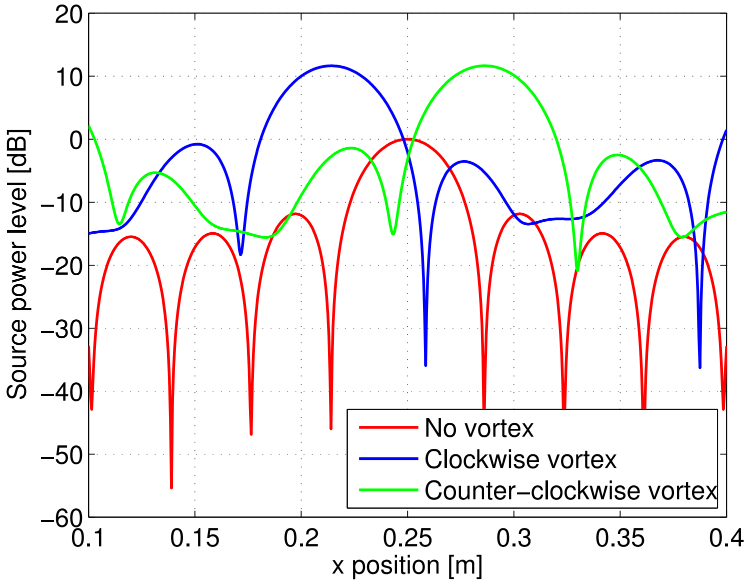

Figure 5.31: Source map of 2D test case using simulated data for cases where the sound wave does not encounter a vortex, encounters a clockwise vortex and encounters a counter-clockwise vortex. $f_{source} = 16$ kHz, $U_{\infty} = 30$ m/s

Chapter 6

Conclusions and recommendations

In this report an assessment is made of using an acoustically transparent wall (ATW) to improve aero-acoustic measurements. The ATW is constructed from a porous material that allows sound to pass through but is aerodynamically closed. During this research project several materials were tested: glass fiber cloth, Kevlar cloth, perforated aluminium and perforated steel. These materials were compared to a traditional open jet configuration, where no material is used to confine the flow. The emphasis of this research lies on reducing spectral broadening caused by a turbulent region, since this is one of the main limitations of current aero-acoustic open-jet measurements. Since the ATW must fulfil both an acoustic and an aerodynamic purpose, it was decided to initially investigate the acoustic and aerodynamic characteristics separately. Acoustic measurements in an anechoic chamber were performed in order to characterize how different porous material transmit sound waves. An aerodynamic investigation of the boundary layer over these porous materials was carried out to determine the aerodynamic parameters related to spectral broadening. Finally, the acoustic and aerodynamic effects were combined in a series of aero-acoustic wind tunnel measurements. This allows for an evaluation and performance analysis of the complete system.

First of all, it was observed that all materials show good sound transmission characteristics up to 7 kHz. The perforated plates showed some periodic variations in their acoustic power transmission coefficient beyond that frequency. It was found that the response pattern received through the perforated plates repeats itself according to a shift of twice the distance between the source and the porous material. The response pattern was further investigated and was found to originate from sound waves reflecting on the perforated plate. Because the two fibrous materials have a higher open area ratio compared to the perforated plates, less acoustic energy gets reflected. The effect was so weak that the reflected waves were not visible in the results for these cases. It was also identified that both the Kevlar and glass fiber cloths are very fragile in an unprocessed state. They should be handled with care which might form a problem under load from the wind tunnel.

PIV measurements were performed to characterize the two main aerodynamic parameters contributing to spectral broadening: wall normal velocity fluctuations v' and boundary/shear layer thickness δ. These aerodynamic parameters were measured over a selection of porous walls. It was found that both these parameters are greatly reduced over an acoustically transparent wall when compared to a free shear layer. Typically the maximum standard deviation (rms) of the wall normal velocity fluctuations were reduced from 10.5 % of the free stream velocity to 5 % for the fiber weaves and 7.5 % for the perforated plate. The thickness of the boundary layer over the porous materials was only a fraction of the shear layer thickness, which indicates smaller scales for the turbulence. A model by Sulaiman (2011) allowed for a prediction of the amplitude of the time delay variations caused on an acoustic wave, based on the measured aerodynamic properties. The model predicted a reduction in amplitude of up to 95 % for a tensioned glass fiber wall when compared to a free shear layer and about 90 % for the perforated plates. The Kevlar cloth had higher levels of turbulence at high free stream velocities, likely caused by vibrations at high free stream velocities due to its lack of tension.

Finally, a series of aero-acoustic experiments with a speaker source in a wind tunnel were performed. Spectral broadening through a free shear layer was observed at frequencies of 8, 12 and 16 kHz with free stream velocities of 20 and 30 m/s. The relations between the amount of spectral broadening and flow velocity or source frequency were in good agreement with previous measurements and theoretical predictions. It was concluded that through a free shear layer the ratio of the peak energy over the total energy in the acoustic pressure PSD dropped significantly with increasing frequency while through an ATW nearly all energy is confined in the peak. On the other hand it was also observed that the installation of an ATW adds background noise to the measurements. Especially at higher frequencies the background level can be increased by 10 dB.

In addition to a single microphone system, a 64 element microphone array was used. It can be concluded that the performance of the acoustic array is greatly improved by installing an ATW for frequencies above 8 kHz. At those frequencies the -3 dB beamwidth in case an ATW was used is less than half of the - 3 dB beamwidth obtained through a free shear layer. At those higher frequencies the sidelobe level is reduced by approximately 5 dB, increasing the dynamic range of the measurement. At 12 and 16 kHz the effective dynamic range obtained through a free shear layer was reduced to less than 6 dB, which is typically the range used for analysing source maps. Therefore at these high frequencies tonal measurements performed through a free shear layer are not trustworthy.

From analysing the source maps calculated from the array, it was found that the interaction between the turbulent structures in a free shear layer and an acoustic wave not only lead to spectral broadening, but also lead to spatial broadening for microphone array measurements. The broadened parts of the frequency spectrum led to spurious sources in the source maps. These appear above and below the actual source. For example with a free stream velocity of 30 m/s and a source signal at 16 kHz, these spurious sources can have a higher amplitude than the actual source when measuring through a free shear layer. With an ATW installed their amplitude was 30 dB below the real peak for the same testing conditions. A simple 2D simulation showed that the spurious sources are possibly due to the interaction between the sound waves and the large vortices inside the turbulent shear layer. The acoustic paths are "bend" due to the vortex making multiple routes between the source and the microphone possible. These different routes have corresponding time delays which are associated with the spurious sources and misinterpreted by the beamforming algorithm as sources above and below the actual source.

In general it can be concluded that installing an acoustically transparent wall in a wind tunnel greatly improves aero-acoustic measurements when a single frequency source is considered. Spectral and spatial broadening is almost eliminated by installing the ATW and both the dynamic range and resolution of an acoustic array are improved. Note that this improvement only becomes relevant at high source frequencies and high flow speeds. For a source at 4 kHz and free stream velocity of 20 m/s little difference was found between the case with a free shear layer and the ATWs. It must also be stated that the perforated metal plates are a viable alternative to the tensioned fiber walls previously used as ATW. Except for the increased background noise, little difference was found between the two porous materials during the final aero-acoustic wind tunnel test and the perforated plates offers many benefits with respect to the construction of the test section.

Recommendations

Although an acoustically transparent wall already shows great potential for aero-acoustic testing it can sill be improved and further research is required. The perforated plate has proven to be a cheaper and easier to handle alternative to the tedious tensioned Kevlar cloths used before. However the lower open area of the perforated plate reduced the transmission coefficient at higher frequencies, leading to more reflections. In addition to that once installed in the wind tunnel the background noise was elevated. Therefore it is suggested to do more research towards the optimal perforated material for an acoustically transparent wall. Reducing the hole size and shape might solve both issues.

It is also suggested that the ATW should be tested in a case of strong spectral broadening where the peak related to the source completely vanishes. This would require wind tunnel speeds of up to 70 m/s and source frequencies of 32 kHz and above. During this research project only weak spectral broadening was considered due to the limited capabilities of the wind tunnel, measurement and source systems used. Another facet that was not investigated during this research was the effect that an ATW has on the aerodynamic performance of the wind tunnel. By installing an ATW the test-section becomes (semi)-closed. The accuracy and consistency of the wind tunnel should be improved, requiring less aerodynamic corrections and the usable test section space would be increased as well. This was outside the scope of this research, but would be an interesting topic for further research.

Bibliography

Christopher S. Allen, Blake K. William, Robert P. Dougherty, Denis Lynch, Paul T. Soderman, and James R. Underbrink. *Aeroacoustics Measurements.* Springer, 2002. ISBN 3540417575.

A. B. Bauer. Acoustically Transparent Walls for Wind-Tunnel Applications. Technical Report 8, Douglas Aircraft Company, 1976.

JK Brueckner and R Girvin. Airport noise regulation, airline service quality, and social welfare. *Transportation Research Part B: Methodological*, 2006.

L. M. B. C. Campos. The spectral broadening of sound by turbulent shear layers. Part 1. The transmission of sound through turbulent shear layers. Technical report, Engineering Department, University of Cambridge, 1977.

HE Carmargo, BS Smith, WJ Devenport, and RA Burdisso. Evaluation and Calibration of a Prototype Acoustic Test Section for the Virginia Tech Stability Wind Tunnel. *VPI= OAE-294, Virginia*, (May), 2005.

A. Dowling. The Refraction of Sound by a Shear Layer made up of Discrete Vortices. Technical report, Ministry of Defence, Aeronoutical Resaerch Council, 1975.

K Ehrenfried, L Koop, A Henning, and K Kaepernick. Effects of Windtunnel Noise on Array Measurements in Closed Test Sections. *BeBeC Paper*, pages 1–6, 2007.

Takeshi Ito, Hiroki Ura, Kazuyuki Nakakita, and Yuzuru Yokokawa. Aerodynamic/Aeroacoustic testing in Anechoic Closed Test Sections of Low-Speed Wind Tunnels. *AIAA2010-3750*, pages 1–11, 2010.

J Jabben, E.N.G. Verheijen, and B. du Pon. Monitoring luchtvaartgeluid. Trends in de geluidbelasting door luchtvaart. *RIVM rapport*, 2010.

SM Jaeger, WC Horne, and CS Allen. Effect of surface treatment on array microphone self-noise. *AIAA Paper AIAA-2000-1937*, 2000.

S. Krober, M. Hellmold, and L Koop. Experimental Investigation of Spectral Broadening of Sound Waves by Wind Tunnel Shear Layers. Technical report, 2013.

Ulf Michel. History of acoustic beamforming. *BeBeC2006*, pages 1–17, 2006.

L Van Midden. The potential of aircraft noise monitoring using acoustic arrays. Master's thesis, TU Delft, 2013.

S. Oerlemans and P. Sijtsma. Determination of absolute levels from phased array measurements using spatial source coherence. AIAA-2002-2464, 2002. 8th AIAA/CEAS Aeroacoustics Conference and Exhibit, Breckenridge, Colorado, June 17-19, 2002.

Stefan Oerlemans and Beatriz Méndez López. Acoustic Array Measurements on a Full Scale Wind Turbine. *11th AIAA/CEAS Aeroacoustics Conference*, (May):23–25, May 2005. doi: 10.2514/6.2005-2963.

S.B. Pope. *Turbulent Flows*. Cambridge University Press, 2000. ISBN 9780521598866.

RC Ramachandran, Hirenkumar Patel, Ganesh Raman, and RP Dougherty. Localization of Wind Turbine Noise Sources Using a Compact Microphone Array with Advanced Beamforming Algorithms. *bebec.eu*, pages 1–14, 2012.

PA Ravetta, RA Burdisso, and WF Ng. Phased array technology development at Virginia tech: Application to landing gear noise source identification. *Mecanica Computacional*, XXIII(November), 2004.

Marcel Remillieux, Erin Crede, Hugo Camargo, Ricardo Burdisso, William Devenport, Matthew Rasnick, Philip Van Seeters, and Amanda Chou. Calibration and Demonstration of the New Virginia Tech Anechoic Wind Tunnel. *14th AIAA/CEAS Aeroacoustics Conference (29th AIAA Aeroacoustics Conference)*, pages 1–17, May 2008. doi: 10.2514/6.2008-2911.

P Sijtsma. Experimental techniques for identification and characterisation of noise sources. *Advances in Aeroacoustics and Applications, VKI . . .* , (April), 2004.

P Sijtsma. Phased Array Beamforming Applied to Wind Tunnel And Fly-Over Tests. *SAE Technical Paper*, (October):17–19, 2010.

P Sijtsma and H van der Waal. Identification of noise sources on civil aircraft in approach using a phased array of microphones. (April), 2004.

HA Siller, S Schroder, G Saueressig, and S Frohlich. Beamforming on a Turbofan Engine in an Indoor Test-Facility. pages 1–11, 2008.

RW Stoker, Yueping Guo, C Streett, and Nathan Burnside. Airframe noise source locations of a 777 aircraft in flight and comparisons with past model scale tests. *AIAA Paper*, (May): 1–10, 2003.

Zana Sulaiman. Effect of Open-Jet Shear Layers on Aeroacoustic Wind Tunnel Measurements. Master's thesis, TU Delft, 2011.

H. Tennekes and J.L. Lumley. *A first Course in turbulence*. Butterworth, 1990.

Dirk van Dun and M Tuinstra. Design , construction and assessment of an acoustically transparent test section. Master's thesis, Hogeschool Inholland, 2011.

Milton Van Dyke, editor. *Album of Fluid Motion.* The Parabolic Press, Stanford, California, tenth edition, 1982.

F.M. White. *Viscous fluid flow.* McGraw Hill Series in Mechanical Engineering. McGraw-Hill Professional Publishing, 1991. ISBN 9780070697126.

Kingo J Yamamoto, Michael J Donelson, Shumi C Huang, and Mahendra C Joshi. Airframe Noise Prediction Evaluation. Technical Report October, NASA, 1995.

Appendix A

V-tunnel nozzle

The recommended wind tunnel available at the TU Delft for conducting the final aero-acoustic measurement campaign was the V-tunnel because it has the lowest background noise of all the available tunnels. The wind tunnel is an open jet vertical wind tunnel with a circular exit of 0.6 m in diameter. It was however preferred to have square 0.4 m by 0.4 m exit since that would make the new test section compatible with other wind tunnel at the TU Delft (M-tunnel, W-tunnel). Furthermore a square test section makes the construction of the acoustically transparent walls significantly less difficult and allows for easier corrections with respect to the shear layer. Therefore it was decided to construct a nozzle which would contract the flow from a circular 0.6 m diameter cross-section to a square 0.4 m by 0.4 m cross-section. This appendix will contain information about the design, construction and validation of the nozzle.

A.1 Design

Since the time available for this nozzle was limited and the contraction ratio was low (only 1.8), a simple and fast design process was used. Some basic rules were followed to obtain the initial design which was then improved several times based on comments of experienced people at the faculty. The main design rules were:

- Make all curvatures smooth, especially when an adverse pressure gradient will be present.
- Let the nozzle end with a straight part to align the flow.
- Make the end points of the contraction tangential to the center axis of the wind tunnel for a smooth transition.

- Add corner fillets which vanish towards the end in the straight part in order to avoid corner vortices.

From these rules a model was made with the aid of CATIA. First the two end cross-sections were drawn after which an intermediate octagonal cross-section was added. Based on the rules above eight guiding curves were drawn which would enable CATIA to form a closed surface between the cross-sections. Careful attention was paid to make sure that the guide curves were as smooth as possible and were tangential with the centre axis at the end points. The three cross-sections and guiding curves can be seen in figure A.1(a) and the final closed design can be seen in figure A.1(b). In this final design the contraction has a length of 40 cm and is followed by a straight part to align the flow of 30 cm with fading corner fillets .

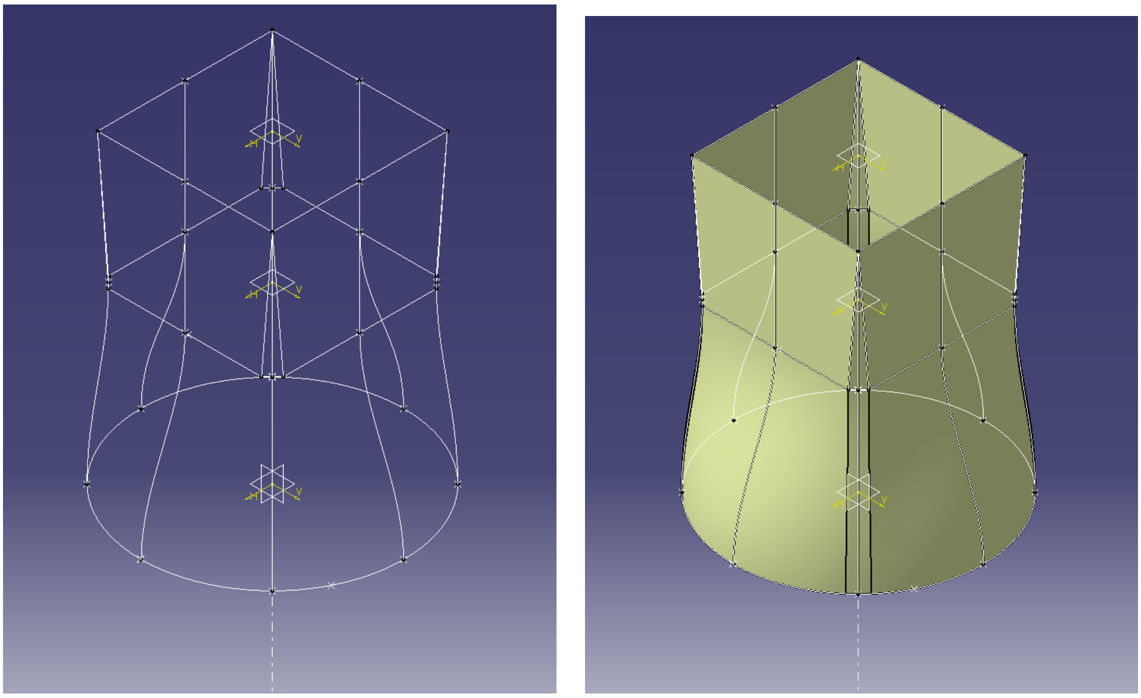

(a) Cross-section and guiding curves

(b) Final nozzle shape in CATIA

Figure A.1: CATIA drawings of the nozzle design

A.2 Construction

It was decided to make the contraction part of the nozzle from foam and the straight part from wood. The corner fillets would be added afterwards. The contraction was constructed from eight foam plates with a thickness of 5 cm. Because the plates were not wide enough they first had to be glued to create larger plates as can be seen in figure A.2(a). After that the 8 required cross-section were made from the CATIA model to get the exact shape needed, these were printed on a 1:1 scale and taped onto the foam plates, see figure A.2(b). Each section was cut out with a jig saw after which they were glued on top of each other as can be seen in figure A.2(c). When the glue was dry, the remaining unwanted material was removed with sandpaper. Figure A.2(d) shows the contraction during this sanding process. This process repeated until a smooth shape/surface was obtained which can be seen in figure A.3(a). Next a wooden top and bottom section were added to the contraction which allows to mount it firmly on the current wind tunnel exit (figure A.3(b)). After that the straight part was constructed from wood shown in figure A.3(c) and the foam corner fillets were added. Finally the nozzle was finished with two layers of epoxy paste to give it a smooth surface and remove all cracks and dents. The final product is depicted in figure A.3(d). The nozzle was fixed to the current circular exit with four long M8 bolts.


(a) (b) (c) (d)

Figure A.2: Photos of construction of the nozzle, Part 1

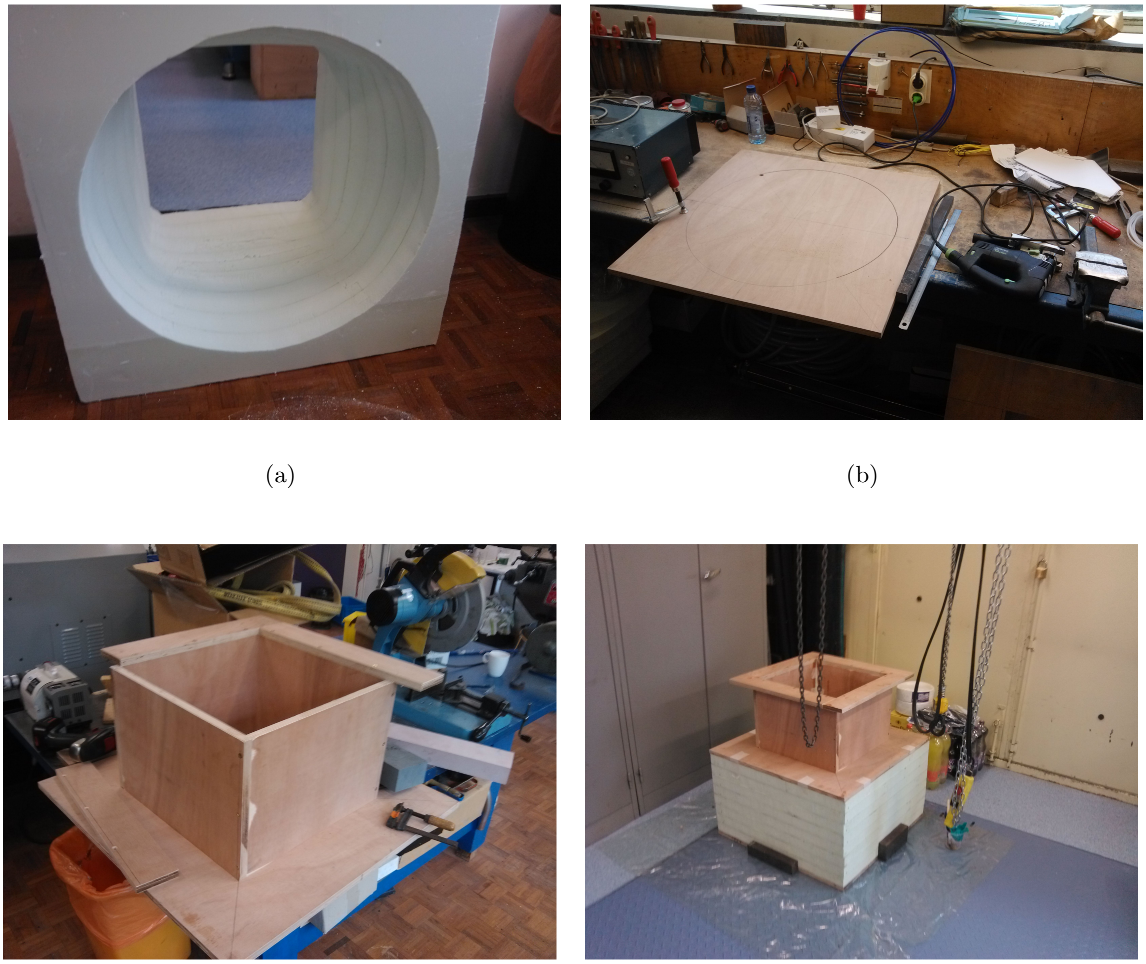

(a) (b)

(c) (d)

Figure A.3: Photos of construction of the nozzle

A.3 Validation

A.3.1 Setup

To determine the outflow of the new contraction a series of pitot tube measurements was done. The pitot tube was connected to a Mensor digital pressure gauge (model 2101 SN 532017). The dynamic pressure was sampled by a Labview program at 10 Hz for 15 seconds. Initially the whole exit was measured at 169 points 20 mm above the exit with a fan speed of 1000 rpm. The location of the points is represented by the marks in figure A.4. The pitot tube was mounted on a traverse to allow for smooth and exact displacements. However the travers had a reach of only 30 cm which was insufficient to test the whole section, therefore it was moved several times by hand as well. The blue squares were used to evaluate the performance of the new nozzle at various fan speeds and heights. They were tested at 1000, 1500, 2000 rpm and a height of 20 mm and 200 mm . For these test only the height adjustment had to be done manually, all the other movements were done with the traverse.

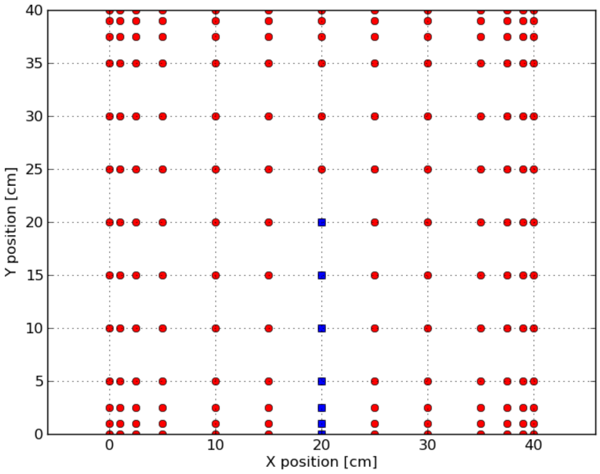

Figure A.4: Measurement points

Since the flow can be treated as incompressible the measured dynamic pressure can be converted to flow velocity by using equation A.1. Where q is the measured dynamic pressure and ρ the density of air.

$$U = \sqrt{\frac{2q}{\rho}} \tag{A.1}$$

A.3.2 Results and discussion

Figure A.5(a) shows the measured flow velocities over the exit of the nozzle. In figure A.5(a) those velocities were expressed with respect to the average of the nine center points, resulting in the variation from the mean flow velocity. Overall it can be seen that the velocity profile is smooth and flat, most of the variations are below 1 %. The variations that are measured are probably influenced by measurements errors. The first main cause for error is that the pitot tube had to be moved manually several times to span the whole cross-section. It was noticed that after moving the pitot and traverse system manually a constant shift could be observed. The variation was much lower when the pitot was only displaced by the traverse. This is the reason for the vertical stripes visible in figure A.5(a). A second source of error comes from the ambient pressure, temperature and density, these were all assumed to be constant while after running the wind tunnel for a long time, these will most likely have changed.

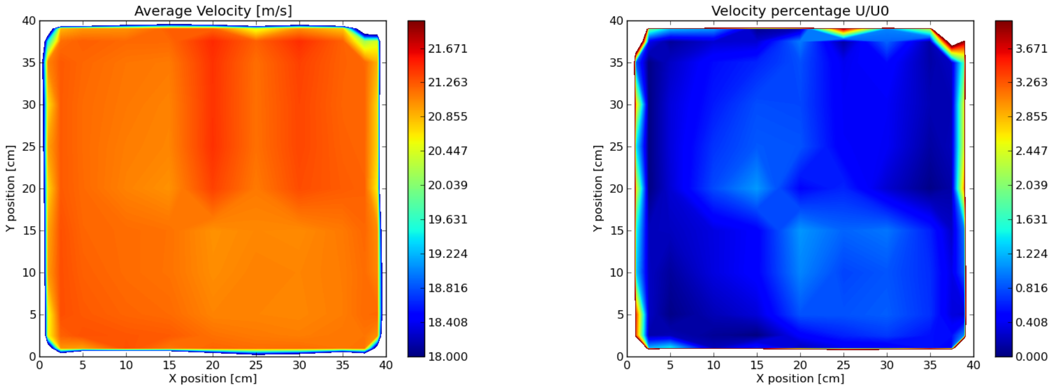

(a) (b)

Figure A.5: Results from first measurement at height = 20 mm, fan speed = 1000 rpm

The second series of experiments should eliminate the two sources of error mention earlier since the measurement time is much shorter (due to the fewer points) and the movement can be done by the traverse. The resulting measurement profiles were again scaled with the average of the centre three points. From figure A.6 it can be seen that the velocity profile is very flat and consistent for all tested cases. Only 1 cm away from the exits edge the difference from the mean flow velocity is below 1 % and 5 cm from the edge the difference is even below 0.3 % for all measured cases.

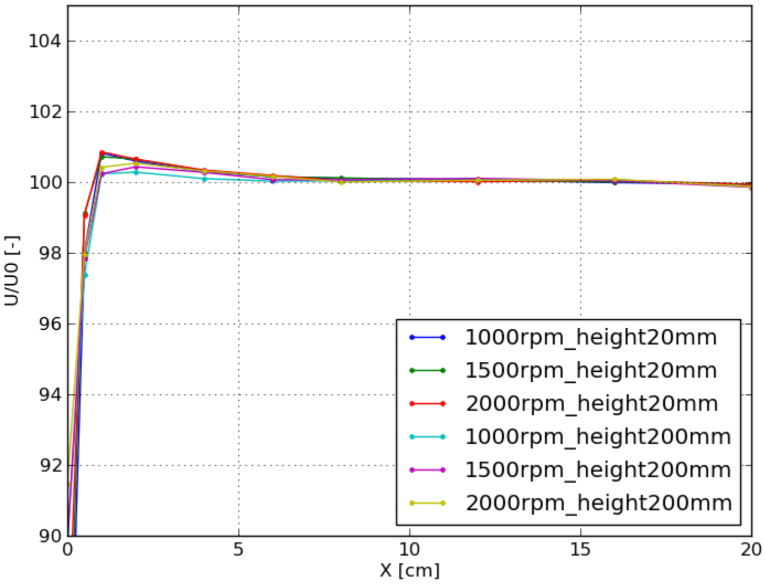

Figure A.6: Results of second measurement series

A final series of experiments was conducted to determine the boundary layer thickness at the nozzle exit. The same traverse system as before was used but now the pitot tube was placed level with the nozzle exit and moved towards the center of the nozzle with 2 mm increments to determine the boundary layer profile. Figure A.7 show the boundary layer profile at two different free stream velocities. In both cases the profile becomes straight at around 15 mm, indication the boundary layer thickness.

Finally a run was done at maximum fan rmp to determine the new maximum free stream velocity of the wind tunnel. The new maximum velocity was found to by 55 m/s.

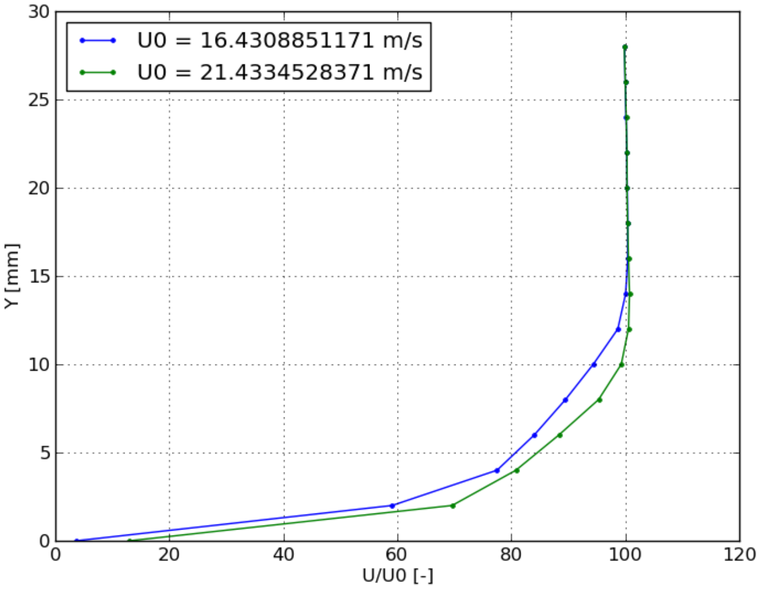

Figure A.7: Boundary layer profiles at nozzle exit

Appendix B

PSD of acoustic pressure measured through ATW's

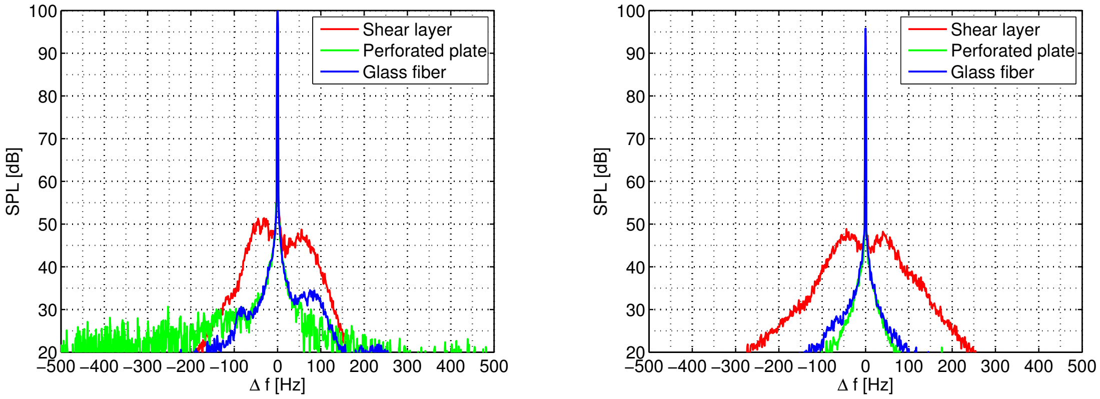

(a) $f_{source} = 4$ kHz

(b) $f_{source} = 8$ kHz

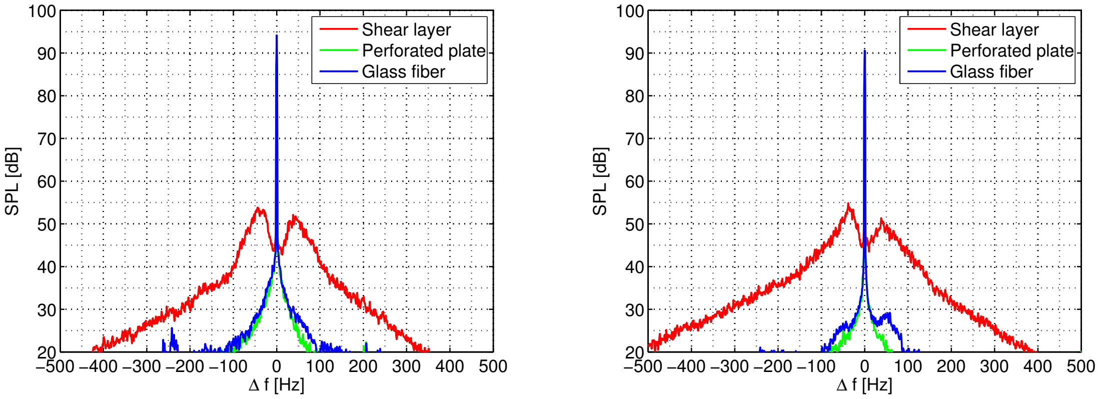

(c) $f_{source} = 12$ kHz

(d) $f_{source} = 16$ kHz

Figure B.1: PSD of acoustic pressure acquired through different porous materials for case with tonal noise source located in open jet with free stream velocity of 20 m/s. Microphone at reference position (x=y=0), see figure 4.7(b).

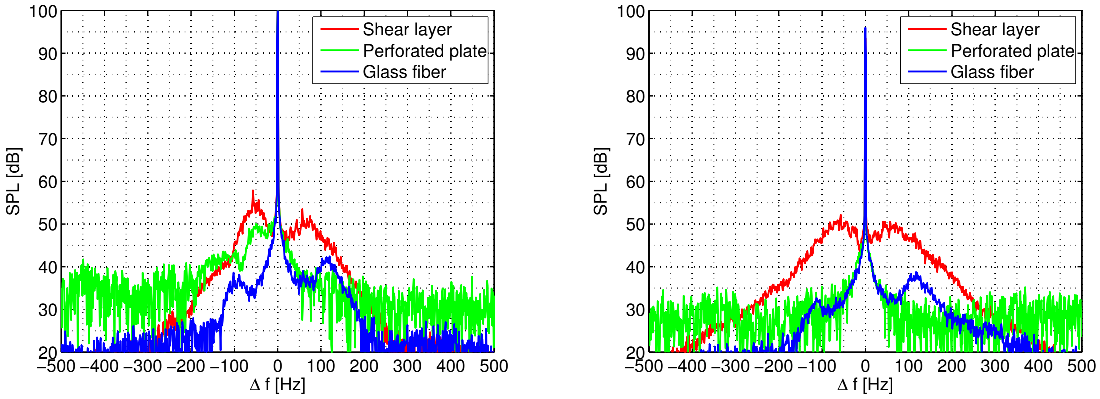

(a) $f_{source} = 4$ kHz

(b) $f_{source} = 8$ kHz

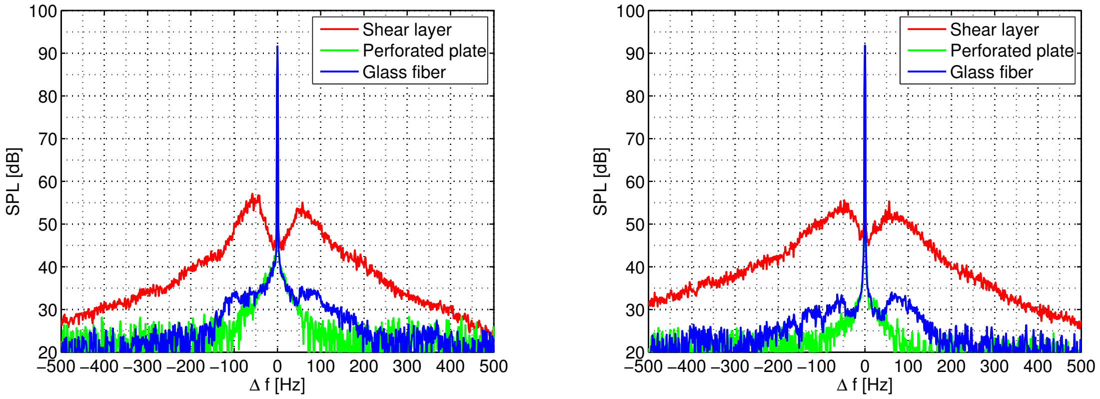

(c) $f_{source} = 12$ kHz

(d) $f_{source} = 16$ kHz

Figure B.2: PSD of acoustic pressure acquired through different porous materials for case with tonal noise source located in open jet with free stream velocity of 30 m/s. Microphone at reference position (x=y=0), see figure 4.7(b).

Appendix C

Source maps of 12 kHz case

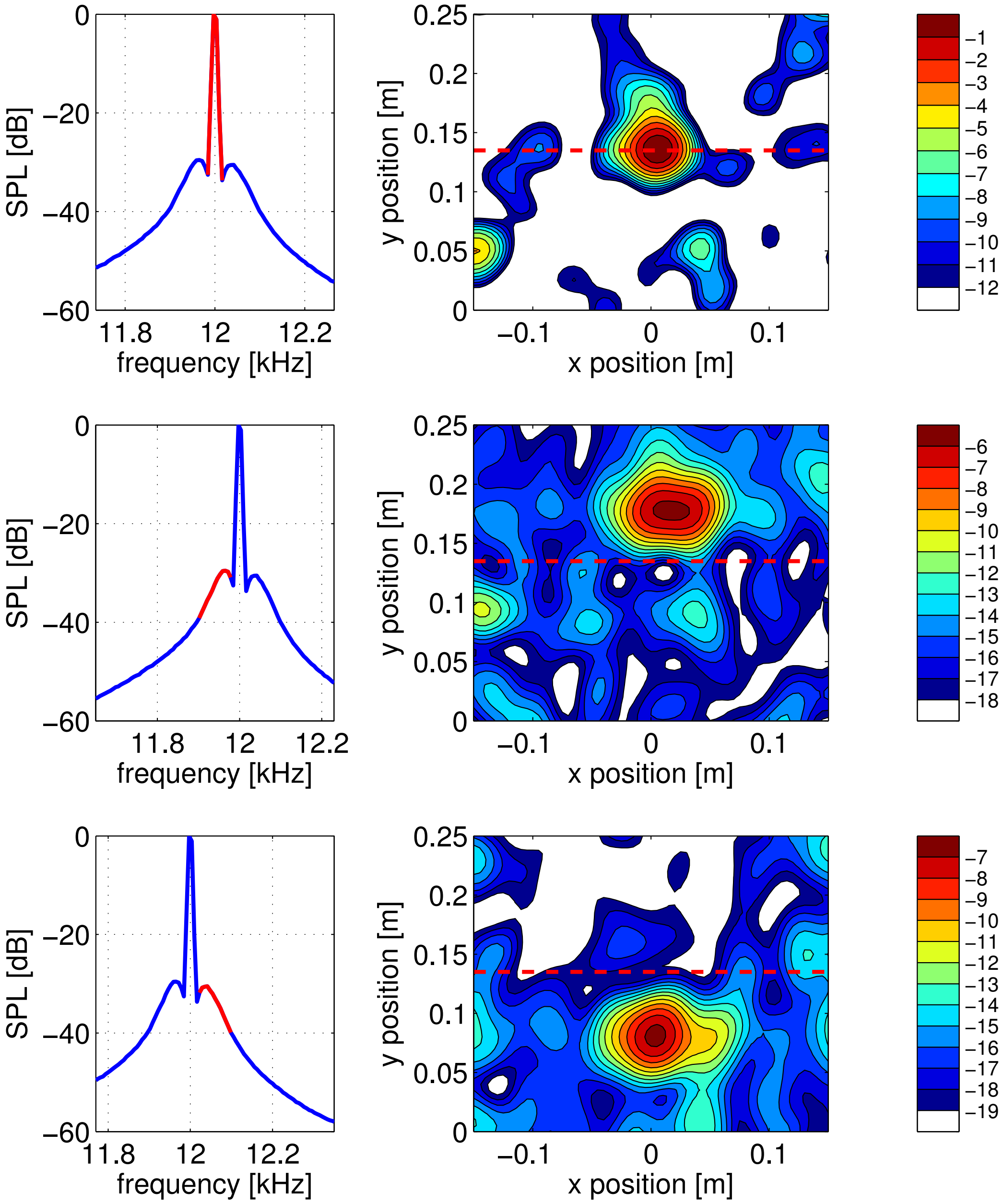

Figure C.1: Left: PSD of acoustic pressure from single microphone; Right: source map of main peak (top) and shoulders (middle, bottom) calculated from microphone array data acquired through free shear layer. Red line on the PSD indicates frequency band used by the beamforming algorithm, red dashed line on the source map indicates expected source location. $U_\infty = 20$ m/s, $f_{source} = 12$ kHz.

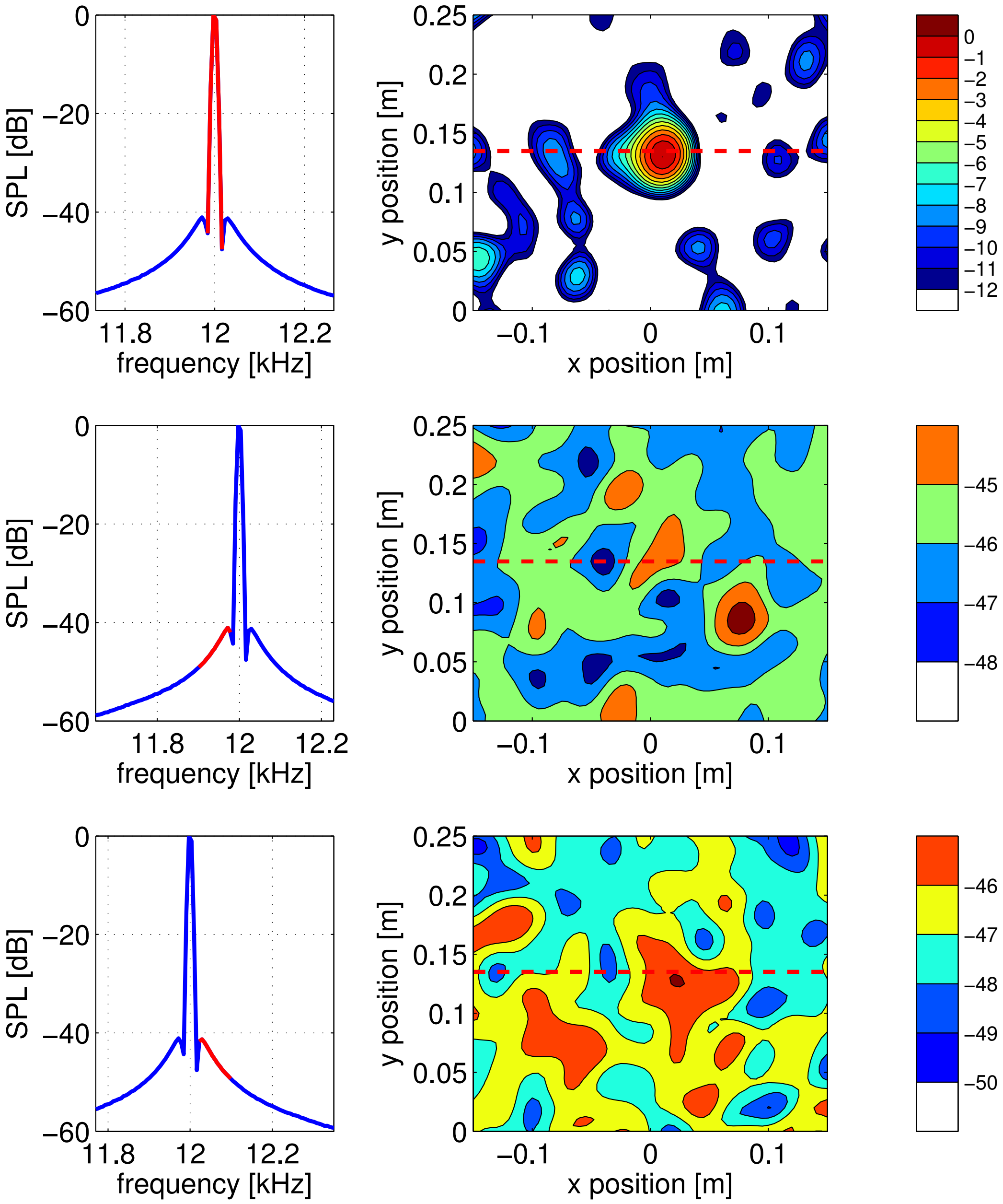

Figure C.2: Left: PSD of acoustic pressure from single microphone; Right: source map of main peak (top) and shoulders (middle, bottom) calculated from microphone array data acquired through perforated metal plate. Red line on the PSD indicates frequency band used by the beamforming algorithm, red dashed line on the source map indicates expected source location. $U_\infty = 20$ m/s, $f_{source} = 12$ kHz.

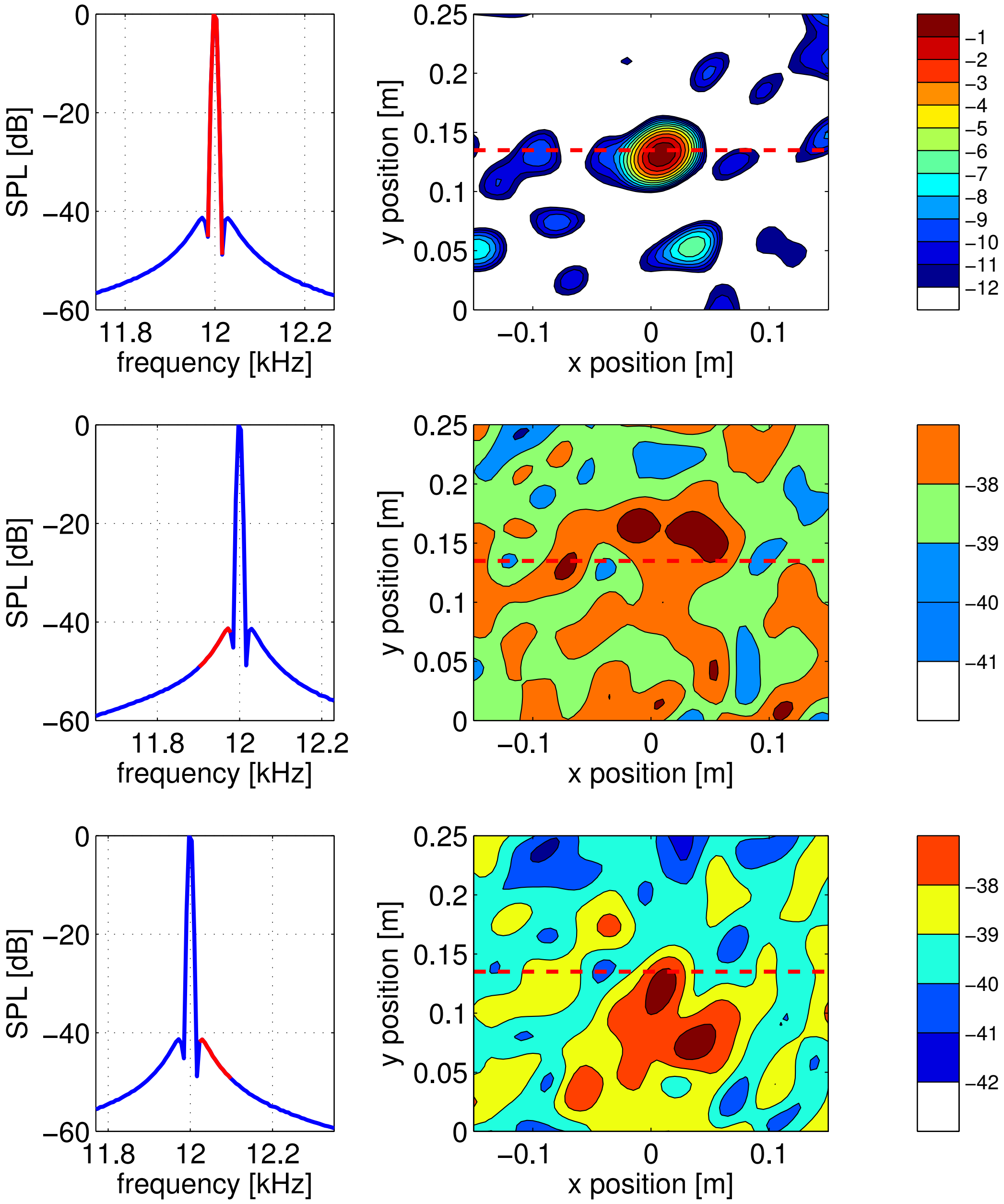

Figure C.3: Left: PSD of acoustic pressure from single microphone; Right: source map of main peak (top) and shoulders (middle, bottom) calculated from microphone array data acquired through tensioned glass fiber wall. Red line on the PSD indicates frequency band used by the beamforming algorithm, red dashed line on the source map indicates expected source location. $U_\infty = 20$ m/s, $f_{source} = 12$ kHz.

Appendix D

Quantification of spectral broadening with source "C2"

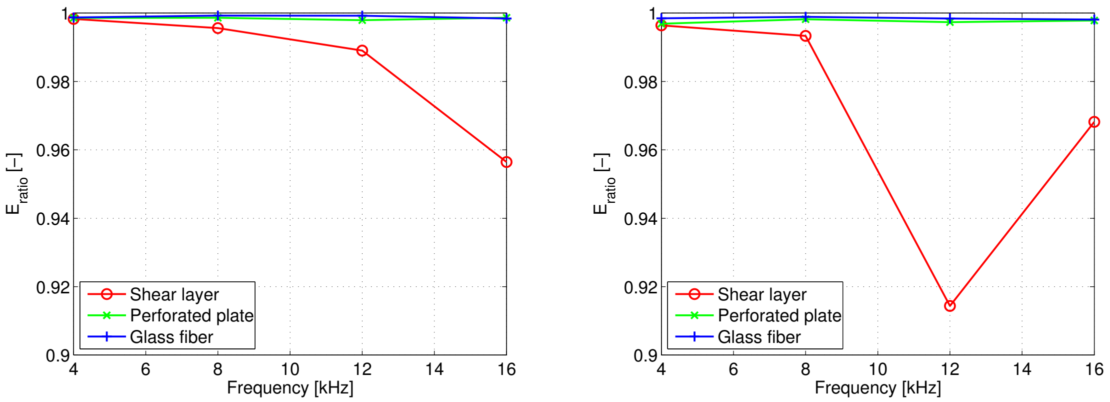

(a) $U_\infty = 20$ m/s

(b) $U_\infty = 30$ m/s

Figure D.1: Ratio of peak over total energy (E_{ratio}) in the PSD of acoustic pressure acquired for various discrete source frequencies emitted by BMS compression driver "C2", see figure 4.7(b).

Appendix E

Microphone performance figures at 20 m/s

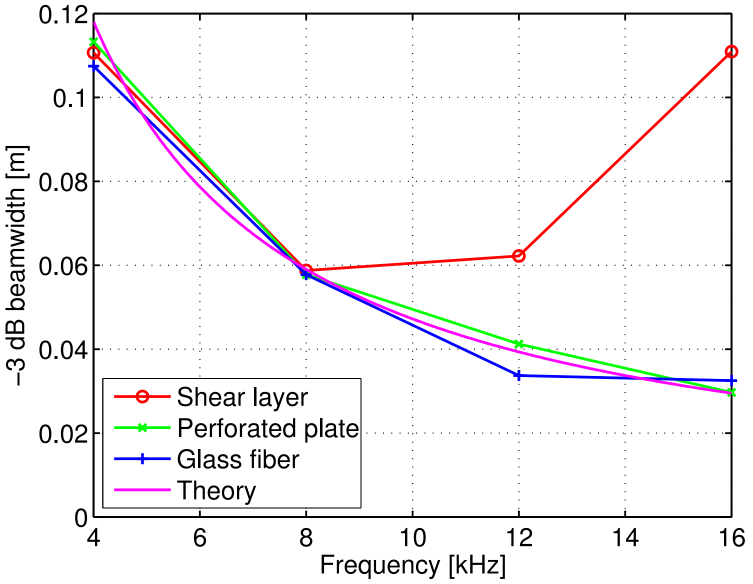

Figure E.1: -3 dB beamwidth obtained by conventional beamformer using microphone array data acquired through different porous materials with BMS compression driver "C1" emitting discrete frequencies for $U_\infty = 30$ m/s.

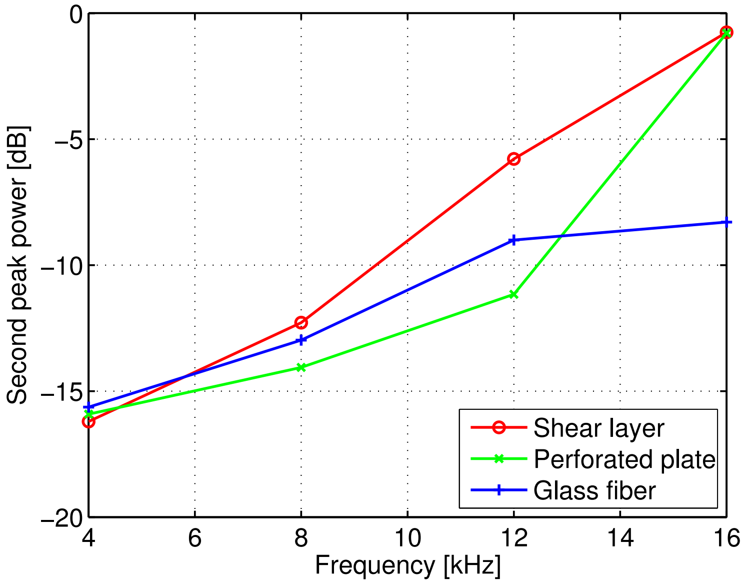

Figure E.2: Second peak power obtained by conventional beamformer using microphone array data acquired through different porous materials with BMS compression driver "C1" emitting discrete frequencies for $U_\infty = 20$ m/s.